ADVANCED MINERALOGY 3

Arnold S. Marfunin
Editor

Mineral Matter in Space, Mantle, Ocean Floor, Biosphere, Environmental Management, and Jewelry

Springer

Arnold S. Marfunin (Ed.)

Advanced Mineralogy

Volume 3
Mineral Matter in Space, Mantle, Ocean Floor, Biosphere, Environmental Management, and Jewelry

With 168 Figures and 41 Tables

Springer

Prof. Dr. Arnold S. Marfunin

Geological Faculty
University of Moscow
119899 Moscow
Russia, CIS

ISBN 978-3-642-62108-6

Library of Congress Cataloging-in-Publication Data Advanced mineralogy/Marfunin. Arnold S. (ed.). p. cm. Includes bibliographical references and index. Contents: – v. 3. Mineral Matter in Space, Mantle, Ocean Floor, Biosphere, Environmental Management, and Jewelry
1. Mineralogy. 1. Marfunin. Arnol'd Sergeevich.
ISBN 978-3-642-62108-6 ISBN 978-3-642-18154-2 (eBook)
DOI 10.1007/978-3-642-18154-2
QE363.2.A35 1994 549 — dc20 94-13315

Originally published by Springer-Verlag Berlin Heidelberg in 1998
Softcover reprint of the hardcover 1st edition 1998

Coverdesign: E. Kirchner, Springer-Verlag
Production: ProduServ GmbH Verlagsservice, Berlin
Typesetting: Fotosatz-Service Köhler OHG, Würzburg

SPIN: 10474900 32/3020 – 5 4 3 2 1 0 – Printed on acid-free paper

Contents

Chapter 1 Mineral Matter in Space

List of Contributors

ANDERSON, J. R., Dept of Chemistry and Biochemistry, Arizona State University, Tempe, Arizona 85287, USA
BAMBAUER, H. U. , Institut für Mineralogie, Universität Münster, Vogelweide 7, D-48346 Ostbevern-Brock, Germany
BARSKOV, I. S., Department of Geology, Moscow State University, Moscow 119899, Russia
BATURIN, G. N., Institute of Oceanology, Russian Academy of Sciences, Krasnikova 23, Moscow 117218, Russia
BOGDANOV, YU. A., Institute of Oceanology, Russian Academy of Sciences, Krasnikova 23, Moscow 117218, Russia
BUSECK, P. R., Department of Geology, Arizona State University, Tempe, Arizona 85287, USA
CHELISHCHEV, N. F., Institute of Mineralogy, Geochemistry and Crystallochemistry of Rare Elements, Moscow 113035, Sadovnicheskay Nab. 71, Russia
CALMANO, W., Arbeitsbereich Umweltschutztechnik, TU Hamburg-Harburg, Eichendorferstr. 40, D-21073 Hamburg, Germany
DEISSMANN, G., Institut f. Mineralogie u. Lagerstättenlehre, RWTH Aachen, Wüllnerstr. 2, D-52062 Aachen, Germany
DEUTSCH, A., Institut für Planetologie, Universität Münster, Wilhelm-Klemm-Str. 10, D-48149 Münster, Germany
DUBROVINSKAIA, N. A., Institute of Earth Sciences, Uppsala University, S-75236 Uppsala, Sweden
DUBROVINSKY, L. S., Institute of Earth Sciences; Mineralogy-Petrology, Uppsala University, S-75236 Uppsala, Sweden
FISENKO, A.V., Vernadsky Institute of Geochemistry, Vorobjevskoe 10, Moscow 117975, Russia
FÖRSTER, H. G., Institut für Mineralogie und Lagerstättenlehre der RWTH Aachen, Wüllnerstr. 2, D-52062 Aachen, Germany
FÖRSTNER, U., Arbeitsbereich Umweltschutztechnik, TU Hamburg-Harburg, Eichendorferstr. 40, D-21073 Hamburg, Germany

FRIEDRICH, G., Institut für Mineralogie und Lagerstättenlehre der RWTH Aachen, Wüllnerstr. 2, D-52062 Aachen, Germany
GAFT, M. L., Open University of Israel, Geology and Physics Group, 16 Klausner St., P.O.B. 39328 Ramat-Aviv, Tel-Aviv 61392, Israel
HELING, D. F. W., Institut für Umweltgeochemie, Universität Heidelberg, D-69020 Heidelberg, Germany
KASHKAROV, L. L., Vernadsky Institute of Geochemistry, Vorobjevskoe 10, Moscow 117975, Russia
KERSTEN, M., Institut f. Ostseeforschung, Sektion Marine Geologie, Seestr. 15, D-18119 Rostock-Warnemünde, Germany
KHORASANI, R., FH Hamburg, FB Bauingenieurwesen, Hebebrandstr. 1, D-22297 Hamburg, Germany
KOHLER, E., Lehrgebiet Angew. Geologie, Universität Regensburg, Universitätsstr. D-93053 Regensburg, Germany
KURAT, G., Naturhistorisches Museum, Burgring 7, Postfach 417, A-1014 Vienna, Austria
KOZENKO, A.V., Institute of Physics of the Earth, Bolshaya Grusinskaya 10, Moscow 123810, Russia
KUSKOV, O. L., Vernadsky Institute of Geochemistry, Vorobjevskoe 10, Moscow 117975, Russia
LANGENHORST, F., Bayerisches Geoinstitut, Universität Bayreuth, D-95440 Bayreuth, Germany
MARFUNIN, A. S., Department of Mineralogy, Moscow State University, Moscow 119899, Russia
MASAITIS, V. L., Karpinsky Geological Institute, Sredny Prospect 74, St. Petersburg 199026, Russia
NAZAROV, M. N. Vernadsky Institute of Geochemistry, Vorobjevskoe 10, Moscow 117975, Russia
PANCZER, G., Laboratoire de Physico-Chimie des Materiaux Luminescents Universite Claude Bernard-Lyon 1, 69622 Villeurbanne Cedex, France
PENTINGHAUS, H., Kernforschungszentrum Karlsruhe, Institut für Nukleare Entsorgungstechnik. Postfach 3640, D-76021 Karlsruhe, Germany
PHILIPSBORN, H., Abt. Kristallographie, Universitäts Regensburg, Universitätsstr. 31, D-93053 Regensburg, Germany
PÖLLMANN, H., Fachbereich Geowissenschaft, Universität Halle-Wittenberg, Domstr. 5, D-06108 Halle, Germany
RIETMEIJER, F. J. M., Department of Earth and Planetary Sciences, University of New Mexico, Albuquerque, New Mexico 87131-1116, USA
ROZANOV, A. YU., Paleontological Institute, Profsoyznaya 123, Moscow 117868, Russia

RYABCHIKOV, I. D., Institute of Ore Deposit Geology, Mineralogy, Petrology, and Geochemistry, Academia of Sciences, Staromonetny 35, Moscow 109017, Russia
SAXENA, S. K., Institute of Earth Sciences, Uppsala University, S-75236 Uppsala, Sweden
SHARKOV, E. V., Institute of Ore Deposit Geology, Mineralogy, Petrology, and Geochemistry, Academia of Sciences, Staromonetny 35, Moscow 109017, Russia
SHIGLEY, J., Gemological Institute of America, 5355 Armada Drive, Carlsbad, San Diego County, California 92008, USA
SNETHLAGE, R., Bay. Landesamt für Denkmalpflege, Hofgraben 4, D-80539 München, Germany
SNYDER, G. A., Planetary Geosciences Institute, Department of Geological Sciences, University of Tennessee, Knoxville, Tennessee 37996-1410, USA
TAYLOR, L. A., Planetary Geosciences Institute, Department of Geological Sciences, University of Tennessee, Knoxville, Tennessee 37966-1410, USA
ULYANOV, A. A., Department of Mineralogeny, Moscow State University, Moscow 119899, Russia
WYNN-WILLIAMS, G., University of Hawaii at Manoa, Institute for Astronomy 2680 Woodlawn Drive, Honolulu, Hawaii 96822, USA
YAKHONTOVA, L. K., Department of Mineralogy, Moscow State University, Moscow 119899, Russia
ZHARKOV, V. N., Institute of Physics of the Earth, Bolshaya Grusinskaya 10, Moscow, Russia

Abstract of Volume 4. Processes of Mineral Formation: Frontiers in Experiment and Evolution in Geological History

Theoretical background of the physical chemistry of mineral formation. Thermodynamics and thermochemistry of minerals. Paragenetic analysis of magmatic and metamorphic rocks.
Experimental studies of mineral formation: systematics and overview of principal results.
Thermobarogeometry. List of mineral thermobarometers. Summary of P-T characteristics of principal mineral-forming processes.
Synthesis of minerals.
Geodynamic types of mineral formation in the earth's history.

Abstract of Volume 5. Minerals as a Source of Metals, Energy, and Materials

All 4500 mineral species are distributed between genetic and economic types of mineral formation with characteristics of their genetic position and industrial importance.

CHAPTER 1

Mineral Matter in Space

1.1 Types of States of Matter in the Universe

A.S. MARFUNIN

The extended scope of mineralogy, including extraterrestrial materials, came first from increasingly sophisticated studies of meteorites, then from direct studies of lunar samples, then from the comparative mineralogy of terrestrial and giant planets, and finally from data on interplanetary dust and interstellar presolar mineral dust.

This is, however, not only an extension by the involvement of new objects. The mineral state of matter is now considered as a natural type of the system of types of matter in the Universe. It is the final extension of the term mineral matter.

The concept of the Universe as a whole represents the largest entity that can be studied or imagined. There are two approaches to understanding it which can be called geometric and evolutionary.

The geometric approach is based on a model of the homogeneous isotropic Universe, the model "dust of galaxies". It considers the geometric future of the Universe, depending on either Riemanian geometry, leading to closed space and the collapse of the Universe, or Lobachevsky (open space) and Euclidian (flat space), leading to infinite expansion.

Most contemporary estimations of the average density of the Universe indicate its geometric future as corresponding to open (or flat) space and infinite expansion.

The evolutionary approach considers the Universe as a whole as an evolutionary series of gravitational (and postgravitational) transformations, as a system of the types of matter; a frame for this Universe is a density-temperature diagram with absolute maxima.

A principal complexity exists in the construction of a whole picture of the Universe from the study of its parts. On the one hand, for each of these parts, summarizing surveys are available which can be used to present the Universe as a whole: general astrophysics and cosmology, particle physics and relativistic cosmology, thermonuclear physics and synthesis of elements, equation of states in astrophysics, cosmochemistry, evolution of stars, protostars, and protoplanets, stellar atmospheres, white dwarfs, neutron stars, black holes, very low mass stars and brown dwarfs, giant planets, Solar System, interstellar dust, meteorites, asteroids, and comets.

On the other hand, each of these fields is self-sufficient and self-contained, operating within the framework of accepted concept, basic equations, formalisms, specialized mathematic and theoretical apparatures, and enormous masses of available data.

To bring together these components of the whole Universe, the component types of the states of matter must be presented in a single system.

Density and temperature are measures of expansion and cooling of the earlier Universe and also of gravitational compression and heating in galaxy

formation. They are the coordinates of the antigravitational and gravitational evolution of the Universe. They consider the whole evolution of the Universe in this single coordinate system, without omissions, in a physically and logically exhaustive manner.

The origin of the coordinates can be taken at minimum values of density and temperature of the now existing Universe: less than about 10^{-30} g cm^{-3} and less than 2.7 K, or, extrapolating to time corresponding to proton lifetime (more than 10^{30} years), in the order of 10^{-15} K.

To obtain a closed space of the diagram it is necessary to find the absolute maxima of temperature and density.

In the Universe, the evolution and antropicity of which are determined by fundamental physical constants, for these maxima the values of the Planck density and temperature, which are related only to the fundamental constants, can be taken:

$$\rho_{Pl} = c^5/G^2 2\,\hbar = 5\times10^{93}\ \text{g cm}^{-3} \quad \text{and} \quad T_{Pl} = 1/k(c^5\cdot\ \hbar/G)^{1/2} = 10^{32}\,\text{K}$$

(c – light velocity, G – gravitation constant, $\hbar$ – Planck constant, and k – Boltzmann constant).

In the expanding Universe model these maxima correspond to the values of the Big Bang singularity.

The closed space thus obtained offers the possibility of inscribing the whole infinite Universe within the framework defined by these coordinates and absolute values. A model of the Universe including the entire diversity of states, at all distances up to 10–20 billion light years, for all the billions of galaxies and trillions of stars in each galaxy, from all times from the beginning to the end of the Universe, can be constructed based on this big square of the Universe (Fig. 1).

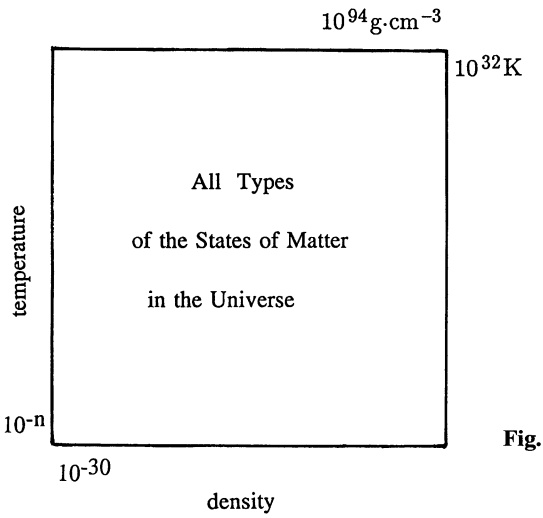

Fig. 1. The frame for the Universe

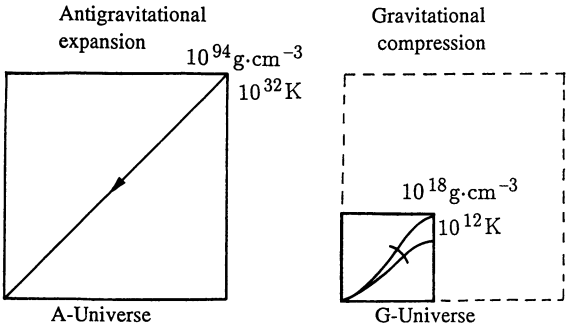

Fig. 2. Division of the evolution of the Universe into A – antigravitational and G – gravitational Universes

- Motive force: Big Bang
- Hot origin
- Linear relation T–t–R
- Pregalactic homogeneous the universe with temporal structure
- From absolute maxima down to ρ, T minima
- First seconds, minutes and up to hundreds of millions and billion years
- Noncreative evolution; dissipation of energy

- Motive force: gravitation; no external force
- Cold origin
- Relations determined by gravitational evolution
- Galactic
- From ρ, T minima up to 10^{12} K and 10^{16} g cm^{-3}
- All next 15–20 billion years and all the future of the Universe
- Creation of galaxies, stars, planets, life

First Fundamental Division in the Evolution of the Universe; Discerning Two Universes. When trying to inscribe into the big square of the Universe all possible states of matter, two groups of states with different trends and times can be distinguished. This corresponds to the most striking initial and fundamental division in the history of the Universe.

Two epochs are distinguished (Fig. 2). whose evolution followed different models and mechanisms, with different origins and opposite directions of motive forces and, different orders of temperature and density:

A: Pregalactic homogeneous initial Universe. Antigravitational expansion and cooling. Hot origin. Motive force: Big Bang. Linear relations ρ – T – t – R (density – temperature – time – radius of the Universe). The Universe with temporal structure. Homogeneous evolution from absolute maxima down to ρ – T minima. Epoch of the first seconds, minutes, and up to hundreds of millions and the first billion years. This is noncreative evolution; dissipation of energy. Transient states. Extinct Universe.

G: Galactic Universe. Gravitational compression and heating. Cold origin. Motive force: non external force, only gravitation. Fragmentation into galaxies. Evolution from ρ – T minima up to about 10^{12} K and 10^{16} g cm^{-3}. Epoch of the next 15–20 billion years and all the future of the Universe. Creation of galaxies, stars, planets, life.

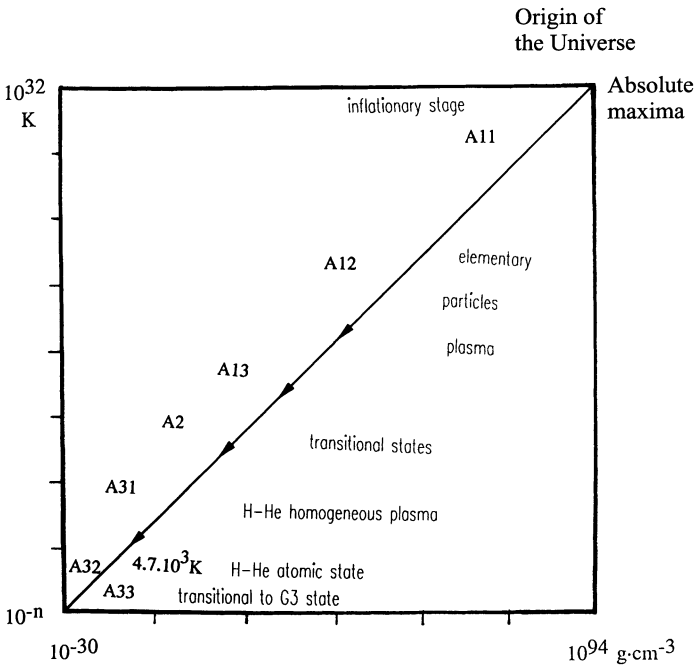

Fig. 3. The types of the states of matter in the A-universe

- Antigravitational expansion and cooling
- Linear relations ρ–T–t–R
- Pregalactic, homogeneous
- Hot origin
- The Universe with temporal structure
- First seconds, minutes up to hundreds of millions and the first billion years
- Extinct Universe

The distributions of the states of mater are completely different for the A- and G-Universes.

General Picture of the A-Universe. Figure 3 describes the behavior with classical simplicity: a straight line drawn by its evolution and traversing all orders of the chosen parameter values:

- from the absolute maxima of the Planck 10^{32} K and 10^{94} g cm^{-3} at the beginning of the Universe (upper right vertex of the square corresponding to the singularity, the Big Bang);
- down to the minima of the parameters near the origin of the coordinates.

All other parts of the diagram are not realizable.

General Picture of the G-Universe (Figs. 4–5). This is not linear, but represented by the entire space limited by about 10^{12} K (i.e., in the stability field of

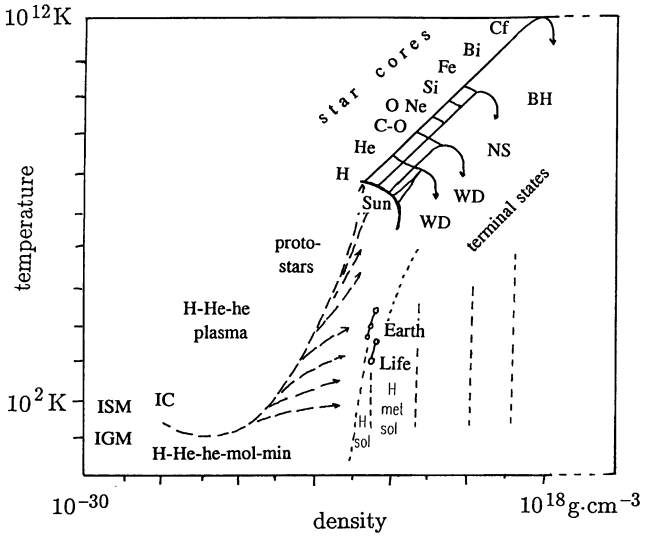

Fig. 4. The G-Universe: ascending states; evolutionary trends

- Interstellar and Intergalactic H-He-he medium
- (Hydrogen-helium-heavier elements)
- Interstellar clouds (molecular-mineral dust)
- Protostars and protoplanets
- Stellar nucleosynthesis
- Terminal states: white dwarfs, neutron stars, black holes
- Mineral states. Stuff of life

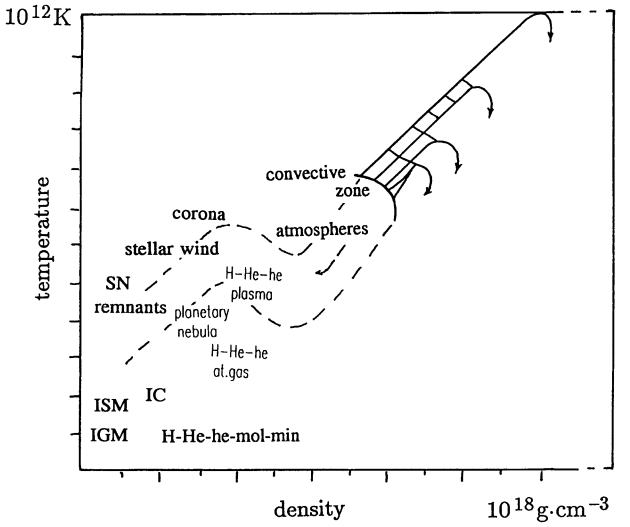

Fig. 5. The G-Universe: descending states

- Star envelopes; convective zone
- Atmospheres, corona
- Stellar wind
- Planetary nebula
- SN remnants

protons and neutrons before transition to quarks) and 10^{16} g cm^{-3} (nuclear matter states).

Thus, the frame of the galactic G-Universe is inscribed in the part of the big square which is lower than the elementary particle field, but covers all combinations of T and ρ in these boundaries.

Temporal Structure of the Pregalactic A-Universe. This results form the preservation of its homogeneity throughout the whole length of its existence; fluctuations do not develop into structural fragmentation. There are series of transient momentary states filling the whole A-Universe in its expanding space. At every moment, the Universe is homogeneous and the momentary states fill it entirely. At any moment in time the whole Universe is described not by a field or line on the ρ – T diagram but by a "running point": there is nothing behind it ("all bridges are burned"), and there are states ahead of it which have never existed before.

This is Universe plasma, Universe light; the Universe a single nonstructured star; at the end of this epoch, there is Universe darkness, nearly emptiness, nearly ultimate coldness, darkness without stars and radiation, without any hint of future, without a sign of a possibility for stars, minerals or intelligence.

Only in the A-Universe do the linear T–ρ–t–R relations exist. The line of its evolution can be identified with the "arrow of time" divided at time-temperature intervals according to the relation: $T(K) = 10^{10}\sqrt{t}\,(s)$.

Directions of Evolution. These are opposite in the A- and G-Universe: in the first, the processes accompany decreasing temperature, expansion, dissipation of energy, and increase in entropy, in the second, gravitational compression, and increase in temperature and energy.

Moving Force. In the A-Universe, this is the inertia of the Big Bang impetus, antigravitational repulsion. This is a single trust in the evolution of the Universe, the only moving force resulting in limitless expansion in time and space. No other forces besides the Big Bang inertia are able to spread the matter of the Universe forever. This inertia of the primordial push, which occurred 15–20 billion years ago, continues to be the single cause of the expansion of the Universe, even after its transition form the A- to the G-epoch.

The moving force in the G-Universe is gravitation, and its action is of two kinds: (1) as the initial cause of the transformation of matter at all stages of the galactic evolution, change in the composition of the Universe from a hydrogen-helium medium to a synthesis of all chemical elements, then to molecules and minerals, to formation of galaxies, stars, planets, and (2) as gravitational mechanisms of celestial mechanics in fragmented hydrogen-helium masses and celestial bodies, media, and particles.

Relations of the A- and G-Universe. These are two separate temporal layers, two epochs in the existence of the Universe. The first epoch elapsed and will never

recur in this Universe; this is a transient, extinct Universe. The second exists now and comprises all observable diversity of the Universe from the interstellar medium to stars of all types and planetary systems and life.

All types of states in the Universe can be distributed between three diagrams: for the A-Universe, for the G-Universe ascending states, and for the G-Universe descending states.

A1: The Elementary Particles Universe. One of the fundamental states of matter and the first in the evolution of the Universe. The whole of matter was only in this elementary particles state. There were no compounds, no atoms, no nuclei, no protons or neutrons (and there was no place for thought and word). The entire Universe was composed of this type of matter alone.

- State of elementary matter: more than 300 particles in continuous transformation in other particles, radiations and resonances; annihilation and formation of particle-antiparticle pairs; ephemerality, nondetermination. Unique scale of particle lifetimes and relations of matter – time – space. Total time of existence is about 1 s.
- Represents the largest part of Universe conditions: from 10^{32} to 10^{12} K and from 10^{94} to 10^{14} g cm^{-3}, i.e., 20 orders of temperature and 80 orders of density.
- These particles are not "building stones" (protons, neutrons) for all other types of matter. These elementary particles neither enter into states of the next types of matter, nor compose them. This state was transformed into other types of states and ceased to exist. This is a state of the past, extinct, nonquenchable Universe.
- A1 and A2 are the only states with antiparticles. Antimatter was not separated into a phase; no "antiworlds" existed.
- Limit to subdivision of matter. Limit to infinity in depth.
- First picosecond is the time of the inflationary Universe; inflationary cosmology concerns this first picosecond.
- No primordial chaos; supersymmetry.

There are three subtypes related by phase transitions:

A11: Particles states with supersymmetry interactions (great unification theory for strong and electroweak interactions); 10^{32}–10^{27} K;
A12: Separation of strong and electroweak interactions; 10^{27}–10^{15} K;
A13: Separation of strong, weak, and electromagnetic interactions; 10^{15}–10^{12} K;

A2: Transitional States (from Elementary Particles to Hydrogen-Helium Medium).

A21: Formation of protons and neutrons from quarks; end of free quark state; continuous annihilation and formation of proton-antiproton, neutron-antineutron, and electron-positron, pairs.

A22: Termination of the proton and neutron formation (threshold temperatures 1.0888×10^{10} and 1.0903×10^{10} K; annihilation of equal amounts of protons and antiprotons, neutrons and antineutrons. Proton and neutron surplus (baryon asymmetry) 10^{-9} composes the entire subsequent matter of the Universe.
Initial equal ratio of the survived neutrons and protons changed and stabilized at 5×10^{9} K as n:p ~ 0.2.
Surviving part of electrons from electron-positron annihilation at a threshold temperature of 5.930×10^{10} K.
At this time, the initial mass of the Universe and the total amount of protons and neutrons with their corresponding electrons were determined. End of antiparticles.

A23: Start of nuclei formation from all neutron and corresponding amount of protons: helium ^{4}He(2p + 2n) with a small admixture of deuterium (2p) and some other isotopes of light elements (Li, Be, B).

Thus, at the end of the transitional states at 5×10^{9} K in about 3 min after the Big Bang the final composition of the principal components of the Universe was established: $H_{90}He_{10}$ (atomic ratio) or $H_{75}He_{25}$ (mass ration) with a negligible admixture of some light elements.

A3: Primordial H–He Homogeneous Universe. This was the primitive Universe with the simplest composition, $H_{90}H_{10}$, and traces of light elements with no other elements: without Si, Al, O – elements of minerals and planets, without C, O, P, N – elements of life and without a hundred other elements. This was the pregalactic variant of cosmic space as homogeneous primitive Universe without stars and planets.

A31: H–He plasma.

A32: H–He atomar gas (H and He recombination at 4.7×10^{3} K in about 140 000 years from the Big Bang).

A33: Transitional to the galactic Universe state: from A3 to G3. The A3 and G3 states are similar but have two principal distinctions. (1) Relations between the states are determined by the phase supertransition of the entire Universe from homogeneous A-states to inhomogeneous galactic G-states. (2) There are heavier elements in the G-Universe which compose all the forms, bodies, and colors of the world, and all stars and planets, and which are absent in A-states. Duration of the A3 state in determined by (1) the time necessary for the expansion of the Universe to dimensions which permit the arising of the initial galaxys protosuperclusters, (2) the cooling down to temperatures permitting gravitational evolution of inhomogeneities and their fragmentation into galaxies and stars. Hence, uncertainty in duration estimations: 100 K reached in 300 million years, 50 K in 1 billion years. Probably these inhomogeneities in A33 descend genetically from the initial fluctuations already present in the A1 elementary particle state.

G3: cosmic H–He–he Space (Hydrogen-Helium – Heavier Elements).

- On the one hand: it is not emptiness, on the other hand: it is a "vacuum" still many orders higher than the superhighest technical vacuum 10^{-14} g cm^{-3}. It is a "cosmic vacuum": 10^{-30} g cm^{-3}.
- But it is populated (by H–He–he) and this extremely sparse population represents the whole building material for all other states of matter from stars to minerals and life.
- Formula of space composition $H_{90}H_{10}[he_{0.001}]$.
- Always and everywhere in cosmic space, all elements occur.
- The whole volume of space, nearly the whole Universe, is the H–He–he medium. But most of the mass of matter of the Universe (90%) is contained in stars. Second fundamental division the evolution of the Universe: ascending states (evolution trends) and descending states (star outflows).
- Ascending states in the H–He–he space: interstellar clouds-protostars and protoplanets – star envelopes.
- Descending states: star backscattering of H–He–he matter from convective zones, outer envelopes, and atmospheres of stars to corona, stellar wind, planetary nebula, hot ionized gas, cosmic rays, and so on; in all cases it is always H–He–he-plasma.

G31: H–He–he molecular gas and interstellar mineral dust.
G32: H–He–he atomic gas.
G33: H–He–he plasma.

G4: Thermonuclear Stellar States; Synthesis of Elements.

- Star cores: gravitational transformation in the evolution of the Universe occurs only here. Formation of elemental composition of the Universe.
- Star envelopes: backscattering of H–He–he matter, supply space by building material for minerals, planets, and life.

Genetic System of Elements. Consecutive packing of protons and neutrons in nuclei of elements due to gravitational evolution.

Primordial hydrogen; pregalactic helium (and lightest isotopes); main sequence H → He; synthesis He–Fe by fusion; synthesis Fe → Cf by neutron capture ("slow" and "rapid" processes); "non-Mendeleyevian elements" with excess of neutrons; neutronization.

Gravitational evolution of the Universe represents essentially the synthesis of elements. It covers the whole series from pure proton to pure neutron states.

Genetic Classification of Stars.

1. Core envelope states of stars: main sequence, red giants.
2. Separated cores and envelopes:

- Envelopes → coronas, stellar wind, planetary nebulae, dissipation in Space, all H–He–he plasma states.
- Cores → gravitational evolution.

G41: Thermonuclear plasma; synthesis from He to Fe.
- G411: Main sequence; H → He.
- G412: Synthesis from He to Fe; nondegenerate electrons.
- G413: Degenerate electrons; white dwarfs.
- G414: Plasma crystallization; metallic star cores.

G42: Synthesis of heavy and superheavy elements. Supernovae.
- G421: "Slow" processes; Fe to Bi.
- G422: "Rapid" processes; Fe to Cf.

G43: Neutronization. Neutron stars.
- G431: Neutronized nuclei of "non-Mendeleyevian elements"; neutron nuclei.
- G432: Neutron superfluid state.

G44: Quark-gluon plasma ("quagma"). Black holes.

G5: Mineral State of Matter. The current understanding of matter is related intuitively to matter of the visible world and then transposed to matter in general; and this matter is described as infinitely diverse. However, in the gravitational evolution of the Universe, the whole diversity of terrestrial (planetary) matter, inorganic and organic, crystalline, amorphous, melts, solutions, natural and technogenic, all minerals and materials, constitutes only one type of matter.

Common to all these objects (and distinct from all other states considered above) is the existence in the form of compounds, in a state of chemical bonding, crystal structures, and stereochemistry, of combinations form 104 elements. Their entire diversity is restricted by this single type of matter. Its diversity is the diversity of species and individuals.

It can be named the mineral type of matter, according to the original and predominant interstellar mineral dust and celestial mineral bodies. It constitutes a negligible part of the volume and mass of the Universe, but the whole diversity of matter, its colors and forms, manifest themselves only here.

G51: Interstellar mineral dust and molecules. Largest area of mineral formation; bulk amount of mineral dust in the galaxy is about 60 trillions of Earth masses. Occurs everywhere in all cold regions of all galaxies. The only source of matter for formation of planets and life. Nongravitational formation: mineral condensation from cold H–He–he medium.

G52: Celestial mineral bodies: planets, asteroids, meteorites, comets.

G53: Synthetic compounds.
- G531: Crystalline, amorph, melts, solutions.
- G532: Interactive materials in electronics and technologies, this is a "new race of materials".

G6: Stuff of Life. This can be considered as a carbon-based variety of the mineral type of matter: both are represented by compounds in a state of chemical bonding. Genetically, mineral matter precedes and accompanies the stuff of life; minerals are a substratum of life. Planetary conditions provide only parallel realization of biological and geological evolution.

The principal distinction between stuff of life and minerals is its existence in the form of molecule organizations capable of interaction with the environment, of self-organization and biological evolution. Minerals and materials are compounds, while life is organisms.

There is only one possible composition for the stuff of life: carbon compounds (with hydrogen, oxygen, etc.) because of the existence of the only possible system of elements, and due to the unique ability of carbon to form large C–H–O-based molecules.

Summarizing the foregoing descriptions leads to the "types of matter" concept.

The whole visible world represents a type of matter, called the mineral type, which is only one of the types of matter. Other types of matter exist, fundamental and distinct from each other. The diversity of matter is not boundless; there are a finite number of types (form A1 to G6), together composing matter in general.

The types of matter constitute the evolutionary series of the Universe, complete (without blanks in the series) and with two ends: the beginning of matter (and beginning of time, space, and the Universe) and the terminal states of matter. Each of them has its place and significance in the evolution of the Universe.

The concept "terminal states" designates the end of the evolutionary series of the Universe. States are terminal when they have completed their gravitational transformations due to the exhaustion of a star's gravitational evolutionary resource, limited by the mass of the star.

Depending on the initial mass of a star, a terminal state can be represented by white dwarfs with different elemental composition, by neutron stars with different stages of neutronization, and black holes.

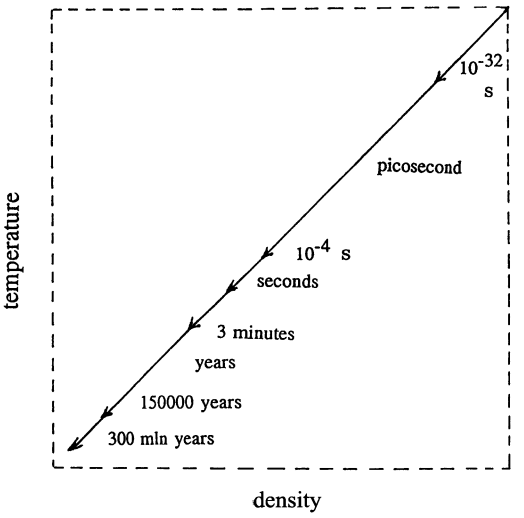

Fig. 6. Arrow of time (time in the pregalactic A-Universe with temporal structure)

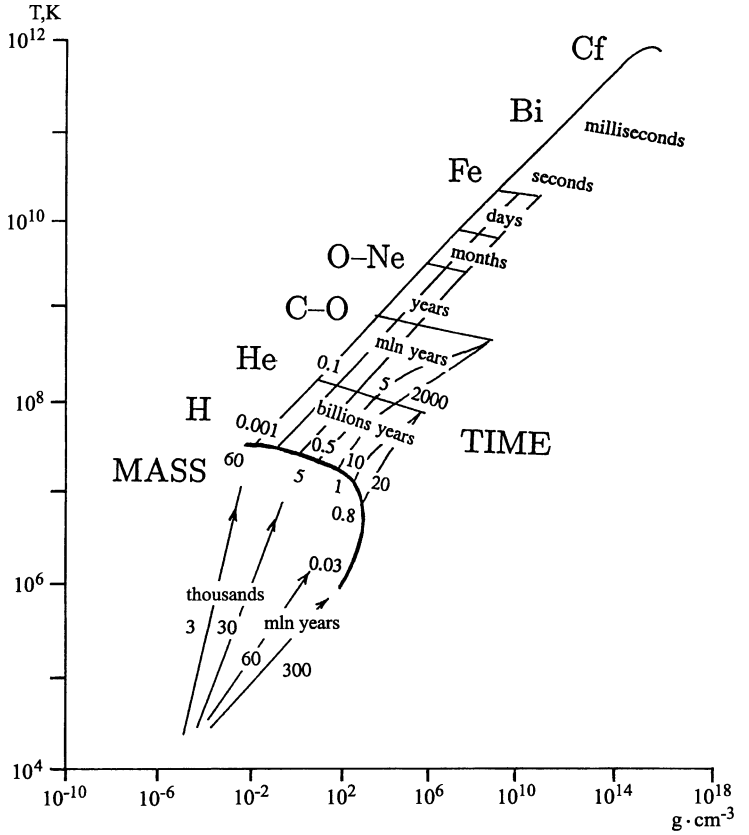

Fig. 7. The well-tempered Universe. (Algorithm of time depending on mass of stars and protostars). This is part of Fig. 4.
Inner side of the arc (main star sequence, corresponding to hydrogen burning): masses of stars are indicated (60; 5; 1 solar mass; 0.8; 0.03). *Outer side of the arc* (Time of stay of stars with different masses in the main sequence (hydrogen burning): 0.001; 0.5; 10; 20 billion years). *Next rows* correspond to times of burning of other elements in stars with different masses: million years, years, months, days, seconds, milliseconds. *Below left* Time of protostars for corresponding star masses

Stars do not disappear, but extinguish and enter terminal states. Terminal states do not evolve further, and are stable and eternal. Mineral states form and exist as terminal states (if not destroyed by external factors). The gravitational evolution of matter in the Universe is finite. The matter of the Universe is eternal in terminal states.

The existence of a frame for the Universe, and a finiteness of the evolutionary series determines the frame and finiteness of time. Time once arose, beginning with the beginning of matter, i.e., with the origin of the Universe. There are amounts of time. In the beginning, the whole of time comprised fractions of a second, now it is 15–20 billion years. The greatest part of time as a whole belongs to the future of the Universe.

Minerals have no proper (evolutionary) time. They form at once in terminal states, which are invariable in time and carried by the flow of geological time.

Time in the Universe is calculable time. The measure of general time is the expansion of the Universe. All times in the evolution of matter are calculated or calculable.

The arrow of time represents this calculation for the pregalactic Universe; it was substantial significance in the density-temperature diagram (Fig. 6). Times of stellar evolution, depending on the mass of stars, compose a temporal algorithm for the galactic Universe.

It can be compared with the structure of a fugue in music. By analogy with the wohltemperiertes Klavier of Bach, it can be described as a well-tempered Universe (Fig. 7).

The calculability of time of the evolution of matter permits the description: "evolutionary determinism" of the Universe.

The suggested ρ–T system arranges events in the whole Universe and coordinates the results of many fields of studies involved in the modeling of the Universe.

Empirical arrangement of the states of matter in the Universe in the density-temperature diagram leads to the fundamental division of Universe evolution, to the system of the types of matter, to the evolutionary model of the Universe, and the definition of time, space, matter, and infinity.

References

Bailey ME, Club SBM, Napter VM (1990) The origin of comets. Pergamon Press, Oxford
Beatty JK, Chaikin A (eds) (1990) The new solar system. Cambridge University Press, Cambridge
Boss AP (1985) Collapse and formation of stars. Sci Am 252:4–11
Burrows A, Hubbard WB, Lunin JI (1989) Theoretical models of very low mass stars and Brown Dwarfs. Astrophys J 345:939–958
Chabrier G, Shatzman E (eds) (1993) The equation of state in astrophysics. Proc IAU Coll No 147, Cambridge University Press, Cambridge
Edmunds ME, Terlevich RJ (eds) (1992) Elements and cosmos. Cambridge University Press, Cambridge
Encrenaz T, Bibring JP (1995) The solar system. Springer, Berlin Heidelberg New York
Gehrels T (eds) (1982) Protostars and planets. Studies of stars formation and of the origin of the solar system. University of Arizona Press, Tucson
Hawking St (1988) A brief history of time. From the Big Bang to Black Holes. Bentam Books
Heide F, Wlotzka F (1995) Meteorites. Springer, Berlin Heidelberg New York
Koester D, Wernez K (1995) White Dwarfs. Springer, Berlin Heidelberg New York
Linde A (1990) Particle physics and inflationary cosmology. Harwood Academic Publishers, Chur
Lipunov VM (1992) Astrophysics of neutron stars. Springer, Berlin Heidelberg New York
Luminet J-P (1992) Black holes, Cambridge University Press, Cambridge
Mihalas D (1978) Stellar atmospheres. WH Freeman, San Francisco
Prantzer NE, Vangioni-Flani M, Casse M (eds) (1992) Origin and evolution of the elements. Cambridge University Press, Cambridge
Silk J (1980) The Big Bang. The creation and evolution of the Universe. WH Freeman, San Francisco

Tenkolsky Sh (1983) Black holes, white dwarfs, and neutron stars. Wiley, New York
Weinberg S (1977) The first three minutes. Basic Books, New York
Whittet DCB (1992) Dust in the galactic environment. Hilger
Winnewisser G, Pelz GC (eds) (1995) The physics and chemistry of interstellar molecular clouds. Springer, Berlin Heidelberg New York
Wynn-Williams S (1992) The fullness of space: nebulae, stardust, and the interstellar medium. Cambridge University Press, Cambridge
Zharkov VN, Gudkova TV (1992) Modern models of giant planets. In: High-pressure research. Terra Sci Publ, Tokyo, pp 393–401

1.2 Interstellar Dust

C.G. WYNN-WILLIAMS

Interstellar matter comprises about 10% of the mass of the Milky Way galaxy. About 0.7% of interstellar matter is in the form of microscopic dust grains; most of the remainder is hydrogen or helium gas. As far as we know, there are no liquids in space. Interstellar matter exists both as a diffuse medium that fills the gaps between the stars and as comparatively dense clouds that sometimes take the form of bright or dark nebulae. Under different interstellar conditions the gas may be molecular, atomic, or ionized, with temperatures anywhere from less than 10 to over 10^6 K. In the vicinity of the solar system, gas atoms are separated from each other by distances of the order of 1 cm, while individual dust particles are separated from each other by hundreds of meters. Because interparticle collisions occur so infrequently, the gas and dust are not necessarily in thermal equilibrium with each other. The dust temperature ranges from less than 10 K in dense molecular clouds, to over 1000 K in stellar winds and in the vicinity of newly forming stars.

There is great uncertainty about the physical and chemical nature of interstellar dust. We have clues that indicate that certain materials exist in space, including silicates, graphite, and ice, but many of the data are somewhat ambiguous. No interstellar particles (as opposed to interplanetary particles) have been collected on Earth, although it has been argued that certain species found in meteorites must originally have been interstellar. Current ideas about the nature of interstellar grains come from studying their interactions with starlight, from constraints on the elemental composition of dust based on cosmic abundance arguments, and from infrared and ultraviolet spectral features.

Interactions with Starlight

The most easily observable property of interstellar dust is its ability to absorb and scatter light from background stars. This property is called interstellar extinction (see Mathis 1990 for a review). Short-wavelength light is absorbed

and scattered more than long-wavelength light, giving rise to the phenomenon of interstellar reddening of the light from distant stars. If a dense interstellar cloud lies close to a bright star, the scattered light may be observable directly as a reflection nebula. Studies of reflection nebulae indicate that dust grains have albedos of the order of 0.5 at visible wavelengths.

Starlight that is absorbed (as opposed to scattered) by a dust grain is reradiated into space at infrared wavelengths. The plane of the Milky Way Galaxy is very bright in the 30–300 μm range as a result of dust grains heated to equilibrium temperatures of 10–100 K in the interstellar medium.

Abundance Constraints

Hydrogen and helium cannot solidify under interstellar conditions. Dust must therefore consist mainly of compounds of the more common heavy elements such as oxygen, carbon, and nitrogen, with significant contributions from hydrogen and from the next most common elements: silicon, magnesium, iron, and sulfur. Supporting evidence for this assumption comes from the observation that the relative abundances of some of these elements is much lower in interstellar gas than in the atmospheres of stars – 100 times lower in the case of iron. The widely accepted explanation for these depletions is that the missing elements are locked into dust grains. The most depleted elements are generally those which would condense into dust grains at the highest temperatures, a result that supports the view that grains form in the expanding, cooling winds that blow off the surfaces of giant stars.

Spectral Absorption Features

The strongest interstellar spectral absorption feature lies in the ultraviolet band at 0.22 μm. The most likely carrier is graphite, though other carbonaceous materials have been proposed, including amorphous carbon, quenched carbonaceous composites, and polycyclic aromatic hydrocarbon molecules (see below).

The presence of silicate particles in interstellar dust is deduced from the 9.7 and 18 μm absorption features. The shape of the 9.7-μm feature does not correspond well with any known terrestrial mineral. The discrepancy may be due to the difference in particle sizes between interstellar and laboratory samples, or possibly to the interstellar silicates having an amorphous rather than a crystalline structure. The 11.7-μm feature of silicon carbide has been seen in the immediate surroundings of certain carbon-rich stars, but has not yet been detected in the general interstellar medium.

An absorption feature at 3.4 μm is probably due to C-H stretching in aliphatic hydrocarbons, but a more precise identification cannot be made. A deep absorption feature at 3.1 μm, and a weaker one at 6 μm are attributed to water ice. These features are seen only in dense interstellar clouds, where tempera-

tures are lower and destructive radiation fields are weaker than in the general interstellar medium. Evidence for frozen carbon monoxide and ammonia has also been found.

It is not clear whether the diffuse interstellar absorption bands, which are seen in the visible spectra of reddened stars, have a dust or a molecular origin; in any case, attempts to identify them spectrally have so far met with little success (see Herbig 1995 for a review).

Dust grains that are subject to strong ultraviolet radiation fields display a number of broad emission features at infrared wavelengths. The most prominent are at 3.3, 6.2, 7.7, 8.6, and 11.3 μm. The features have been tentatively identified with polycyclic aromatic hydrocarbon (PAH) molecules, though other identifications have also been suggested. PAHs consist of 10–100 carbon atoms bound into linked benzene-like rings, with hydrogen atoms around the edges. Examples are pyrene and coronene. Emission from PAH molecules is often seen in conjunction with emission from very small grains (see below); PAHs may represent the small end of a continuous size distribution of particles that blur the distinction between molecules and solid grains.

Sizes and Shapes of Dust Grains

Comparison of the observed wavelength dependence of interstellar extinction with theoretical models based on Mie scattering theory indicates that at least some dust grains have diameters of the order of 0.1 μm. A more detailed model by Mathis et al. (1977) posits a power-law distribution of dust sizes with $dn/da \sim a^{-3.5}$ for $0.005 < a < 0.2$ μm. There is some evidence that grains inside dense clouds are larger on average than those in the diffuse interstellar medium; the increase in size may be due to the formation of ice mantles around silicate grains.

There is also evidence for the existence of very small grains (VSGs) consisting of only 10^2–10^4 atoms. The heat capacity of such a grain is so low that a single visible-wave photon will temporarily raise its temperature to values far in excess of thermal equilibrium. VSG dust is detectable by its anomalously strong emission in the 2–20 μm wavelength range.

Almost nothing is known about the shapes of grains. Simple models usually assume sphericity, but needles and flat sheets (as in graphite) have also been considered. The only direct evidence concerning the shapes of dust grains comes from the observation that starlight that has passed through large column densities of interstellar matter usually emerges slightly polarized. The generally accepted explanation for this polarization is alignment of nonspherical grains by interstellar magnetic fields.

Books that provide a starting point for general studies of the interstellar medium include the nontechnical account by Wynn-Williams (1992), the series of lectures by Burton et al. (1992), and the conference proceedings edited by Hollenbach and Thronson (1987) and by Blitz (1990). Useful works that deal

with interstellar dust per se are the monograph by Whittet (1992), the conference proceedings edited by Bailey and Williams (1988) and Allamandola and Tielens (1989), and the reviews by Mathis (1990) and Draine (1995).

References

Allamandola LJ, Tielens AGGM (eds) (1989) Interstellar dust. IAU Symp 135. Kluwer, Dordrecht, 525 pp

Bailey ME, Williams DA (eds) (1988) Dust in the universe. Cambridge University Press, Cambridge, 573 pp

Blitz L (ed) (1990) The evolution of the interstellar medium. Astron Soc Pacific, San Francisco, 346 pp

Burton WB, Elmegreen BG, Genzel R (1992) The galactic interstellar medium. Springer, Berlin Heidelberg New York

Draine BT (1995) Properties of dust in diffuse clouds. In: Ferrara A, McKee CF, Heiles C, Shapiro PR (eds) The physics of the interstellar medium and intergalactic medium. Astron Soc Pacific, San Francisco, pp 133–147

Herbig GH (1995) The diffuse interstellar bands. Annu Rev Astron Astrophys 33:19

Hollenbach DJ, Thronson HA (eds) (1987) Interstellar processes. Reidel, Dordrecht, 807 pp

Mathis JS (1990) Interstellar dust and extinction. Annu Rev Astron Astrophys 28:37–70

Mathis JS, Rumpl W, Nordsieck KH (1977) The size distribution of interstellar grains. Astrophys J 217:425–433

Whittet DC (1992) Dust in the galactic environment. Institute of Physics, London, 295 pp

Wynn-Williams CG (1992) The fullness of space. Cambridge University Press, Cambridge, 202 pp

1.3 Interstellar Diamond

A.V. Fisenko

Interstellar diamond (designated C_δ) was discovered in meteoritic matter in 1987.

The diamond was identified as presolar because of its isotopically anomalous xenon composition: it is simultaneously enriched in light isotopes ($^{124.126}$Xe) and heavy isotopes ($^{134.136}$Xe) with respect to solar Xe. This Xe–HL in the diamond phase carrier must have been formed by nucleosynthesis processes.

The grains of diamond are sited in a fine-grained matrix, and their abundance in chondrites reflects mainly the degree of metamorphism undergone. For carbonaceous chondrites the diamond abundance decreases in range CI (Orgueil ~ 0.1 wt.%) > CV (Vigarano ~ 0.5 wt%) ≥ CM (Murray ~ 0.04 wt.%) > CO (Kainsas ~ 0.02 wt.%). For unequilibrium ordinary and enstatite chondrites, the diamond abundance falls within the limit of 0.002–0.013 wt.%.

Interstellar diamond has been isolated from chondrites by corrosive chemical reagents (HCl, HF, $K_2Cr_2O_7$, $HClO_4$). The isolation of most pure diamond grains is based on their tendency to form a colloid at $pH \geq 5$ due to the presence of COOH groups at the microdiamond surface. The dry gel represents a brown matter with a density of 2.22–2.33 g/cm^3.

Microdiamond crystals have mainly face-centered cubic lattice structure with the parameter of the unit cell 0.3558 ± 0.0015 nm.

The mean size of diamond grains lies within 10–26 Å. This indicates that the diamond grains were formed as a result of growth and not of fragmentation of their more large predecessors. The kinetic parameters of the oxidation process in air atmosphere differ for interstellar diamond in chondrites of different chemical classes. Thus, for the Murchison CM2 diamond the activation energy is 233.0 ± 2.1 kJ/mol, for the Krymska LL 3.0 diamond 266.1 ± 6.3 kJ/mol.

These distinctions may be due to different PT conditions in the accretion process of the chondrite parent bodies and/or of the metamorphism process.

According to TEM analyses, diamond fractions contain also amorphous material. EELS (electron energy loss spectroscopy) shows the presence of sp^2-bonded atoms in addition to the sp^3-bonded atoms of diamond. The amorphous phase is most probably the hydrogenated surface of diamond grains, but data for the noble gas component in the amorphous phase indicate that it can be the discrete carbonaceous phase (designed C_ζ). The C_ζ-phase should be highly resistant to chemical reagents, but less thermostable than diamond. One candidate for C is the amorphous a–C:H phase.

Carbon in interstellar diamond is "normal", with an average of $\delta^{13}C \sim -33 - 40$‰. Why the carbonaceous phase carrier of anomalous presolar nucleogenous components has a solar $^{12}C/^{13}C$ ratio is an open question.

The main admixtures in interstellar diamond are hydrogen (10–40 at.%) and nitrogen (up to 1.5 at.%). Hydrogen is most probably sited in the amorphous phase. Hydrogen in diamond-enriched in deuterium relative to SMOW: $\delta D = 245 - 342$‰. The N abundance in diamond ranges form ~0.2 to ~0.9 wt.% and depends markedly on the degree of metamorphism of diamond-bearing chondrite: N abundance decreases with an increasing degree of metamorphism. The nitrogen in diamond is depleted in ^{15}N ($\delta^{15}N_{min} \sim -375$‰ relative to atmospheric N). It is possible that N in diamond fractions is either present in two phase carriers, differentialy thermostable to oxidation, or N is a two-component mixture which is heterogeneously distributed within the diamond grains.

Of the trace elements in interstellar diamond, the noble gases are best understood. Their abundances range from 2×10^{-2} to 6×10^{-2} cm^3/g for ^{4}He and from 2×10^{-7} to 5×10^{-7} cm^3/g for ^{132}Xe. Diamond contains almost all trapped He and Ne in chondrites. To the present two components of noble gases in diamond-bearing fractions have been most exactly identified. One of them, with almost "normal" (planetary) isotopic composition, was designated P3 component. Another, containing isotopically anomalous gases, was called HL component. At pyrolyses the P3 component is released at low temperature (< 900 °C), the

HL component at 1100–1600 °C. The phase carrier of the P3 component could be phase C_ζ. The HL component is present in diamond grains. In addition to the two components in diamond fractions, there is one further component, released at a temperature higher than the HL component. This third component either has almost normal isotopic composition (called P6) or is an HL subcomponent. The abundance of the P3 component ranges by more than by 2 orders in diamonds isolated from chondrites of different chemical classes and groups. This variation is most probably due to the different degree of metamorphism. At the same time, the abundance of the HL component in the diamond of these chondrites changes by a factor of $\lesssim 2$. The Xe-HL isotopic composition is also similar in all chondrite diamonds. The $^{124}Xe/^{132}Xe$ and $^{136}Xe/^{132}Xe$ ratios are equal to 0.0074 and ~0.642, respectively, almost twice exceeding the ratios for solar Xe. Kr in the HL component is enriched in heavy isotopes $^{84,86}Kr$ (Kr–H), but is depleted in ^{78}Kr. Ar in the HL component is enriched in ^{38}Ar ($^{38}Ar/^{36}Ar = 0.208$), and Diamond grains contain Ne-A2 ($^{20}Ne/^{22}Ne = 8.36 \pm 0.03$, $^{21}Ne/^{22}Ne = 0.035 \pm 0.001$), while the P3 component-Ne-A1 ($^{20}Ne/^{22}Ne = 8.4 \pm 0.08$, $^{21}Ne/^{22}Ne = 0.0299 \pm 0.0003$. Helium in diamond is enriched in ^3He ($^3He/^4He = 1.4 \times 10^{-4}$). Xe-Hl has almost no excess of radiogenetic ^{129}Xe.

At present, there are the following hypotheses for the formation of interstellar diamond:

1. Diamond grain formation by the Chemical Vapor Deposition (CVD)-process. This process is similar to the chemical process of vaporous matter precipitation. Laboratory experiments on epitaxial diamond growth show that the CVD process may occur in a hydrogen-rich medium at relatively low pressures and temperatures ($P < 1$ atm and $T < 1500$ K). Such conditions are present in some astrophysical objects with $C/0 > 1$ (atmosphere of carbon stars and red supergiants, and expanding He shell after a supernova explosion), and therefore the diamond grains can be formed by a CVD mechanism.
2. Diamond grain formation as a result of photolysis of hydrocarbons in the vicinity of stars.
3. Crystallizaton from a melt formed as a result of collision of graphitized carbon particles under the influence of shock waves. The probability of diamond grain formation in this process is estimated at ~5% and therefore diamond in chondrites should be accompanied by considerable amounts of initial carbon grains. These grains, like diamond, should contain anomalous Xe, Kr, and N. However, such carbon grains have not been found in chondrites, and therefore this diamond formation process seems unlikely.
4. Diamond grain formation from chemically connected carbon and/or from amorphous carbon (e.g., soot) in the vicinity of supernova in an extremely unequilibrated process. Shock waves may provide the energy for this process.

References

Allaerts L, Lewis RS, Matsuda J, Anders E (1980) Isotopic anomalies of noble gases in meteorites and their origin. Presolar components in the Murchison C2 chondrite. Geochim Cosmochim Acta 44:189–209

Anders E, Zinner E (1993) Interstellar grains in primitive meteorites: diamond, silicon carbide and graphite. Meteoritics 28:390–514

Bernatowicz TJ, Gibbons PC, Lewis RS (1990) Electron energy loss spectrometry of interstellar diamond. Astrophys J 359:248–255

Blake DF, Freund F, Krishnan K, Echer C, Shiff R, Bunch T, Tielens A, Lupari R, Hetherington C, Chang S (1988) The nature and origin of interstellar diamond. Nature 332:611–623

Buerki PR, Lentwyles S (1991) Homogeneous nucleation of the diamond powder by CO_2-laser-driven gas-phase reactions. J Appl Phys 69:3739–3744

Clayton DD (1989) Origin of heavy xenon in meteorite diamonds. Astrophys J 340:613–619

Fisenko AV, Verchovsky AB, Semjonova LF (1994) Noble gases in the interstellar diamond of Efremovka CV3 chondrite. Geokhimia N7:916–927 (in Russian)

Fisenko AV, Tatsy VF, Semjonova LF, Bolsheva LN (1995) Experimental studies of oxidation kinetics of the meteoritic diamonds by air oxygen. Lunar Planet Sci 26:397–398

Fraundorf P, Fraundorf G, Bernatowicz T, Lewis R, Tang M (1989) Stardust in the TEM. Ultramicroscopy 27:401–412

Huss GR (1990) Ubiquitous interstellar diamond and SiC in primitive chondrites: abundances reflect metamorphism. Nature 347:159–162

Huss GR, Lewis RS (1994) Noble gases in presollar diamonds: Three distinct components and their implications for diamond origins. Meteoritics 29:791–810

Huss GR, Lewis RS (1995) Presolar diamond, SiC, and graphite in primitive chondrites: abundances as a function of meteorite class and petrologic type. Geochim Cosmochim Acta 59:115–160

Jorgensen UG (1988) Formation of Xe-HL-enriched diamond grains in stellar environments. Nature 332:702–705

Lavrukhina AK, Fisenko AV (1994a) On the features and isotopic composition of elements composing the interstellar diamond, SiC and graphite in chrondites. Geokhimia N10: 1372–1382

Lavrukhina AK, Fisenko AV (1994b) On the origin of the interstellar diamonds, SiC and graphite in chondrites. Geokhimia N11:1539–1546

Lewis RS, Anders E (1988) Xenon-HL in diamonds from the Allende meteorite-composite nature. Lunar Planet Sci 19:679–680

Lewis RS, Tang M, Wacker JF, Anders E, Steel E (1987) Interstellar diamonds in meteorites. Nature 326:160–162

Lewis RS, Anders E, Draine BT (1989) Properties, detectability and origin of interstellar diamonds in meteorites. Nature 339:117–121

Nuth JA, Allen JE Jr (1992) Supernovae as sources of interstellar diamonds. Astrophys Space Sci 196:117–123

Ott U (1993) Interstellar grains in meteorites. Nature 364:25–33

Russell SS, Arden JW, Pillinger CT (1991) Evidence for multiple sources of diamond from primitive chondrites. Science 254:1188–1191

Swart PK, Grady MM, Pillinger CT, Anders E (1983) Interstellar carbon in meteorites. Science 220:406–410

Tang M, Anders E (1988) Isotopic anomalies of the Ne, Xe, and C in meteorites. II. Interstellar diamond and SiC: carriers of exotic noble gases. Geochim Cosmochim Acta 52:1235–1244

Tielens AGGM, Seab CG, Hollenback DJ, McKee CF (1987) Shock processing of interstellar dust: diamond in sky. Astrophys 319:L109–L113

Valter AA, Fisenko AV (1993) Diamonds in meteorites. Meteoritika 50:113–122 (in Russian)
Verchovsky AB, Russell SS, Pillenger CT, Fisenko AV, Shukolyukov YuA (1993) Are the C light nitrogen and noble gases located in the same carrier? Lunar Planet Sci 24:1461–1462
Virag A, Zinner E, Lewis RS, Tang M (1989) Isotopic composition of H, C, and N in C diamonds from the Allende and Murray carbonaceous chondrites. Lunar Planet Sci 20: 1158–1159
Wdowiak TJ (1987) Diamond formation in carbon-star atmosphere. Nature 328:385

1.4 Interplanetary Dust

F. J. M. Rietmeijer

Dust particles with diameters between 2–50 μm enter the Earth's atmosphere daily. These nano- to picogram dusts (densities form 0.3–4.2 $g\,cm^{-3}$) are not affected by gravitational forces, but will spiral towards the sun due to light pressure exerted by the solar wind. As these dusts cross the Earth's orbit, they enter its atmosphere. The interplanetary dust particles [IDPs] collected in the lower stratosphere are derived from solid solar system bodies that cover a wide range of heliocentric distance from the inner asteroid belt to 100s of AU (1 AU = 149 600 000 km). Both chondritic and nonchondritic particles (i.e., iron-sulfide and Mg-rich olivine grains) could cooccur at the surface of asteroids. Potential IDP sources of most interest are icy protoplanets (not sampled by meteorites) wherein solar nebula dusts were kept at cold storage for 4.56 Ga. They include carbon-rich icy asteroids at ~3.5–5.2 AU, comet nuclei (formed at 20–30 AU) that arrive in the inner Solar System form the Oort cloud, and comets from the Kuiper belt (~40–400? AU). The similarity between chondritic IDP compositions and this composition of CI carbonaceous chondrite meteorites and the solar photosphere show that they were not chemically fractionated during this time. Yet, various alteration processes left their imprint on carbon-rich chondritic IDPs, leaving considerable micrometer-scale heterogeity and nonequilibrium mineral assemblages. It is a challenge to this research to understand the origin(s) of the large numbers of carbonaceous and noncarbonaceous phases alike, and the presence of fully oxidized and reduced carbon, sulfur, and iron, often in the same particle. Another challenge is to recognize the original, or principal, components of these IDPs for a consistent model.

Chondritic Dusts

Original attempts to classify these dusts relied on morphology or mineralogy. That is, aggregate particles, viz. chondritic porous [CP], and less porous chondritic-filled [CF] IDPs, and compact particles, viz. chondritic smooth [CS] and

Advanced Mineralogy, Volume 3
Mineral Matter in Space, Mantle, Ocean Floor, Biosphere, Environmental Management, and Jewelry (ed. by A. S. Marfunin)

chondritic rough [CR] IDPs. The mineralogies allowed division into (1) particles dominated by neso- and ino-silicates plus carbons, and (2) particles dominated by layer silicates plus carbons. Using the *predominant* silicates, the anhydrous particles were subdivided into olivine-rich and pyroxene-rich particles. The hydrated IDPs included smectite-rich and serpentine-rich particles. The mostly anhydrous aggregate IDPs were linked to periodic comets. Compact IDPs that are dominated by phyllosilicates were linked to asteroids. This simple relationship between morphology, dominant silicates, and putative sources is no longer tenable. Using the peak heating temperatures during atmospheric entry (obtained by stepped-heating helium-release profiles) of particles of known size and density, it appears that CS and aggregate IDPs are derived from both asteroids and comets. The carbon-free CR IDPs resemble matrix materials in CI and CM carbonaceous chondrite meteorites and have asteroidal origins.

The typically carbon-rich (2–48 wt.% C) CP, CF, and CS IDPs are unique. They differ significantly in form and texture from components in carbonaceous meteorites and contain some mineral assemblages which do not occur in any meteorite class. These IDPs are nonequilibrium assemblages of (1) ultrafine (2–50 nm) Mg,Fe-olivines, Mg,Fe-pyroxenes, Fe,Ni-sulfides, Fe,Ni-oxides, and Fe,Ni-metals, (2) amorphous materials, and (3) carbonaceous and carbon materials. They may contain small but variable amounts of submicron (~100–1000 nm) minerals. For example, plagioclase-feldspars, K-feldspars, Mg,Fe-smectites, illite, kaolinite, barite, (Mg,Ca,Na)-hydrosulfates, calcite, and brucite in various aggregate IDPs. The CS IDPs contain calcite and various Mg,Fe-carbonates. The predominant Mg,Fe-olivines, Mg,Fe(low-Ca)-pyroxenes, and pyrrhotites show a wide range of grain sizes from 2 to 1000 nm that may correlate with different provenances. The carbonaceous materials also occur in many forms, viz. polycyclic aromatic hydrocarbons, amorphous, turbostratic, and poorly graphitized carbons (300–4000 nm in size), graphite, lonsdaleite, and Fe,Ni-carbides.

IDP Alteration

All particles experience a thermal spike (5–15 s) during deceleration in the atmosphere as a function of size, density, and entry velocity and entry angle, and whereby the entire particle is heated. The ensuing dynamic pyrometamorphic oxidation reactions include laihunitization of Mg,Fe-olivines, and oxidation of common Fe,Ni-sulfides. The resulting magnetite and maghemite often form a thin (<100-nm) rim on the particle.Temperatures in unmelted IDPs can be up to 1050 °C. Other alteration processes affecting the IDPs were recognized. Linear features in olivine and diopside single-crystals are solar flare tracks acquired during Solar System sojourn. Sputter rims on Mg-rich olivines testify that they traveled as small bodies in interstellar space.

The most significant postaccretion alteration of the IDPs is related to residency in a parent body with a heat source that could support the presence of an

aqueous fluid. An understanding of the complex mineralogies in chondritic IDPs dawned with the finding that amorphous materials are common in these particles. They are amorphous ferromagnesio-aluminosilica materials [Mg/(Mg+Fe) = 0.23–0.95 (wt.%)], and rare silica-rich and (almost) chondritic materials. Using examples of terrestrial alteration, it is plausible that dry crystallization of amorphous alkali-bearing aluminosilica materials leads to the formation of K-feldspar and plagioclase-feldspars; and aqueous alteration of amorphous materials, or preexisting tectosilicates, yields layer silicates. These secondary minerals, and others, support dry (thermal) and aqueous ($T < 200\,°C$) alteration when these IDPs were resident in icy protoplanets. The scarcity of energy for alteration is an ever present problem. This problem is alleviated by a thin layer of interfacial water that is present on grains in dirty ice. This hydrocryogenic alteration at $T < 0\,°C$ is quite efficient to allow growth layer silicates and salts in IDPs. The least altered chondritic aggregate particles consist of distinct (sub)spherical units, and some amorphous and ultrafine-grained anhydrous units remain in hydrated IDPs.

The Original Dusts

Chondritic aggregates are sediments of (sub)spherical units and rare micrometer-sized ("xenolithic") single-crystal silicates (e.g., enstatite whiskers) and Fe,Ni-sulfides. Local concentrations of carbonaceous (Fig. 8) and carbon-free units (Fig. 9) in almost unaltered IDPs fused into irregular contiguous patches.

The original units, or principal components, include three chemically distinct types (Table 1). The nomenclature is confusing, with different names for the same unit or a general term for different types. Table 1 offers a guide to assess the literature.

Each principal component is a unique chemical end member with a unique (minimum) unit size. Fusion into larger entities may not lead to new chemical types. A recent model for the formation of carbon-bearing chondritic IDPs considers the formation of aggregates that are mixtures of three principal components. The components are the dusts that accreted in the solar nebula. Among others, this model shows evolution of IDP morphology. A high ratio of carbon-free to carbon-bearing ferromagnesio-aluminosilica units in an aggregate particle might, upon hydration and loss of ice, yield a compact CS IDP with relic units. Variable carbon contents of chondritic IDPs reflect the extent of mixing of the carbonaceous component relative to other types during accretion.

Only if the distributions of principal components in the nebula are a function of heliocentric distance, will it be possible to use particle chemistry and morphology as a discriminant of its origin. Many primary and secondary features of chondritic particles remain intimately linked to the proportions of principal components acquired during accretion. These scenarios remain to be proven, but the resulting textures and minerals of carbon-bearing chondritic IDPs may contain information on the scale lengths of accretion in the solar nebula at

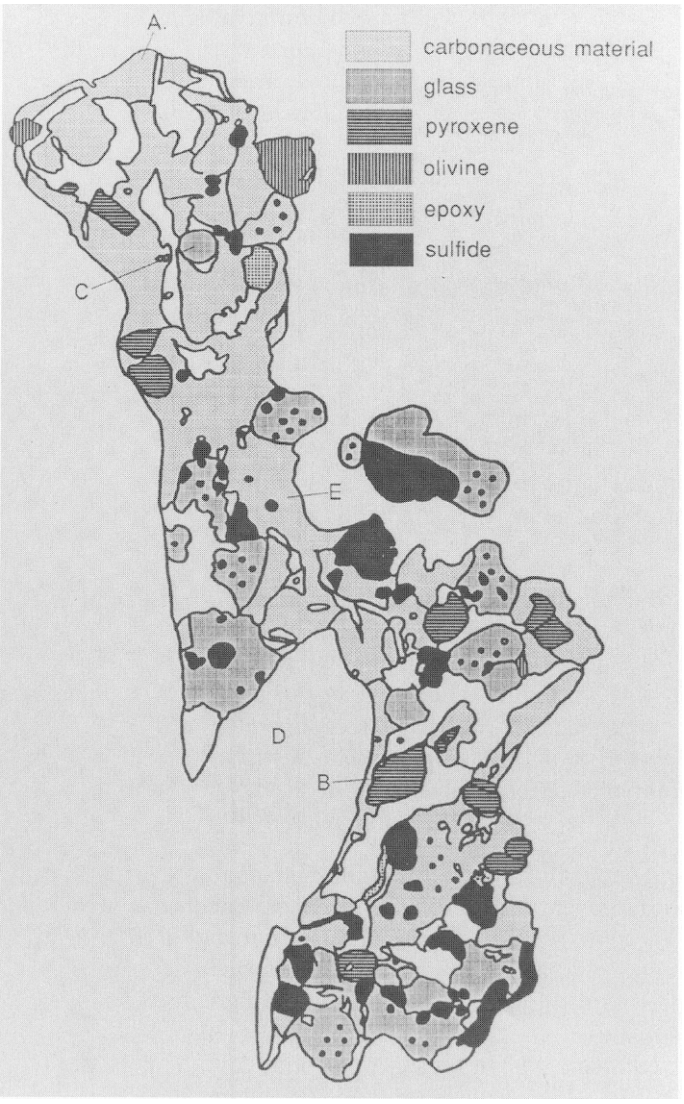

Fig. 8. Mineralogical map based on a transmission electron photomicrograph of an ultrathin section of carbon-rich chondritic IDP W7027H14 showing a contiguous area of carbonaceous material. *A* Carbonaceous material; *B* pyroxene; *C* glass; *D* epoxy, used for embedding of the sample for ultramicrotomy; *E* sulfide. Length of section 5 μm. (Thomas KL et al. 1993)

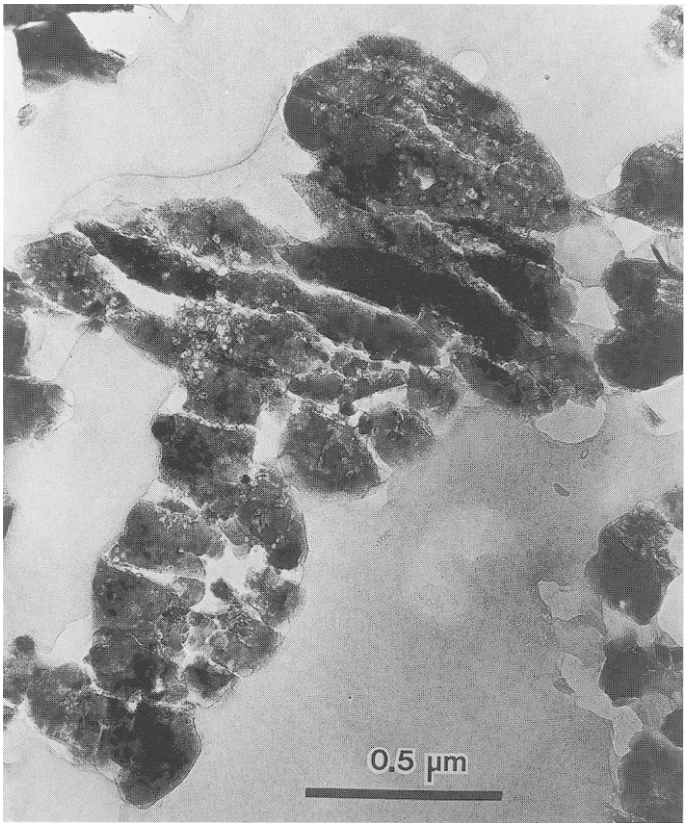

Fig. 9. Transmission electron micrograph of an ultrathin section of chondritic IDP L2011K7 embedded in epoxy (gray background) showing fusion of subspherical (carbon-free) ferromagnesio-aluminosilica (very low Al_2O_3) units with ultrafine-grained Mg, Fe-olivines and pyroxenes and iron oxides. The shattered appearance is an artifact of ultramicrotome sectioning

Table 1. Principal components of chondritic IDPs

Carbonaceous units: refractory hydrocarbons and amorphous carbons Unit size: ~400 nm in diameter
Carbon-bearing ferromagnesio-aluminosilica units Variable Mg/(Mg+Fe) ratios, alkali and Al_2O_3 contents. The units contain ultrafine (2–50 nm) platey Mg,Fe-olivines, Mg,Fe-pyroxenes, Fe,Ni-sulfides, Fe,Ni-metal and Fe,Ni-carbides in a matrix of refractory hydrocarbons and amorphous carbons. Unit size: 100 nm in diameter
(Carbon-free) ferromagnesio-aluminosilica units Variable Mg/(Mg + Fe) ratios, alkali, CaO and Al_2O_3 contents. The units can be amorphous, or holocrystalline (both coarse- and ultrafine-grained) with Mg,Fe-olivines, Mg,Fe-pyroxenes, and Fe,Ni-sulfides. The unit compositions match $(Mg,Fe)_3Si_2O_7$. Units may have an amorphous zone on the periphery. Unit size: 125–1000 nm in diameter (see text)

the sites of their sources. The model received a boost from the 1985/6 encounters with P/comet Halley that recorded an unexpected incidence of light-element, so-called CHON, particles. They could be similar to the carbonaceous units that have since been identified in carbon-rich chondritic IDPs.

Future Research

The minor and trace elements, D/H ratios, and hydrocarbons in carbon-bearing chondritic IDPs also yield new insights. Mineralogical studies of these fascinating dusts remain a prerequisite to constrain dynamic pyrometamorphism and parent body alteration of these IDPs. For example, are oxidation states of carbon, sulfur, an iron correlated, and does S^0 exist in these particles? What are the original (i.e., primary) properties of the principal components? For example, the unit size of the carbon-free component is not yet defined. Their exact bulk compositions also remain uncertain. What is their origin? If they are presolar (or interstellar) dust, the principal components were probably amorphous materials that altered after accretion. Amorphous carbon-free and carbonaceous units occur in several particles but, in others, an amorphous nature of carbon-free and carbon-bearing ferromagnesio-aluminosilica units is inferred from the size distributions of their constituent nanograins. When were the ultrafine silicates and Fe-Ni-sulfides formed? They could be presolar grains that acquired a carbon coating in the solar nebula. In this scenario, efficient evaporation and (re)condensation of (hydro)carbons occurred in the solar nebula at the locations of these IDP sources. This scenario is inconsistent with very high D/H ratios in some of these IDPs, which suggests that carbons were carried to the nebula. It is even possible that the ultrafine minerals are much younger than 4.56 Ga and formed during atmospheric entry. The model creates exciting research opportunities of the complex carbon-bearing chondritic IDPs. The results will constrain the histories of their sources and processes in the solar nebula such as component mixing as a function of heliocentric distance and/or turbulent transport during accretion. The causes of fusion, viz. chemical reactions and/or compaction, of principal components, and associated variations in intraparticle density and porosity), are important. The resulting microtextures, that could determine particle alteration, include partial melting on atmospheric entry.

Conclusions

The Holy Grail of this research would be to find a fluffy, carbon-bearing chondritic aggregate of the three amorphous principal components. It would firmly support the current model of principal component mixing and subsequent parent body alteration and dynamic pyrometamorphism. The carbon-bearing chondritic IDPs are dominated by amorphous materials and (ultra)fine-grained high-temperature minerals.

These properties contribute to a state of high free energy that wild determine particle alteration when energy to activate mineral reactions is scarce. The principal components of chondritic IDPs collected in the lower stratosphere contain a tremendous amount of information on the nature of dusts and processes in the solar nebula. They are a window to the earliest time of our solar system, and to ongoing processes in our galaxy.

References

Bradley JP, Sandford SA, Walker RM (1988) Interplanetary dust particles. In: Kerridge JF, Matthews MS (eds) Meteorites and the early solar system. University Arizona Press, Tucson, pp 861–898

Brownlee DE (1985) Cosmic dust: collection and research. Annu Rev Earth Planet Sci 13:147–173

Mackinnon IDR, Rietmeijer FJM (1987) Mineralogy of chondritic interplanetary dust particles. Rev Geopyhs 25:1527–1553

Rietmeijer FJM (1992) Mineralogy of primitive chondritic protoplanets in the early solar system. Trends Mineral 1:23–41

Sandford SA (1987) The collection and analysis of extraterrestrial dust particles. Fundam Cosmic Phys 12:1–73

Thomas KL et al. (1993) Carbon abundance and silicate mineralogy of anhydrous interplanetary dust particles. Geochim Cosmochim Acta 57:1551–1566

Zolensky ME, Wilson TL, Rietmeijer FJM, Flynn GJ (eds) (1994) Analysis of interplanetary dust. AIP Conf Proc 310, Am Inst Physics, New York, 357 pp

1.5 Cosmogenic Matter in Terrestrial Environments

G. KURAT

The accretionary influx of extraterrestrial matter onto the Earth amounts to about 40000 t/a and is delivered mainly by meteoroids in the size range 50–400 μm (median 220 μm – Love and Brownlee 1993). Not all particles of this size can survive atmospheric entry unaltered. Most are frictionally heated to such an extent that partial to total melting and also partial evaporation takes place (e.g., Kornblum 1969). However, small particles and some of the larger ones penetrating the atmosphere at low velocities and almost tangential entry angles can enter without being melted (Brownlee 1981; Bonny and Balageas 1988; Love and Brownlee 1991).

Melted interplanetary dust particles, cosmic spherules, are omnipresent in sediments throughout geological times (e.g., Taylor and Brownlee 1921). Unmelted interplanetary dust is certainly also present but not easily distinguished from terrestrial dust. It can, therefore, be collected only in places were there are low amounts of terrestrial dust.

Advanced Mineralogy, Volume 3
Mineral Matter in Space, Mantle, Ocean Floor, Biosphere,
Environmental Management, and Jewelry (ed. by A. S. Marfunin)

One such place is the stratosphere, where interplanetary dust can be collected utilizing high-flying aircraft or balloons (e.g., Brownlee 1985). However, only small dust particles (average diameter about 10 μm) can be collected in this way, but not the large ones, for several reasons (e.g., Warren and Zolensky 1994). Such particles (stratospheric interplanetary dust particles – SIDPs, unfortunately commonly called IDPs) have been available for study for more than 15 years. Since 1984 also large unmelted interplanetary dust particles – micrometeorites (MMs) – have been available from Greenland ice (Maurette et al. 1986) and subsequently also from Antarctica (Maurette et al. 1991).

In Greenland, micrometeorites can be retrieved from "cryoconite", a dark sediment in melt-water lakes, which consists of dust and cocoons of blue algae and siderobacteria. On average, cryoconite contains about 10 g/kg fine-grained sand and dust, mostly of terrestrial origin, and about 800 cosmic spherules and 200 unmelted to partially melted micrometeorites.

In Antarctica, micrometeorites can be harvested by artificially melting the proper ice. One ton of Antarctic blue ice contains about 100 cosmic spherules with diameters >50 μm and about 500 unmelted to partially melted MMs 50–400 μm in size. Now, fortunately, large amounts of unmelted and almost unaltered samples of the interplanetary dust particles which contribute most to the recent accretion rate on Earth are available for study.

The Nature of Interplanetary Dust

Many micrometeorites have suffered severe alteration by frictional heating in the atmosphere. They are partially to almost totally melted, consisting of foamy glass with variable amounts of unmelted phases. Others have been thermally altered (metamorphosed) but not melted and a few have grossly retained their pristine mineralogy. Some micrometeorites suffered additional alterations in the hostile terrestrial environment.

The pristine mineralogy of micrometeorites is surprisingly simple (e.g., Maurette et al. 1991, 1994; Kurat et al. 1993, 1994a; Klöck and Stadermann 1994). Major minerals are olivine, low-Ca pyroxene, magnetite, and hydrous Mg-Fe silicates (phyllosilicates) like serpentine and saponite. Individual MMs are usually dense, low-porosity mixtures of anhydrous and hydrous phases in proportions ranging from fully anhydrous (coarse-grained "crystalline" micrometeorites) to fully hydrous mineral assemblages (phyllosilicate micrometeorites).

Minor phases comprise Ca-rich pyroxenes, feldspars, Fe-Ni sulfides and metal, Mg-Fe hydroxides, Mg-Al and Fe-Cr spinels, perovskite, ilmenite, hibonite, and others.

The major silicates have highly variable Fe/Mg ratios, even within a given particle (unequilibrated mineral assemblage) and are usually very rich in minor elements as compared to their terrestrial counterparts (Fig. 10).

The hydrous minerals contain some elements in chondritic abundances (e.g., Ti, Al, Cr, Na, K).

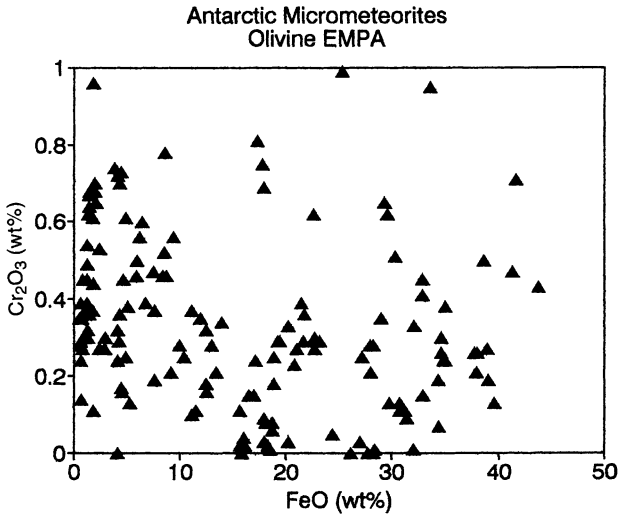

Fig. 10. Plot of Cr_2O_3 vs. FeO contents (wt.%) of olivines from micrometeorites which have varying FeO contents and commonly high Cr_2O_3 contents (terrestrial olivines usually do not contain Cr). Olivines with <0.5 wt% FeO, which are common in CM and CR chondrites, are very rare in MMs

Refractory minerals like Mg-Al spinel are strongly enriched in refractory trace elements (e.g., rare earth elements, Sc, Zr, Hf, etc. – Kurat et al. 1994b) as compared to chondritic rocks.

The mineralogy, mineral chemistry, and the presence of refractory minerals in MMs are similar to those of CM-type (Mighei-type) an CR-type (Renazzo-type) carbonaceous chondrites. However, there are some differences between MMs and CM/CR chondrites, like the presence of abundant Ca-poor pyroxene in MMs (most CM chondrites do not contain such pyroxenes), the lack of very Fe-poor olivines with high Al and Ca contents in MMs (they are common in CM and CR chondrites), and the high abundance of Fe-rich olivines and pyroxenes in MMs.

Bulk major and minor element abundances in phyllosilicate-rich MMs are chondritic, except for Ca, Na, Ni, and S, which are depleted with respect to CI (and CM/CR) chondrites (Fig. 11). Coarse-grained crystalline, anhydrous MMs deviate from the chondritic composition, a feature typical also for anhydrous aggregates and chondrules in carbonaceous chondrites.

Lithophile trace element abundances in phyllosilicate-rich MMs (Fig. 12) follow the abundance pattern of CM chondrites (which is also similar to that of CR chondrites) and deviate from that only in the abundance of K. However, the abundances of siderophile elements in MMs, deviate significantly from those of CI and CM/CR chondrites.

Only the highly refractory elements Os and Ir and the highly volatile Se have abundances similar to those in CI and CM/CR chondrites. The common

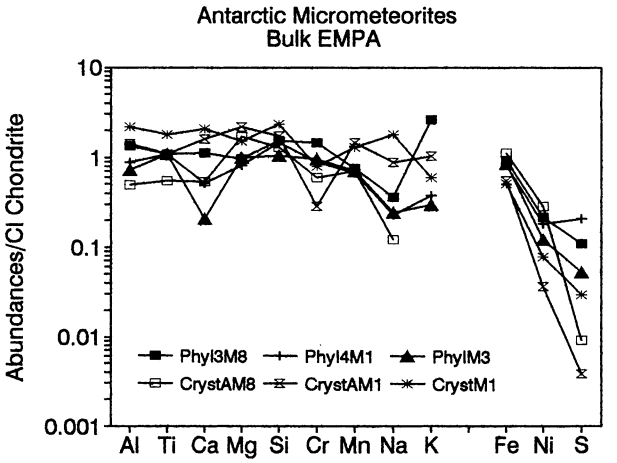

Fig. 11. Chondrite-normalized major and minor element abundances in phyllosilicate-rich and anhydrous crystalline micrometeorites (electron microprobe data from Kurat et al. 1994). Lithophile (*left*) and siderophile (*right*) elements are arranged in order of increasing volatility

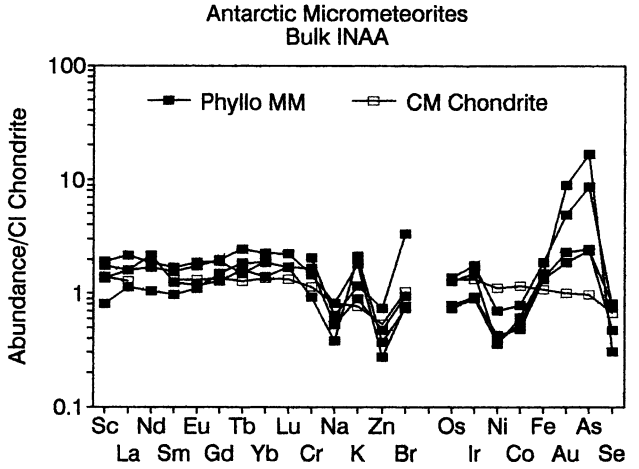

Fig. 12. Chondrite-mormalized abundances of selected trace elements in phyllocilicate-rich micrometeorites (INAA data from Kurat et al. 1994). Lithophile (*left*) and siderophile (*right*) elements are arranged in order of increasing volatility

siderophile elements Ni and Co are depleted compared to chondritic abundances and also fractionated from each other (the Ni/Co ratio is nonchondritic). Iron is enriched over chondritic abundances (moderately), as are Au and As (strongly). The depletion in Ni, Co, and S has been shown (Presper et al. 1993) to be due to terrestrial leaching of Ni-bearing Mg-Fe sulfates from MMs.

Micrometeorites do not contain sulfates which, on the other hand, are abundant in CM and CI chondrites. Large voids present in some MMs may have

been occupied by a soluble mineral. Similarly, the depletion of MMs in Ca, as compared to CM chondrites, is possibly due to leaching of carbonates, minerals which are common in CM chondrites but absent from MMs. The enrichments of MMs in Au, As, and K over chondritic abundances must be due to terrestrial contamination. All three elements are strongly enriched in the terrestrial crust as compared to chondrites.

A special compositional feature of MMs (and also SIDPs) is their richness in carbon. Perreau et al. (1993) and Engrand et al. (1994) showed that MMs have C/O ratios which are on average higher than those of CI chondrites, the most C-rich chondrites.. MMs are up to 5x richer in C than CM/CR chondrites.

The small particle portion of the interplanetary dust, the stratospheric interplanetary dust particles – SIDPs, with a typical diameter of about 10 μm, has in principle mineralogical and chemical compositions which are similar to those of micrometeorites. Thus, they consist of either phyllosilicates, anhydrous silicates (olivine or pyroxene), or mixtures thereof (e.g., Brownlee 1985; Bradley 1988; Klöck and Stadermann 1994; Zolensky and Barrett 1994). Also, the chemistry of the major phases is very similar to that of MM phases, i.e., olivine and pyroxene have varying Fe/Mg ratios, and high contents of minor elements and phyllosilicates are mostly saponite with minor serpentine, both rich in minor elements. Magnetite, Ca-rich pyroxene, sulfides, and accessory refractory phases are also present. However, in addition to what has been found in MMs, SIDPs contain sulfates and carbonates of a composition similar to those of carbonaceous chondrites.

Furthermore, there is a class of particles present among SIDPs which has not yet been found among micrometeorites or in meteorites: highly porous aggregates of sub-μm-sized Mg, Fe silicates, Ni, Fe sulfides, and Ni, Fe metal in a glassy and/or carbonaceous matrix (e.g., Bradley 1988; Bradley et al. 1992; Thomas et al. 1994; Rietmeijer 1994).

These aggregates commonly are extremely fluffy and have very high C contents (up to 13×CI, e.g., Thomas et al. 1994).

The chemical bulk composition of SIDPs is chondritic for major, minor, and trace elements (e.g., Jessberger et al. 1992). However, abundances of some elements are nonchondritic due to primary differences (surplus of C) or terrestrial contamination (surplus of K, As, Sb, and Br).

The isotopic composition of several elements has been found to be nonterrestrial and, in some cases, also nonsolar, in both MMs and SIDPs (e.g., McKeegan 1987; Stadermann 1991; Hoppe et al. 1995; Engrand et al. 1996). Specifically, anomalies in isotopic abundances of H/D, C, N, and O have been found.

Interplanetary dust has been exposed to the solar wind and cosmic rays for a sufficiently long time to accumulate large amounts of noble gases and spallogenic isotopes. They have, for example, very high He (up to 10^{-1} cm^3g^{-1} at STP) and Ne contents – in excess of 10^{-5} cm^3g^{-1} at STP – comparable to only a few very gas-rich chondrites and the lunar soil (e.g., Maurette et al. 1991; Nier 1994).

Helium and neon isotope abundances confirm the extraterrestrial origin of SIDPs and MMs (and some cosmic spherules) as they are comparable to those of solar energetic particles (SEP). In addition, a small contribution from cosmic ray spallation neon was also identified.

Thus, SIDPs and MMs were exposed to cosmic rays and to the solar wind. For the solar wind exposure, the particles must have been of the size recovered. Thus, MMs and SIDPs (e.g., Nier and Schlutter 1990) are true interplanetary dust meteoroids and cannot be products of the breakup of a larger meteoroid in the atmosphere.

Conclusions

Interplanetary dust accreting onto the Earth today bears some similarities to the rare CM/CR carbonaceous chondrites, but differs form them in so many ways that it must be considered a Solar System matter of its own. The features making it different from chondrites are likely to be of primordial origin. These include the mineral abundances, mineral chemistry, the bulk C content, and the presence of unique, fluffy, fine-grained aggregates.

Some deviations in the dust composition from that of chondrites are due to extraction of water-soluble sulfates and carbonates and contamination from the terrestrial environment.

We have good reasons to favor comets as the source of most of the interplanetary dust in the solar system. Therefore, interplanetary dust allows us to study the primordial matter which probably supplied the Earth with volatile elements and the oceans and, possibly, with the ingredients for the development of life.

References

Bonny P, Balageas D (1988) Entry corridor of micrometeorites containing organic material. Lunar Planet Sci Conf XXI:111–112

Bradley JP (1988) Analysis of chondritic interplanetary dust thin-sections Geochim Cosmochim Acta 52:889–900

Bradley JP, Humecki HJ, Germani MS (1992) Combined infrared and analytical microscope studies of interplanetary dust particles. Astrophys J 394:643

Brownlee DE (1981) Extraterrestrial component in deep sea sediments. In: Emiliani C (ed) The sea. vol 7. Wiley & Sons, New York, pp 773–762

Brownlee DE (1985) Cosmic dust: collection and research. Annu Rev Earth Planet Sci 13:147–173

Engrand C, Christophe Michel-Levy M, Jouret J, Kurat G, Maurette M, Perreau M (1994) Are the most C-rich Antarctic micrometeorites exotic? Meteoritics 29:464

Engrand C, Deloule E, Hoppe P, Kurat G, Maurette M, Robert F (1996) Water contents of micrometeorites from Antarctica. Lunar Planet Sci Conf XXVII:337–338

Hoppe P, Kurat G, Walter J, Maurette M (1995) Trace elements and oxygen isotopes in a CAI-bearing micrometeorite from Antarctica. Lunar Planet Sci Conf XXVI:623–624

Jessberger EK, Bohsung J, Chakaveh S, Traxel K (1992) The volatile element enrichment of chondritic interplanetary dust particles. Earth Planet Sci Lett 112:91–99

Klöck W, Stadermann FJ (1994) Mineralogical and chemical relationship of interplanetary dust particles, micrometeorites and meteorites. In: Zolensky ME, Wilson TL, Rietmeijer FJM, Flynn GJ (eds) Analysis of interplanetary Dust. Am Inst Physics, New York, pp 51–88

Kornblum JJ (1969) Micrometeoroid interaction with the atmosphere. J Geophys Res 74:1893–1906
Kurat G, Brandstätter F, Presper T, Koeberl C, Maurette M (1993) Micrometeorites. Russ Geol Geophys 34:132–147
Kurat G, Koeberl C, Presper T, Brandstätter F, Maurette M (1994a) Petrology and geochemistry of Antarctic micrometeorites. Geochim Cosmochim Acta 58:3879–3904
Kurat G, Hoppe P, Maurette M (1994b) Preliminary report on spinel-rich CAIs in an Antarctic micrometeorite. Lunar Planet Sci Conf XXV:763–764
Love SG, Brownlee DE (1991) Heating and thermal transformation of micrometeorites entering the Earth's atmosphere. Icarus 89:26–43
Love SG, Brownlee DE (1993) A direct measurement of the terrestrial mass accretion rate of cosmic dust. Science 262:550–553
Maurette M, Hammer C, Brownlee DE, Reeh N, Thomsen HH (1986) Placers of cosmic dust in the blue ice lakes of Greenland. Science 233:869–872
Maurette M, Immel G, Hammer C, Harvey R, Kurat G, Taylor S (1994) Collection and curation of IDPs from the Greenland and Antarctic ice sheets. In: Zolensky ME, Wilson TL, Rietmeijer FJM,, Flynn GJ (eds) Analysis of interplanetary dust. Am Inst Physics, New York, pp 277–289
Maurette M, Olinger C, Christophe Michel-Levy M, Kurat G, Pourchet M, Brandstätter F, Bourot-Denise M (1991) A collection of diverse micrometeorites recovered from 100 tonnes of Antarctic blue ice. Nature 351:44–47
McKeegan KD (1987) Ion microprobe measurements of H, C, O, and Si isotopic abundances in individual interplanetary dust particles. PhD Thesis, Washington Univ, St Louis, Missouri, pp 187
Nier AO (1994) Helium and neon in interplanetary dust particles. In: Zolensky ME, Wilson TL, Rietmeijer FJM, Flynn GJ (eds) Analysis of interplanetary Dust. Am Inst Physics, New York, pp 115–126
Nier AO, Schlutter DJ (1990) He and Ne isotopes in individual stratospheric particles – a further study. Lunar Planet Sci Conf XXI:883–884
Perreau M, Engrand C, Maurette M, Kurat G, Presper T (1993) C/O atomic ratios in micrometer-sized crushed grains from Antarctic micrometeorites and two carbonaceous meteorites. Lunar Planet Sci Conf XXIV:1125–1126
Presper T, Kurat G, Koeberl C, Palme H, Maurette M (1993) Elemental depletions in Antarctic micrometeorites and Arctic cosmic spherules: comparison and relationships. Lunar Planet Sci Conf XXIV:1177–1178
Rietmeijer FJM (1994) A proposal for a petrological classification scheme of carbonaceous chondritic micrometeorites. In: Zolensky ME, Wilson TL, Rietmeijer FJM, Flynn GJ (eds) Analysis of interplanetary dust. Am Inst Physics, New York, pp 231–240
Stadermann FJ (1991) Messung von Isotopen- und Elementhäufigkeiten in einzelnen interplanetaren Staubteilchen mittels Sekundärionen-Massenspektroskopie. PhD Thesis, University of Heidelberg, Germany, pp 97
Taylor S, Brownlee DE (1991) Cosmic spherules in the geologic record. Meteoritics 26: 203–211
Thomas KL, Keller LP, Blanford GE, McKay DS (1994) Quantitative analysis of carbon in anhydrous and hydrated interplanetary dust particles. In: Zolensky ME, Wilson TL, Rietmeijer FJM, Flynn GJ (eds) Analysis of interplanetary dust. Am Inst Physics, New York, pp 165–172
Warren JL, Zolensky ME (1994) Collection and curation of interplanetary dust particles recovered from the stratosphere by NASA. In: Zolensky ME, Wilson TL, Rietmeijer FJM, Flynn GJ (eds) Analysis of interplanetary dust. Am Inst Physics, New York, pp 245–254
Zolensky ME, Barrett R (1994) Olivine and pyroxene compositions of chondritic interplanetary dust particles. In: Zolensky ME, Wilson TL, Rietmeijer FJM, Flynn GJ (eds) Analysis of interplanetary dust. Am Inst Physics, New York, pp 105–114

1.6 Giant Planets

A.V. KOZENKO, V.N. ZHARKOV

Giant planets (GP), brown dwarfs (BD) and very low mass stars (VLM) are objects which have a number of characteristics in common due to the properties of their equations of state. Their luminosities are very low (much less than the solar luminosity, Lo) and their evolutionary time scales are typically measured in Ga.

VLM stars are objects which are more massive than $\sim 10^{-1}$ M⊙ (solar mass).

The term BD has become standard usage for designating a new class of object with the following characteristics: (1) composition similar to the Sun (dominated by hydrogen); (2) masses lie roughly in the range 10^{-2} M⊙ ≤ M ≤ 10^{-1} M⊙ (i.e., masses about ten times larger than that of Jupiter, but smaller than the critical mass for sustained thermonuclear fusion of hydrogen).

GP are the four largest planets of the Solar System: Jupiter, Saturn, Uranus, and Neptune. Their masses lie in the range 5×10^{-5} M⊙ ≤ M ≤ 1×10^{-3} M⊙. The lower mass limit is set by the object's ability to retain hydrogen during accumulation. There is some uncertainty about possible models of origin of objects in the mass range 10^{-3} M⊙ ≤ M ≤ 10^{-2} M⊙ because the minimum mass for direct formation of a BD from collapse of an interstellar cloud of H and He is ~ 0.02 M⊙. The group of terrestrial planets have no ability to retain hydrogen, due to their being small too masses.

We cannot directly sample the interiors of GP. However, we can use the observational data, experimental data (i.e., equations of state), and physical laws to construct computer models of the interiors.

GPs are gas-liquid, convective, adibatic planets due to:

1. If a GP formed as a hot body, it would not have been able to cool off during its existing time, $t_p \sim 4.5 \times 10^9$ years, because its cooling length $I_{cool} \sim (Xt_p)^{1/2}$ is in the order of 5×10^2 km ($X \sim 10^{-2}-10^{-3}$ cm^2/s is the thermal diffusivity of molecular hydrogen).
2. The heat flow from the planet's interior is calculated as $\sim 10^4$ erg/cm^2/s, that is about 4 orders of magnitude greater than the maximum heat flux that can be transported by molecular conduction.
3. All GPs have instrinsic magnetic fields.
4. It proved that values of the specific dissipative function Q for Jupiter, Saturn, and Uranus are 2.5×10^4, 1.4×10^4, and 5×10^3, respectively and are all about 2 orders of magnitude greater than typical values for matter in the solid state.
5. The planetary gravitational field for GPs corresponds to the field of a planet in hydrostatic equilibrium.

Observational Data

The observational data on cosmochemical abundance and oxygen-carbon ratio give new insight into the internal structure of the GPs. The materials of which the planets consist, are divided into three components according to their volatility: (1) gases (He_2, He, Ne, etc) – the G-component; (2) ices (CH_4, NH_3, N_2O) – the I-component; and (3) rocks and iron-nickel – the R-component.

Depending on (P, T) conditions in the protoplanetary cloud, some compounds of I-component (CH_4 and NH_3) may be present in the G-component. It is assumed that: (1) in the zone of GPs the protosolar cloud contained carbon and nitrogen existing in the forms CH_4 and NH_3, because the pressure in the gaseous phase was significantly larger. Modeling calculations show that the formation of Uranus and Neptune was not accompanied by the formation of gaseous envelopes around them, as in the case of Jupiter and Saturn. Carbon exerts the most noticeable influence on G- and I-components. If it formed CO and was in a gaseous phase, then the mass fraction of the I-component in solid phase (which consists of I and R) and the I/R ratio were strongly decreased.

The Theoretical Background: Equations of State

The equation of state of hydrogen is particularly relevant to the largest two giant planets: Jupiter and Saturn.

Under the circumstances in GP, the relation between pressure, P, and mass density, p, is largely independent of temperature, T, and can be expressed in the form $P \sim p^{\alpha}$ with $1.6 < \alpha < 2$. This result is universally true for hydrogen-rich objects in the relevant mass range where the equation of state is mainly governed by the physics of metallic hydrogen (liquid phase) – BD equation of state.

The equation of state for Jupiter follows the BD equation of state most closely, deviating toward a higher-density profile only in a small innermost ice or rock-ice core. By ice, we mean a material composed of the molecules H_2O, CH_3, and NH_3 in solar proportions, not necessarily with intact molecules, and not necessarily in the solid phase.

In Saturn, the deviation from the BD equation of state begins in the metallic-hydrogen region. The hydrogen-helium pressure-density relation can be calculated using purely theoretical results at high pressure and experimental data for effective pair potential at low pressure. The enhanced density of Saturn in the region is interpreted as being caused by enrichment of helium due to immiscibility in metallic hydrogen, and possible enrichment of the ice component.

Uranus and Neptune are composed primarily of ice, a substance which is accessible to laboratory shock compression experiments in the relevant pressure range (typical central pressure reach only a few Mbar). Satisfactory models for both planets have outer hydrogen-helium envelopes which extend to

a maximum pressure of $\sim 0.1-0.2$ Mbar, below which point the equation of state very closely follows the P(p) curve for ice ($0.1 < P < 8$ Mbar). A rocky core may exist in either Uranus or Neptune.

Models of Giant Planets

Methods for generating the models of GP were developed in early 1970s.

In developing the new models, the abundances of elements were used. Three variants of I + R components were used:

IR1 = (CH_4, NH_3, H_2O + rocks), I/R = 3.1
IR2 = (NH_3, H_2O + rocks), I/R = 2.2,

considering that CH_4 exists in a gaseous phase.

IR3 = (H_2O + rocks), I/R = 1.0,

CH_4 and NH_3 in gaseous phase.

New models of Jupiter and Saturn consist of five layers: the two-layered molecular envelope, an atomic metallic envelope, and a two-layer core. The models with homogeneous helium concentration in the hydrogen envelope or Jupiter ($Y_1 = Y_2 = Y_3$) are models of the first type and do not satisfy the condition of conservation of solar abundance of helium in the planet. In the models of the second type. $Y_2 = Y_3 > Y_1$. The models of Saturn are constructed as those for Jupiter.

The Jupiter-like two-layered molecular envelopes models of Uranus and Neptune are shown in Fig. 13.

The Evolution of Giant Planets

The present general hypothesis is that the embryos of the GPs first formed by accumulation planetesimals. These embryos later gravitationally accreted their gaseous envelopes from the solar nebula. The primary cores are formed by accumulation of rocky and ice planetesimals. If the core mass has reached some critical value, it is capable of concentrating and capturing a gaseous envelope.

The heat flow which corresponds to the observed luminosity, L, of GPs is presumed to be derived from two sources: (1) heat release from the object due to work done on the object's interior, and (2) due to changes in internal energy, E. In GPs the abundance of radioactive high-Z elements such as ^{40}K, ^{232}Th, and ^{238}U is too low for radioactive decay to be significant. The evolutionary age of the planet t_E is defined by the value of t, for which the planets luminosity drops to the present intrinsic luminosities. For the Jupiter, the theory gives $t_E = 5$ Ga, but for Saturn $T_E = 2.5$ Ga. Thus, Jupiter's heat flow is in accordance with the equation of state of hydrogen, but Saturn's is not. In the case of Saturn, it is

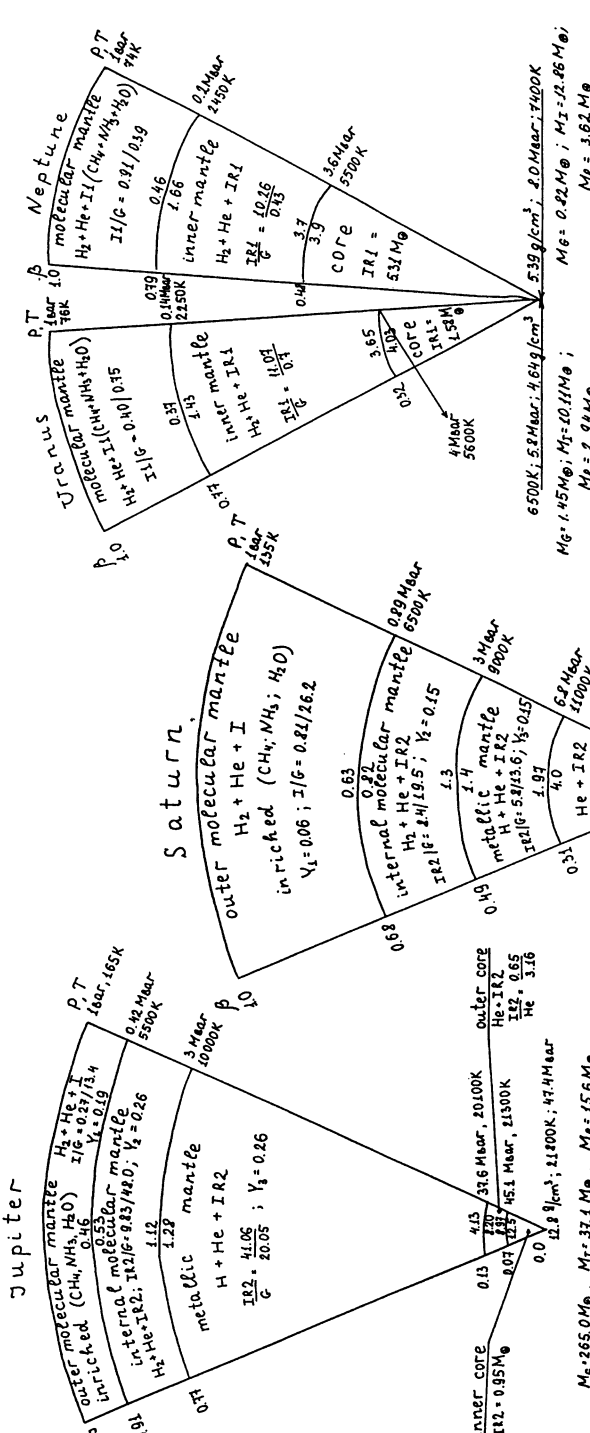

Fig. 13. Schemes of Jupiter, Saturn, Uranus, and Neptune models. Values of the pressure P and temperature T are shown at the interface $\beta(\beta = r/R -$ dimensionless radius) and at the *center.* At the *same levels* in the center of the scheme, the density p (g/cm^3) is shown. The I(IR)/G ratio and helium content in the envelopes are shown. The numerical values of the G, I, and R components are expressed in Earth masses ($M_\oplus$). The total values of the masses of the G, I, and R components in Earth masses and total value of helium content (Y_0) are given

necessary to account for the immiscibility of helium in liquid metallic hydrogen and the consequent formation of a helium-enriched core. Due to these processes, the additional gravitational energy is liberated in Saturn's interior. In the case of Uranus and Neptune, the equation of state is dominated by materials heavier than hydrogen and helium. Gravitational energy may be released by a rearrangement of the interior mass distribution in a planet: (1) helium with respect to hydrogen in hydrogen-rich planets (Jupiter and Saturn); (2) I-component with respect to G-component in planets which are rich in both (Uranus and Neptune).

References

Chabrier G, Shatzman E (eds) (1993) The equation of state in astrophysics. Cambridge University Press, Cambridge
Gehrels T, Matthews MS (eds) (1984) Saturn. University of Arizona Press, Tempe
Gudkova TV, Zharkov VN, Leontev VV (1988a) Models of Jupiter and Saturn having a two-layer molecular envelope. Sol Syst Res 22:159
Gudkova TV, Zharkov VN, Leontev VV (1988b) Models of Uranus and Neptune with partially mixed envelopes. Sol Syst Res 22:16
Hubbard WB (1994) Giant planets brown dwarfs, and low-mass star interiors. In: Chabrier G, Shatzman E (eds) The equation of state in astrophysics. Cambridge University Press, Cambridge, pp 443–462
Kafatos MC, Harrington RS, Maran SP (eds) (1986) Astrophysics of brown dwarfs. Cambridge University Press, Cambridge
Weaver HH, Danly L (eds) (1989) The formation and evolution of planetary systems. Cambridge University Press, Cambridge
Zharkov VN (1986) Interior structure of the Earth and planets. Harwood Academic Publ, Chur
Zharkov VN, Kozenko AV (1990) On the role of Jupiter in the formation of giant planets. Sov Astron Lett 16:169

1.7 Constitution of the Terrestrial Planets and the Moon

O. L. Kuskov

The mean densities of the terrestrial planets and the Moon differ. The observed mean density of Mercury is 5.44 g cm^{-3}. The Moon's mean density (3.344 g cm^{-3}) is much lower than that of the Earth (5.52 g cm^{-3}) or the other terrestrial planets (3.934 g cm^{-3} for Mars and 5.245 g cm^{-3} for Venus), probably because of a low metallic iron content. It is quite possible that the differences in mean density and chemical composition between the terrestrial planets and the Moon are explainable by physicochemical mechanisms of Fe/Si and Fe/FeO fractionation.

Moon

Six Apollo missions and three Luna missions provide the background of our knowledge of the Moon. The Moon is depleted in the most volatile elements and iron, and is enriched in refractory elements such as Al, Ca, Ti, and U. However, there is a broad spectrum of the proposed compositional models: from models enriched in Ca and Al to Earth-like compositions in which Ca and Al content is lower; values for the lunar FeO content range between 6 and 18%. The Moon is the only extraterrestrial body for which we have information about seismic velocities as a function of depth. From the point of view of comparative planetology, a major problem to be solved is the determination of the bulk chemical composition of the silicate Moon and the radius of the core.

The mineral composition and seismic structure of the Moon depend strongly on its bulk composition and thermal regime, whereas the bulk chemical composition is controlled by the origin of a planetary body. Although we are not certain what proportions of the major petrogenic oxides were incorporated into the growing Moon, it is almost certain from the seismic observations that their concentrations are different at different depths. The problem arises of how to determine the composition of the lunar mantle depending on the depth. The solution to this problem consists in translating the seismic velocity model into petrological models and vice versa, and comparing the calculated and observed geophysical data, including the mantle seismic velocities, the moment of inertia, and the mass of the Moon. In addition, limits to the composition of the crust, crustal thickness, and mean density, as well as composition and equation of state of the core, must be taken into account.

Geophysical Constraints

Geophysical constraints on the models of the lunar interior are being derived form topographic, gravitational, librational, thermophysical, and seismic data.

Moment of Inertia, Density, and Radius. A value of 0.3905 ± 0.0023 for the normalized moment of inertia of the Moon, as well as a value for the mean density of 3.3437 ± 0.003, are determined. Distribution of pressure can be described by an approximate formula: $P = P_0 [1-((R-H)/R)^2]$, where the pressure in the center of the Moon is $P_0 = 47.1$ kbar, $R = 1738$ km is the radius of the Moon, and H is the depth.

Crust. The mean crustal thickness under different physiographic region are: mascons, 30–35 km; irregular maria, 50–60 km; and highlands, 90–110 km. It is suggested that crustal mean density and thickness change in the range $2.90-3.05$ g/cm^3 and 58 ± 8 km.

Mantle. The most recent seismic velocity model based on the complete 5 year data set acquired when four Apollo seismometers were simultaneously opera-

tive, consists of three constant-velocity zones with very sharp discontinuous boundaries at depths of 270 and 500 km. The jump in the seismic parameter across the lunar 500-km discontinuity is equal to 20%, which is three to five times greater than that across the 400 or 650 km discontinuity in the Earth's mantle. The jump of velocities and seismic parameter across the lunar 270-km discontinuity is sharp and negative. There is no identical peculiarity for the Earth's mantle. According to this model, the lunar mantle is strongly differentiated and consists of the upper mantle (58–270 km), the middle mantle (270–500 km), and the lower mantle (between 500 km – and a core). Perhaps the most interesting seismic discovery has been the recognition of a widespread low-velocity zone at a depth of 270–500 km (Fig. 14).

Approach and Calculation of Bulk Composition, Mineralogy, and Physical Properties. On the basis of the geophysical constraints, chemical composition of the zoned Moon has been calculated by a method of thermodynamic modeling of phase relations and physical properties in the CaO-FeO-MgO-Al_2O_3-SiO_2 (CFMAS) system including solid solutions. The method involves computation of seismically admissible bulk compositions of the zoned Moon from the given seismic data (inverse problem). The oxide contents and temperature thus determined are adopted as starting approximation, and have been used further in calculations of velocity and density profiles according to the direct procedure.

P- and S-wave velocities have been found from:

$$V_P^2 = \{(K_s + 4/3G)/\rho\}, V_s^2 = \{G/\rho\},$$

where ρ, K_s and G are the density, adiabatic bulk modulus, and shear modulus.

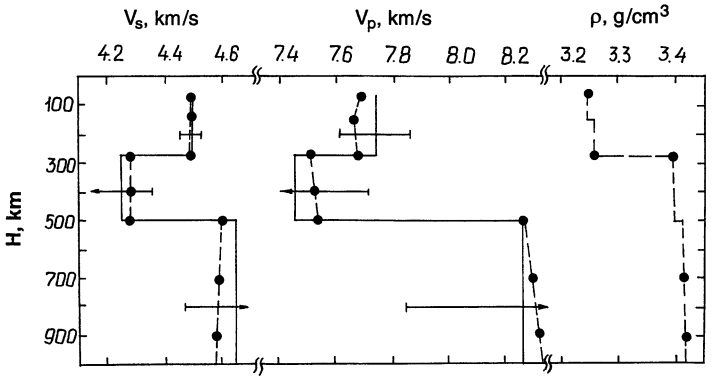

Fig. 14. Calculated velocity and density profiles in the lunar mantle (*dashed lines*) satisfying the moment of inertia and mean density of the Moon in comparison with the observed velocity data (*solid lines*, *error bars* denote seismic uncertainty). Bulk composition models for the upper, middle, and lower mantle are listed in Table 2

Composition of the Moon

The upper mantle of the Moon is enriched in SiO_2 and depleted in FeO relative to the middle mantle, whereas the middle mantle is enriched in SiO_2 and FeO in comparison with the lower mantle; the bulk Moon is enriched in refractories (Table 2). Compositions enriched in refractory elements provide the Al-Ca-rich highland crust.

Comparison of the most probable seismic profiles with those from thermodynamic modeling shows their practical compatibility, whereas the calculated mantle densities satisfy the moment of inertia as well as the mean density constraints (Fig. 14). These results show that there is no reason for density inversion in the Moon. Phase changes from the plagioclase-pyroxenite to the quartz-pyroxenite field taking place at depths of 130–150 km are not able to explain the nature of the 270-km discontinuity, whereas phase changes in any bulk composition model are not able to explain the nature of the 500-km discontinuity. These results lead to the conclusion that the lunar mantle is chemically stratified. At the same time, each separate zone of the mantle is chemically uniform and may be composed of: quartz-bearing pyroxenite containing 0.5–3 mol.% of free silica at depths of 58–270 km (upper mantle); olivine-bearing pyroxenite enriched in FeO at depths of 270–500 km (middle mantle) and olivine-orthopyroxene-clinopyroxene-garnet assemblage enriched in refractory (Al, Ca) elements at depths greater than 500 km (Table 2 and 3).

The preferred solutions for the chemical composition of the middle mantle (an olivine pyroxenite) have an FeO content between 14–18 wt.% (Mg 74–76), indicating that the middle mantle is more iron-rich than the upper and lower mantle. Such an enrichment in FeO may be responsible for the nature of the low-velocity zone at depths of 270–500 km with a density jump from 3.26 to 3.40 g cm^{-3} (Fig. 14). Another explanation is also possible: seismic data give evidence for the occurrence of hydrosilicates in the lunar middle mantle; the mineral assemblage consisting of pyroxene + olivine + garnet + talc and containing hydrosilicate phase (1.5 wt.% H_2O) might be responsible for the low-velocity zone.

The derived composition of the middle mantle is close to that for the source region of Apollo 11 and 12 basalts. Chemical analyses of Apollo 15

Table 2. Chemical composition of the silicate portion of the Moon (wt.%)

Oxide	Crust	Mantle			Entire Mantle	Crust + Mantle
		Upper	Middle	Lower		
SiO_2	45.5	56	52.2	44	50.3	49.9
MgO	7	30.5	24.5	32	29.4	27.5
FeO	6.5	8	17.5	9.5	11.2	10.8
Al_2O_3	25	3	3	8.5	5.2	6.9
CaO	16	2.5	2.5	6	3.9	4.9

Table 3. Phase composition of the lunar mantle (mol.%)[a]

Phase	Upper		Middle		Lower
	58 km	270 km	270 km	500 km	500–1258 km
Anorthite	2.1	0			
Quartz	0	2			
Orthopyroxene	92.8	91.8	94.4	96.8	
Clinopyroxene	5.1	6.2	2.5	0	35.5
Olivine			2.5	2.5	51.5
Garnet			0.6	0.7	13

[a] Solid solutions in the CFMAS system: olivine (binary); garnet (ternary: pyrope, almandine, grossulare); clinopyroxene (five-component solution: diopside, hedenbergite, clinoenstatite, clinoferrosilite, clinocorundum); orthopyroxene (five-component solution: orthodiopside, orthohedenbergite, enstatite, ferrosilite, orthocorundum).
Temperature distribution in the mantle: 58 km 420 °C; 270 km 800 °C; 500 km 1000 °C; 1258 km 1350 °C.

mare basalt samples fall into two distinctive groups, olivine basalts and quartz basalts; it has been suggested that olivine basalts result from magma extraction at depths of 300–400 km, whereas quartz basalts could result from magma segregation at depths of about 200 km. These petrological high-pressure experiments and petrochemical observations are in excellent agreement with the determination of chemical and mineral compositions of the upper and middle mantle from geophysical data.

The Al-Ca-rich model composition (6–9% Al_2O_3, 5–7% CaO) gives the best fit to the lower mantle seismic properties (Fig. 14, Table 3). The lower mantle may be composed of undifferentiated material of bulk lunar composition. In this case, the bulk composition of the crust + upper mantle + middle mantle must correspond to that of the lower mantle.

Core. The radius of the core depends on its composition, thickness of the crust, and distribution of density in the crust and mantle. The seismic constraints, combined with mass and moment of inertia calculations, suggest the presence of a core: 310 km in radius for the γ-Fe(Ni)-core and 480 km for the FeS-core. The existence of a lunar core is consistent with geophysical data (attenuation of seismic velocities, moment of inertia, electrical conductivity, lunar paleomagnetism).

The bulk composition and mineralogies of the silicate portion of the Moon (mantle + crust) generated by the geophysical data show that (Tables 2):

1. The concentrations of FeO, SiO_2, and refractory elements (Ca, Al) are significantly higher than those in the Earth's upper mantle; the bulk Moon is enriched in refractories by a factor of 1.5–2.5 compared with the terrestrial mantle and CI meteorites.
2. The lunar bulk Mg/Si (0.82) and Mg/Al (5.05) atomic ratios are much smaller than those of the Earth and chondrites.

3. The Fe/Si atomic ratio is equal to 0.18 for the silicate portion of the Moon and 0.22 for the Moon as a whole (crust+mantle+core); the latter value is close to the Fe/Si ratio of 0.28 form comet Halley data.
4. The lunar Mg# (Mg/Mg+Fe in the silicate portion) of 0.82 is consistent with some recent estimates for a starting composition for the lunar magma ocean and for the mare basalt source region; the derived lunar Mg# is similar to that for interplanetary dust particles, but is in conflict with that of the Earth's upper mantle (~0.89).

Thus, the bulk compositions of the Earth's upper mantle and the Earth's satellite are different. This conclusion enables us to restrict the number of hypotheses about the origin of the Moon. Fission and coaccretion hypotheses are not able to explain the compositional features of both planetary bodies. The capture event is practically unlikely, and no source region is known to produce bodies of Moon-like composition. The impact hypothesis – collision of a Mars-sized body with the Earth-appears adequate to account for both chemical and dynamical aspects if the protolunar material comes essentially from the mantle of the impactor. However, the same problem as in the capture hypothesis arises of how and where to produce bodies of Moon-like composition? The similarity in oxygen isotopes between Earth and Moon assumes that the impactor formed in the same part of the solar nebula as the Earth. Without specifying a mechanism of the origin of the Moon, we may conclude that the Earth and its satellite formed from compositionally different materials. composition of the Moon remains unusual in comparison with the Earth, the inner planets, chondrites, and achondrites.

Mars

Direct information on the bulk chemistry and structure of Mars is very limited. Recent observations (oxygen isotope ratios, trace element ratios, trapped rare gases, young crystalliaztion ages) have brought evidence that SNC meteorites (four Shergottites, three Nakhlites, and Chassigny) are Martian surface rocks ejected by huge impacts. By assuming that Mars is the parent body of SNC meteorites, the bulk composition of Mars is estimated (wt.%): 44.4% SiO_2, 30.2% MgO, 17.9% FeO, 2.5% CaO, and 3% Al_2O_3. Gross chemical characteristics of Mars are consistent with accretion from more volatile-rich material than the Earth, more extensive oxidation of Fe-metal, and separation of a Fe-Ni-S core.

In the bulk composition models enriched in FeO, the physical property distribution (density and seismic velocities) is essentially different form that in the Earth's mantle. Figure 15 shows that there is no sharp seismic discontinuity in the Martian mantle at 130–140 kbar (1100–1200 km) such as exists in the Earth at the same pressure range (400–420 km depth interval for the Earth). Thus, there is no distinctive separation into upper mantle and transition region. The Martian mantle may consist of three fairly extended zones: crust to

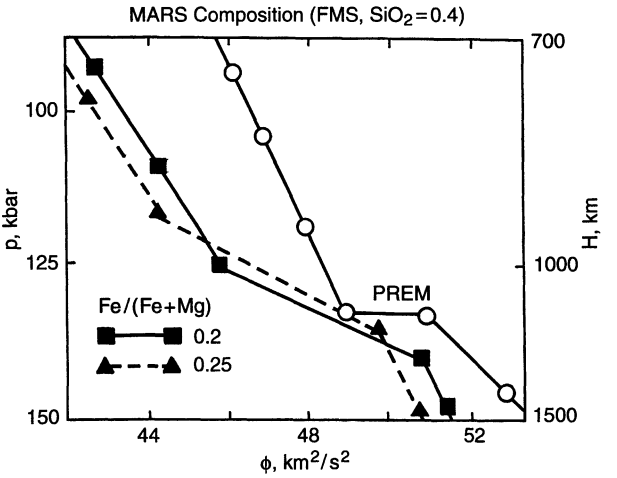

Fig. 15. Seismic parameter profiles ($\phi = V_p^2 - 4/3V_s^2$) in the Martian mantle for two bulk composition models: 40 mol.% SiO_2 and Fe/(Fe+Mg) = 0.2; 40 mol.% SiO_2 and Fe/(Fe+Mg) = 0.25. The PREM model for the Earth with the sharp discontinuous boundary at 134 kbar (400 km for the Earth) is shown for comparison

1000 km, first zone, 1000–1250 km, second (gradient zone); and 1250 km to the lower mantle (if it exists), third zone. Phase transformations are as follows:

$$\text{olivine+pyroxene+garnet} \xrightarrow{1000\ \text{km}} \text{olivine+spinel+pyroxene+garnet} \xrightarrow{1250\ \text{km}} \text{spinel+garnet}.$$

Models of the internal structure of Mars based on geophysical constraints using the mean density, moment of inertia, and gravitational field suggest that there is a core with radius amounting to from 1000 km for a pure iron core to 2000 km for an iron sulfide one.

Mercury

The observed mean density of Mercury of 5.44 g cm^{-3} implies an iron to silicate ratio in the range from 64:34 to 70:30, about twice that of any of the other terrestrial planets and the Moon.Three classes of models have been suggested to account for the anomalous composition of Mercury. One class of models employs scenarios which invoke differences in the physical properties (density, ferromagnetism, mechanical strength) of iron and silicates to achieve the required iron/silicate fractionation. A second class of models invokes the differing volatilities of iron and silicates to fractionate the two phases. A third class of models involves a scenario including major planetary collisions, which are suggested to blow off the bulk of the silicate mantle from the original Mercury protoplanet.

Venus

By its mechanical properties (mass $M = 8.815\ M_E$, mean density $\rho = 0.95\rho_E$, and mean radius $R = 0.95\ R_E$), Venus is the twin planet of the Earth. This suggests similarity in the bulk composition models, mineralogies, and structure between Venus and Earth. The content of iron in the Earth-like models of Venus is 2% less than that in the Earth. The present temperature of the upper layers of the Venusian mantle is near 1700 K; the temperature at the core-mantle boundary is 3500–4000 K, and is close to that of the Earth.

References

Barsukov VL, Bazilevsky AT, Volkov VP, Zharkov VN (eds) (1992) Venus geology, geochemistry and geophysics. The University of Arizona Press, Tucson

Basaltic volcanism study project (1981). Pergamon Press, New York

Florensky KP, Bazilevsky AT, Burba GA et al. (1981) Essays of comparative planetology. Barsukow VL (ed) Nauka, Moscow

Galimov EM (1995) Problem of the origin of the Moon. In: The main trends in geochemistry. The to 100th Anniversary of Academician AP Vinogradov, Nauka, Moscow, pp 8–43

Hartmann WK, Phillips RJ, Taylor GJ (eds) (1986) Origin of the Moon. LPI, Houston

Hood LL, Jones JH (1987) Geophysical constraints on lunar bulk composition and structure: a reassessment. J Geophys Res 92:E396–E410

Kieffer HH; Jakosky BM, Snyder CW, Matthews MS (eds) (1992) Mars. The University of Arizona Press, Tucson

Kuskov OL (1995) Constitution of the Moon: 3. Composition of the middle mantle form seismic data. Phys Earth Planet Inter 90:55–74

Kuskov OL, Panferov AB (1993) Thermodynamic models for the structure of the Martian upper mantle. Geochem Int 30 (8):132–143

Nakamura Y (1983) Seismic velocity structure of the lunar mantle. J Geophys Res 88:677

Neal CR, Taylor LA (1992) Petrogenesis of mare basalts: a record of lunar volcanism. Geochim Cosmochim Acta 56:2177–2212

Ringwood AE (1979) Origin of the Earth and Moon. Springer, Berlin Heidelberg New York

Saxena SK (ed) (1986) Chemistry and physics of terrestrial planets. Advances of physical geochemistry. Springer, Berlin Heidelberg New York

Taylor SR (1982) Planetary science: a lunar perspective. LPI, Houston

Taylor SR (1987) The unique lunar composition and its bearing on the origin of the Moon. Geochim Cosmochim Acta 51:1297–1309

1.8 Mineralogy of Meteorites and Asteroids

A.A. Ulyanov

1.8.1 "Family Tree" of Meteorite Classification

Meteorites are extraterrestrial rocks falling on the surface of our planet, as well as on other bodies of the Solar System. Most of them had elliptical orbits, which suggests that they formed inside our Solar System. Aphelias of the majority of measured and calculated meteorite orbits are in the asteroidal belt, which suggests that the asteroids are a possible source of meteorites.

Upon entry into the atmosphere, the surfaces of the meteorite are heated, melted, and ablated. Only a small fraction of the objects that enter in the atmosphere with appropriate speed and size can pass through the atmosphere to reach the Earth's surface as a meteorite. This raises the question as to whether the meteorites in our museum collections are representative of the objects in interplanetary space.

A meteorite passes through the atmosphere so quickly that the heat is restricted to the outer few millimeters. The interior part of the meteorite is unaltered by atmospheric passage.

Meteorites vary widely in mass and size, from micron-sized particles to large multiton masses. Very large bodies impact at high speeds, are completely destroyed, and may form a meteorite crater.

On the basis of their mineral and chemical composition, meteorites are divided into (Table 4):

1. *Stones*, consisting of magnesium-iron silicates, frequently with troilite and nickel-iron. Stones are further divided into chondrites and achondrites (see below).
2. *Stony-irons*, consisting of an approximately equal mixture of nickel-iron and silicates.
3. *Irons,* consisting essentially of nickel-iron with a small amount of accessory minerals.

There are also some isotopic classifications for meteorites, the most popular being based on oxygen isotopes (e.g., Clayton 1993).

Roughly 4000 meteorites, 1 kg or more in mass, fall to the Earth each year, and only a small percentage of these is recovered. By 1969 the world's meteorite collection comprised just over 3000 meteorites. Since then, more than 10 000 meteorites have been found in the hot and cold deserts of the Antarctic, Australia, and Africa. Some of these meteorites are members of new clans, and about 20 of them are samples from the Moon and Mars.

Figure 16 is a representation of the abundances of various classes of meteorites. The ratio of irons and stones in both finds and falls reflects the very easy identification of irons and their resistance.

Table 4. Classification of meteorites

Class	Subclass	Group	Subgroup	Principal minerals
Stones	Chondrites	Ordinary (OC)	H L LL	Olivine, bronzite, kamasite Olivine, hyperstene kamasite
		Enstatite (E)	EH EL	Enstatite, kamasite, troilite
		Carbonaceous (C)	CI CM CR	Olivine, pyroxene, phyllosilicates
			CV CO CK	Olivine, pyroxene
		Rumurutites (R)		Olivine, pyroxene
	Achondrites	Ca-poor achondrites	Aubrites Diogenites Ureilites	Enstatite Hypersthene Olivine, clynobronzite, FeNi
		Ca-rich achondrites	Angrites Eucrites Howardites	Augite Pigeonite, plagioclase Hypersthene, plagioclase
		Primitive achondrites	Winonaites Acapulcoites Lodranites	Olivine, pyroxene, plagioclase
		Lunar meteorites		Olivine, pyroxene, plagioclase
		Martian meteorites	Shergotites Nakhlites Chassignites	Olivine, pyroxene Diopside, olivine Olivine
Stony-irons	Pallasites			Olivine, kamacite, taenite
	Siderophyres			Orthopyroxene, kamacite, taenite
	Lodranites			Orthopyroxene, olivine, kamacite, taenite
	Mesosiderites			Pyroxene, plagioclase, FeNi
Irons	Hexahedrites			Kamacite
	Octahedrites			Kamacite, taenite
	Ataxites			Taenite, kamacite

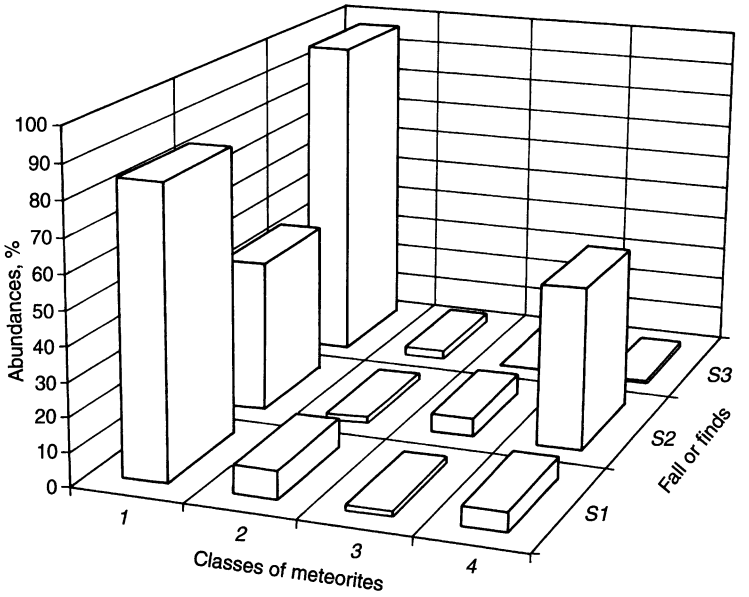

Fig. 16. Abundances of the various classes of meteorites *1* chondrites; *2* achondrites; *3* stony-irons; *4* irons among falls (*S1*) non-Antarctic (*S2*), and Antarctic (*S3*) finds

Table 5. Some mechanical properties of meteorites

Meteorites	Density (g/cm^3)	Porosity (%)
E-chondrites	3.5–3.8	
H-chondrites	3.6–3.8	13.1
L-chondrites	3.4–3.6	10.5
C-chondrites	2.2–3.6	24.4 (for CV)
Aubrites	3.2	4.3–15.1
Diogenites	3.3–3.4	
Ureilites	3.3	
Eucrites	3.1–3.2	14.8
Howardites	3.2–3.3	
Stony-irons	4.3–5.8	
Irons	7.8–8.0	

Meteorites are distinguished also by their main physical mechanical properties, some characteristics of which are summarized in Table 5.

1.8.2 Mineralogical Classification of Meteorites

Stone Meteorites

The prevailing class of meteorites is stones (Fig. 16), the *chondrites* being the most widespread. On some chemical and mineralogical parameters (bulk

MgO/FeO, abundance of metal, Ni/Fe ratio, MgO/FeO in silicates, and abundances of minor elements), textural features, the chondrites are subdivided into: *e*nstatite (E) chondrites, *o*rdinary (OC) chondrites, *c*arbonaceous (C) chondrites, and *r*umurutiites (R-chondrites). Some chondrites cannot be classified into any of these groups, and have been called anomalous, unique, or unclassified. Variations in chemical composition of some chondritic groups are given in Table 6. Van Schmus and Wood (1967) also divided the chondrites into different petrological types based on the degree of recrystallization and equilibration, which they ascribe to thermal metamorphism in the meteorite parent bodies. Chondrites have a peculiar texture, the main feature being the chondrules – predominantly silicate microspherules, the origin of which is widely debated among geologists (e.g., Sears et al., 1995). Chondrules are absent in the rare (but very important) carbonaceous chondrites of the CI clan; these meteorites were classified as chondrites, based on their chemical and mineralogical features. Chondrules may occupy a significant volume of the chondrite matter ($\geq 60\%$). They show considerable variation in form (difference in spherical degree and degree of recrystallization), sizes, internal texture (porphiritic, radial, barred, and other), and mineral and chemical composition. In the majority of cases, chondrules consist of olivine, pyroxene, plagioclase, and glass. Between the chondrules is a fine-grained matrix, the composition of which is frequently close to the average composition of chondrites. The textural features of different chondrites reflect differences in thermal metamorphism, recrystallization, and shock process (shock deformations, transformation of plagioclase into maskelenite). Thus, most of chondrites are breccias.

A comparison of the composition of chondrites and the solar photosphere (excluding H, He, and some other volatile elements), shows a remarkable similarity in elemental abundances. This distinguishes chondrites from terrestrial rocks. Chondrites contain appreciable quantities of lithophile, chalcophile, and siderophile elements, while terrestrial rocks, as a rule, are predominantly composed of lithophile elements. This suggests that the chondrites are samples of the matter of the early solar nebula, with only small degrees of fractionation of the chemical elements.

In enstatite chondrites almost all iron is in the metallic form, silicates contain very little iron. Variations in the contents of metal iron and other siderophile elements cause the enstatite chondrites to be divided into EH (*h*igh metal contents) and EL (*l*ow metal contents) chondrites. The enstatite chondrites are notable for their low degree of oxidation.

The amounts of metallic iron in ordinary chondrites decrease from H (*h*igh metal contents) through L (*l*ow metal contents) to LL (*l*ow-*l*ow metal contents) chondrites, while the amounts of iron in the silicates increase along the same sequence. Ordinary chondrites are more oxidized than enstatite chondrites.

Of special interest are the carbonaceous chondrites, which have high iron contents, almost entirely in the silicates. The carbonaceous chondrites are characterized by a different degree of oxidation of iron. The carbonaceous chondrites also contain high concentrations of the volatile elements and compounds,

Table 6. Chemical compositions of selected subgroups of meteorites. (After Lavruchina 1973; Yavnel' 1973)

	SiO_2	TiO_2	Al_2O_3	Cr_2O_3	$FeO+Fe_2O_3$	MnO	MgO	CaO	Na_2O	P_2O_5	Σ sil.	FeNi	FeS	Fe_{total}	Σ Fe/SiO_2
Irons	–	–	–	–	–	–	–	–	–	–	0	95–100	0–5	80–93	–
Pallasites	17.0	0.00	0.38	0.68	6.65	0.08	19.8	0.28	0.07	–	45.3	54.04	0.53	54.5	3.22
Mesosiderites	19.5	0.08	4.1	0.36	7.08	0.22	6.4	2.9	0.21	0.2	42.4	50.7	2.83	52.5	2.68
H-chondrites	36.5	0.13	2.43	0.36	8.87	0.25	23.5	1.82	0.85	0.23	75.0	18.9	5.35	27.5	0.755
L-chondrites	39.9	0.13	2.31	0.44	13.1	0.27	25.0	1.9	0.88	0.24	84.3	8.9	6.17	21.8	0.546
Carbonaceous chondrites	33.0	0.11	2.53	0.49	22.0	0.24	23.0	2.32	0.72	0.38	84.8	–	13.6	25.7	0.78
Enstatite chondrites	38.0	0.06	1.87	0.35	1.70	0.14	21.0	0.97	1.00	0.20	65.7	21.6	10.7	7.2	0.72
Aubrites	54.1	0.22	0.91	0.14	1.64	0.06	36.0	1.32	0.12	–	94.4	2.5	1.25	12.1	0.039
Chassinites	37.4	0.07	0.52	0.73	28.0	0.16	32.2	0.11	0.11	–	98.5	0.63	0.88	22.4	0.6
Diogenites	52.1	0.01	1.4	0.32	17.2	0.19	25.9	0.00 4	0.004	–	98.0	0.82	1.12	14.0	0.27
Ureilites	38.9	0.07	0.80	0.35	13.0	0.09	35.7	0.43	0.05	–	90.0	8.3	–	18.16	0.46
Eucrites	47.6	0.43	13.0	0.36	16.6	0.47	8.46	10.2	0.43	0.09	98.2	1.18	0.56	14.4	0.30
Howardites	49.3	0.1	9.95	0.53	17.1	0.66	11.8	7.7	0.33	0.08	99.0	0.45	0.60	14.0	0.27
Nakhlites	48.8	0.38	1.73	0.33	20.7	0.09	12.0	15.1	0.40	–	99.8	–	0.16	16.2	0.33

including water, carbon, sulfur, rare gases, and considerable amounts of organic substances. Currently, there are six subgroups of carbonaceous chondrites (CI, CM, CO, CV, CR, and CK named after typical members: *I*vuna, *M*urray, *O*rnans, *V*igarano, *R*enazzo, and *K*aroonda, respectively).

The organic compounds of carbonaceous chondrites are of special interest. They include complex organic acids, hydrocarbons, and heterocyclic compounds of C, H, S, N, O, and Cl. Despite their complexity, the organic compounds in carbonaceous chondrites are of abiogenic origin.

Expect for the carbonaceous chondrites, the mineral compositions the members of each chondrite group are mostly uniform. More than 300 minerals are known to be present in chondrites, but many are rare accessory phases (see below). The main minerals of chondrites are olivine and orthopyroxene; small quantities of plagioclase (or/and maskelinite), and the Ca-rich pyroxenes (pigeonite and diopside) are also present. The usual opaque accessories for chondrites are kamacite – α-(Fe, Ni), taenite – γ-(Fe, Ni), and troilite – FeS.

There are many differences between chondritic and terrestrial mineralogy. The common minerals in chondrites are magnesium-iron silicates, while in the Earth's crust the common minerals are quartz and aluminosilicates. Nickel-iron is very rare in terrestrial rocks, and some chondritic minerals have not been found in the Earth's crustal materials. Most chondrites are composed of anhydrous minerals, while hydrated minerals are abundant on Earth.

The mineral composition of different chondritic groups is related to their chemical compositions.

The mineral composition of carbonaceous chondrites (especially the CI-type) also reflects their high degree of oxidation and hydration. CI-chondrites consist mainly of amorphous hydrated silicates, minerals of the serpentine group, and sulfates. In other carbonaceous chondrites the amounts of hydrated silicates are essentially less, and the dominant minerals are olivine and pyroxene.

Characteristic features of carbonaceous chondrites are low abundances of metallic iron and troilite, and large variations in mineral chemistry.

Most carbonaceous chondrites (except the CI-type)) contain white inclusions characterized by high concentrations of calcium, aluminum, and other refractory elements. These inclusions are distinguished by their peculiar textures, anomalies in the isotopic composition of many elements, and complex mineralogical composition (simultaneous presence of both high-temperature minerals – hibonite, spinel, melilite, perovskite, and low-temperature minerals – nepheline, sodalite, and others). High abundances in these Ca, Al-rich inclusions (CAIs) of elements, the condensation temperature of which is very high, provide the foundation for the assumption that these inclusions represent high-temperature mineral assemblages which condensed from high-temperature nebula in the early stages of Solar System evolution (e.g., Wark and Lovering 1977; Grossman 1980). This hypothesis was adopted by many researchers; however, it has not been commonly accepted. It was also suggested that CAIs formed as residues from the selective evaporation of primary silicate materials (e.g., Kurat et al. 1975). More recently, these hypotheses have been modified to include processes involving

multistage events of alteration (e.g., MacPherson 1988). However, the question of the sequence of these events is still the subject of considerable debate.

Recent data on several unusual meteorites with affinities to ordinary chondrites made the addition of new chondritic group necessary. Weisberg et al. (1991) termed these unusual meteorites Carlisle Lakes type chondrites. Recently, additional meteorites belonging to this group have been described. The relatively large number of these meteorites justifies the definition of a new group of chondrites. Schulze et al. (1994) suggest naming this new chondritic group R-chondrites (rumurutiites) after Rumuruti, the only fall; all other examples of these meteorites are finds from hot and cold deserts in Antarctica, Australia, and Africa. R-chondrites can be characterized as oxidized, olivine-rich, metal-poor chondrites. The chemical composition and oxygen isotopic composition of these meteorites distinguished them from the other chondrite groups; therefore, these chondrites do not belong to carbonaceous, ordinary, or enstatite chondrites, although they exhibit some similarities to ordinary chondrites.

About 10% of all stony meteorites are *achondrites.* The chemical composition of achondrites is not identical (see Table 6). Usually, achondrites are subdivided into Ca-rich (5–25 wt.% CaO) and Ca-poor (0.1–3 wt.% CaO) achondrites. In Table 4 we presented an additional three groups: primitive achondrites, lunar meteorites, and martian meteorites. The compositions and textures of the two main subgroups of achondrites – eucrites and howardites – are very similar to those of terrestrial igneous rocks. This suggested that achondrites are the products of magmatic differentiation on the meteorite parent bodies. On the other hand, many achondrites have breccia textures similar to those of some chondritic meteorites. Sometimes, plagioclase in achondrites is transformed into maskelenite. Breccia textures and the presence of maskelenite show that some achondrites have undergone impact metamorphic processes. In particular, in ureilites small crystal of diamonds were identified, whose origin may be connected with impacts. Some achondrites with igneous texture may have formed at crystallization of shock melts. Winonaites, lodranites, and acapulcoites are subgroups of the primitive achondrites, that have mineral and bulk compositions similar to those of chondrites, but have nonchondritic textures, and their oxygen isotopic compositions indicate that they were formed on different parent bodies.

Iron Meteorites

The number of iron meteorites takes second place among meteorites. The contents of nickel in them varies widely from 4 to 60%. Expect for Fe and Ni, the iron meteorites contain minor elements such as Co, S, Cu, Cr, and C. Irons are characterized by extremely low abundances of lithophile elements; their composition is rather peculiar and clearly differs from the solar abundances of elements. Probably, the matter of these meteorites was formed either during selective condensation and subsequent accretion processes, or as a result of magmatic differentiation in protoplanetary bodies. The irons consist of two

main mineral phases: kamasite (4–7% Ni) and taenite (15–60% Ni). There are some inclusions of shreibersite, troilite, daubreelite, cohenite, graphite, and/or silicates, and phosphates.

The iron meteorites are divided into separate groups, based on the contents of nickel and minor elements (Ga, Ge, Ir, Pt), as well as the structural relationships of kamasite and taenite.

The most widespread group of irons is octahedrites, containing up to 14% Ni. They differ by a peculiar texture, known under the name of Widmanstatten structure: the system of parallel kamasite bands is located in parallel to the sides of the octahedron. The interstition between the plates is filled by taenite and plessite (a fine-grained mixture of kamasite and taenite).

The group of iron meteorites, distinguished by low contents of nickel (less than 6% Ni) and consisting almost wholly of kamasite monocrystals (sometimes more than 0.5 m in size), has received the name hexahedrites.

The third group, ataxites, has no ordered structure. The meteorites of this group differ by their high contents of nickel (more than 14% Ni) and consist of plessite (up to 27% Ni), taenite, and kamasite.

The contents and distribution of nickel in iron meteorites and their peculiar texture testify that this class of meteorite has undergone a melting stage in the history of iron formation. Iron meteorites have undergone numerous intensive shock loads and heating; as a result, there are shock deformations and a number of features of mineral texture in some irons.

On the basis of changes in nickel concentration between taenite and kamasite (on the assumption that the observable picture was formed as a result of nickel diffusion form taenite into kamasite), the cooling speed of iron meteorites can be calculated. From data of Levin and Simonenko (1977), in an interval from 700 up to 500 °C the cooling speed is about 2 °C for 1 Ma: from data of Wood (1971) 1–10 °C for 1 Ma at an interval from 600 to 400 °C. The radiuses of parent bodies are assumed in the order of 50–200 km.

Stony-Iron Meteorites

The class of stony-iron meteorites is an insignificant part of meteorites. Stony-iron meteorites consist of silicates and nickel-iron (in approximately quantities). Meteorites of this class differ by unique textures, representing nickel-iron fragments, cemented together by a silicate matrix, or essentially silicate fragments of different chemical and mineralogical compositions, cemented together by a mixture of nickel-iron and sulfides.

The metal in stony-iron meteorites is kamasite (taenite is rare), having an octahedrite structure. The silicate part basically consists of olivine, orthopyroxene, and plagioclase. Prevailing minerals are in the basis of division of stony-iron meteorites on several subclasses or groups (see Table 4). Some stony-iron meteorites are characterized by breccia texture of silicate parts. The structure and mineral composition of stony-iron meteorites testify that they have passed through a stage of magmatic differentiation.

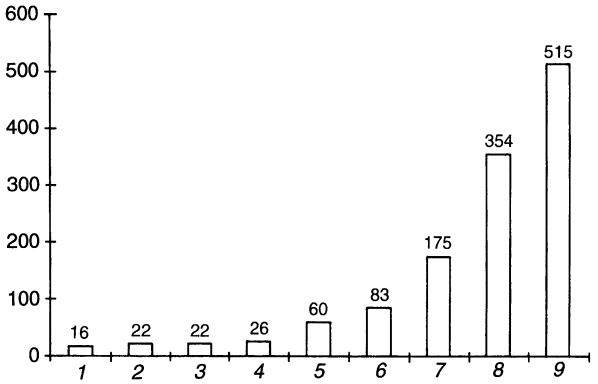

Fig. 17. Number of mineral phases and their varieties recognized in extraterrestrial materials. Data from: *1* Tschermak 1885; *2* Farrington 1915; *3* Heide 1934; *4* Krinov 1955; *5* Mason 1967; *6* Mason 1972; *7* Yudin and Kolomensky 1987; *8* Ulyanov 1991; *9* this chapter

1.8.3 Summary of Extraterrestrial Minerals

Today, more than 500 mineral phases and their varieties are recognized in extraterrestrial materials (meteorites, tectites, interplanetary dust particles, etc.) (Fig. 17).

Reviews of meteorite mineralogy were provided by Mason (1967, 1972), Yudin and Kolomensky (1987), Petaev (1988), Ulyanov (1991), and Yaroshevsky and Ulyanov (1994). These reviews and abstracts of *Lunar and Planetary Science Conferences, Annual Meetings of the Meteoritical Society, Symposiums on Antarctic Meteorites, Russian Meteorite Conferences*, and some publications on meteorite mineralogy in scientific journals (mainly Geochimica et Cosmochimica Acta, Meteoritics, Geochimiya, Meteoritika, etc.) were used to prepare the following list of extraterrestrial minerals. This comprehensive review of space mineralogy included as non-doubtful minerals (normal font in tables) as doubtful minerals, varieties of mineral phases, incompletely described mineral phases (italic font in remarks) in meteorites, tectites, interplanetary dust particles, and cosmic spherules. Table 7 and remarks also include minerals produced by terrestrial weathering of meteorites.

1.8.4 Interstellar Mineral Grains in Meteorites

Some chondrites (so-called primitive meteorites) contain submicroscopic grains of diamond, graphite, SiC, and some other mineral phases. From the extremely anomalous isotopic ratios, originally of noble gases, it is presumed that these grains have an extrasolar system origin and many have formed within stellar atmospheres (e.g. Ott 1993; Zinner 1995). Therefore their formation

Table 7. Native Elements

Mineral	Formula	Crystal system
Kamasite	α-(Fe,Ni)	Cubic
Taenite	γ-(Ni-Fe)	Cubic
Awaruite	Ni_2Fe-Ni_3Fe	Cubic
Wairauite	CoFe	Cubic
Epsilon-iron	ε-(Fe,Ni)	Hexagonal
Tetrataenite	FeNi	Tetragonal
Nickel	Ni	Cubic
Zhanghenite	CuZn	Cubic
Zincum	(Zn, Fe)	Hexagonal
Platinum	Pt	Cubic
Osmium	(Os,Ru)	Hexagonal
Rhenium	(Re, Ru)	Hexagonal
Iridium	Ir	Cubic
Titanium	Ti	Hexagonal
Copper	Cu	Cubic
Sulfur	S	Orthorhombic
Diamond	C	Cubic
Graphite	C	Hexagonal
Lonsdaleite	C	Hexagonal
Chaoite	C	Hexagonal

Fe-metal (Fe,Ni); *α-Fe* (Fe,Ni); *Si-rich Fe,Ni-Metal* (Fe,Ni,Si) (up to 15% Si); *Co-rich kamasite* (up to 7.6% Co; Co > Ni); *Si-rich kamasite* (up to 3.8% Si); *high-Co, low-Ni metal phase* ($FeCo$-Fe_3Co_2); *Ge-rich awaruite* up to 1.5% Ge; *Ni,Cr-alloy* (Ni,Cr); *Ni,Cu-alloy* (Ni,Cu); *(Zn,Fe)* up to 4% Fe; *(Fe,Ni)Zn_{13}, (Fe,Ni)Zn_{10}; (Fe,Ni)Zn_7, (Fe,Ni)$_3Zn_{10}$; (Fe,Ni)$_3Zn_7$; Fe,Pt-alloy* (Fe,Ni,Pt); *ferroan platinum* PtFe; *Fe,Ni,Ir,Os,Ru-alloy; Pt-alloy* (Pt,Fe,Ni); *Pt,Ir-alloy* (Pt,Ir,Fe,Ni); *Os,Ru-alloy* (Os,Ru); *Ru,Os-alloy* (Ru,Os); *Ru,Os,Fe,Ni,Re-alloy; Os, Ru, Ir, Re, Mo,W-alloy; Ni,Pt-alloy* (Ni,Pt,Fe); *Fe,Ir,As,Mo,Pt-alloy; Mo,Fe,Ni-alloy; native gold* Au; *Au,Ag,Fe-alloy; Mo,Fe,Ni-alloy* (Fe,Ni,Mo); *vanadium* V; *phosphorus* P; *carbon* C; *cliftonite* C, *rustenburgite* Pt_3Sn.

Carbides, nitrides, oxynitrides, phosphides, silicides, and silicophosphides

Cohenite	$(Fe,Ni)_3C$	Orthorhombic
Moissanite	SiC	Hexagonal
Haxonite	$(Fe,Ni)_{23}C_6$	Cubic
Osbornite	TiN	Cubic
Carlsbergite	CrN	Cubic
Roaldite	$(Fe,Ni)_4N$	Cubic
Sinoite	Si_2N_2O	Orthorhombic
Barringerite	$(Fe,Ni)_2P$	Hexagonal
Schreibersite	$(Fe,Ni)_3P$	Tetragonal
Perryite	$(Ni,Fe)_5(Si,P)_2$	Cubic
Suessite	$(Fe,Ni)_3Si$	Cubic

Epsilon-carbide; Fe_3C_2; SiC; TiC; Zr,Mo,Ti-carbide; chalipite Fe_2C; *Ti_2N_2O; Cr-cohenite* $(Fe,Ni,Cr)_3C$; *Fe,Cr-carbide* $(Fe,Cr)_2C$; *Si_3N_4; Fe-barringerite* Fe_2P; *Ni-barringerite* $(Ni,Fe)_2P$; *Cr-barringerite* $(Fe,Cr,Ni)_2P$; *rhabdite* $(Fe,Ni)_3P$; *Fe-Ni-silicide* $(Fe,Ni)_2(Si,P)$; *Fe,Cr, Ni-phosphide* $(Fe,Ni)_5CrP_3$; *Fe,Ti,Ni-phosphide* (Fe,Ni) TiP.

Table 7 (continued)

Sulfides, tellurides, and sulfotellurides		
Pentlandite	$(Fe,NI)_9S_8$	Cubic
Troilite	FeS	Hexagonal
Mackinawite	$(Fe,Ni)_9S_8$	Tetragonal
Pyrrhotite	$Fe_{1-x}S$ (x = 0–0.17)	Monoclinic, hexagonal
Pyrite	FeS_2	Cubic
Bravoite	$(Fe,Ni)S_2$	Cubic
Molybdenite	MoS_2	Hexagonal
Tungstenite	WS_2	Hexagonal
Heazlewoodite	Ni_3S_2	Trigonal
Cinnabar	HgS	Trigonal
Covellite	CuS	Hexagonal
Sphalerite	ZnS	Cubic
Alabandite	MnS	Cubic
Oldhamite	CaS	Cubic
Niningerite	(Mg,Fe)S	Cubic
Chalcopyrite	$CuFeS_2$	Tetragonal
Bornite	Cu_5FeS_4	Cubic
Cubanite	$CuFe_2S_3$	Orthorhombic
Violarite	$FeNi_2S_4$	Cubic
Daubreelite	$FeCr_2S_4$	Cubic
Millerite	NiS	Trigonal
Heideite	$(Fe,Cr)_{1+x}(Ti,Fe)_2S_4$	Monoclinic
Brezinaite	Cr_3S_4	Monoclinic
Caswellsilverite	$NaCrS_2$	Trigonal
Djerfisherite	$K_6(Fe,Cu,Ni)_{24}S_{26}Cl$	Cubic
Cooperite	PtS	Tetragon
Laurite	$(Ru,Os,Ir)S_2$	Cubic
Erlichmanite	$(Os,Ru,Ir)S_2$	Cubic
Chalcosine	Cu_2S	Monoclinic
Moncheite (chengbolite)	$PtTe_2$	Trigonal
Altaite	PbTe	Cubic

Co-pentlandite $(Fe,Ni,Co)_9S_8$ (up to 3.5% Co; Co>Ni); *Cr-pentlandite* $(Fe,Ni,Cr)_9S_8$; *Cu-pentlandite* (up to 13% Cu); *Ti-troilite* (Fe,Ti)S up to 14% Ti; *Mn-troilite* (up to 1.5% Mn); *Zn-troilite* (up to 4.4% Zn); *Ni-troilite* (up to 2.5% Ni);); *Cr-troilite* up to 13% Cr; *Cr,Ni-troilite* (up to 15% Cr and 8% Ni); *Cr,Ni-pyrrhotite* (up to 1.9% Cr and 2.7% Ni); *marcasite* FeS_2; *Fe-sphalerite (= marmatite)* up to 35% Fe; *Ga-sphalerite* (up to 3.7% Ga); *Ferroalabandite* (Mn,Fe)S; *Ag-alabandite* (Mn,Fe, Ag)S (up to 10% Ag); *Cr-alabandite* up to 4% Cr; *ferroniningerite* (Fe,Mg)S; *Mn-niningerite* up to 32% Mn; *chalcopyrrhotite; Cu,Fe-sulfide* 48% Cu, 12% Fe; *Cr,Fe-sulfide* 14–452% Cr and 55–23% Fe; *gentnerite* $Cu_8Fe_3Cr_{11}S_{18}$; *Zn-daubreelite* $(Fe,Zn)Cr_2S_4$ up to 10% Zn; *V-daubreelite* $Fe(Cr,V)_2S_4$ up to 1.2% V; *Ag-daubreelite* up to 0.75% Ag; *Mn-daubreelite* $(Fe,Mn)Cr_2S_4$ up to 3.5% Mn; *CrS; Cr_2S_3; $AgCrS_2$; $AgCr_2S_4$; Ag-sulfide; K,Cr,Ni,Fe sulfide* up to 3% K, 4% Cr, 18% Ni; *Ni_5GeS; Cr-sulfide* up to 30% Cr; *Na,Cr-sulfide; Na,Cu,Cr-sulfide* up to 5% Na, 34% Cr, and 15% Cu; *Na,Cu, Zn,Cr-sulfide* up to 2% Na, 33% Cr, 8% Cu, and 10% Zn; *Mn,Cu-sulfide; V-sulfide; Ti,Cr,Fe-sulfide* up to 40% Ti, 10% Cr, and 10% Fe; *wurtzite* ZnS; *Zn,Fe,Mn-sulfide* (Zn, Fe, Mn)S; *Fe,Zn,Ni,Cr-sulfide* ~50% Fe, 20–25% Zn, 2–3% Ni, and 1–3% Cr; *Fe,Pt,Ni-sulfide* $(Fe,Pt,Ni)_2S_3$ (?); *Pt,Ru,Ir,Os-sulfide* $(Pt,Ru,Ir,Os)_2S$ (?); *Fe,Ru,Ni,Pt,Ir-sulfide* (Fe, Ru, Ni, Pt, Ir)$_9$S (?); *Mg-sulfide* MgS; *Pt,Au-telluride; Fe,Pt,Cu-sulfutelluride* $Cu(Fe,Pt)_3(S,Te)_3$ (?).

Table 7 (continued)

Oxysulfides and hydrated sulfides		
Tochilinite	$6Fe_{0.9}S*5(Mg,Fe)(OH)_2$	Triclinic
Schollhornite	$Na_{0.3}CrS*2H_2O$	Trigonal

Valleriite $4(Fe,Cu)S*3(Mg,Fe)(OH)_2$; *Fe,Ni-oxysulfide; hydrated Na,Cu,Cr-sulfide* up to 32% Cr, 18% Cu, and 1% Na; *hydrated Fe,Cr-sulfide* $FeCr_2S_4*nH_2O$ (?); *β-phase* $8FeS*9(Ca_{0.8}Fe_{0.2})O*0.3P_2O_5$; *hydrated Ca,Cr-sulfide.*

Oxides		
Cuprite	Cu_2O	Cubic
Periclase	MgO	Cubic
Wustite (= iozite)	FeO	Cubic
Bunsenite	NiO	Cubic
Maghemite	γ-Fe_2O_3	Tetragon
Corundum	Al_2O_3	Trigonal
hematite	α-Fe_2O_3	Trigonal
Escolaite	Cr_2O_3	Trigonal
Baddeleyite	ZrO_2	Monoclinic
α-Quartz	SiO_2	Trigonal
Crystobalite	SiO_2	Tetragonal
Tridimite	SiO_2	Monoclinic, Triclinic
Coesite	SiO_2	Monoclinic
Opal	SiO_2*nH_2O	Amorphous
Rutile	TiO_2	Tetragonal
Brookite	TiO_2	Orthorhombic
Thorianite	$(Th,U)O_2$	Cubic
Spinel	$MgAl_2O_4$	Cubic
Hercynite	$FeAl_2O_4$	Cubic
Coulsonite	FeV_2O_4	Cubic
Magnetite	$FeFe_2O_4$	Cubic
Pleonast	$(Mg,Fe)Al_2O_4$	Cubic
Trevorite	$NiFe_2O_4$	Cubic
Chromite	$(Fe,Mg)Cr_2O_4$	Cubic
Magnesiochromite	$(Mg,Fe)Cr_2O_4$	Cubic
Magnesioferrite	$MgFe_2O_4$	Cubic
Ulvospinel	$TiFe_2O_4$	Cubic
Alumochromite	$(Mg,Fe)(Al,Cr)_2O_4$	Cubic
Perovskite	$CaTiO_3$	Orthorhombic
Pyrophanite	$MnTiO_3$	Trigonal
Ilmenite	$FeTiO_3$	Trigonal
Geikilite	$MgTiO_3$	Trigonal
Grossite	$CaAl_4O_7$	Monoclinic
Hibonite	$CaAl_{12}O_{19}$	Hexagonal
Armalcolite	$(Mg,Fe)Ti_2O_5$	Orthorhombic
Zirconolite (= zirkelite)	$(Ca,Th,Ce)Zr(Ti,Nb)_2O_7$	Monoclinic
Pyrochlor	$(Ca,REE,Th)_2(Nb,Ti,Zr,Al)_2O_7$	Cubic

Fe-rich periclase (Mg,Fe)O; *magnesiowustite* (Fe,Mg)O; *Ni-maghemite* γ-$(Fe,Ni)_2O_3$; *Ti-rich corundum* $(Al,Ti)_2O_3$; *δ-Al_2O_3; V-oxide* V_2O_3; *Bioxide* Bi_2O_3; *pseudobrookite* $(Fe^{3+},Fe^{2+})_2Fe^{3+},Ti)O_5$; *$ZrTiO_4$; Nb-rich rutile* up to 4% Nb_2O_5; *anatase* TiO_2; *cassiterite* SnO_2; *V-spinel* *$Mg(Al,V)_2O_4$* (up to 3% V_2O_3; *Cr-spinel* $Mg(Al,Cr)_2O_4$ (up to 17% Cr_2O_3); *Cr-hercynite* $Fe(Al,Cr)_2O_4$ (up to 7.7% Cr_2O_3); *Mn-magnetite* $(Fe,Mn)Fe_2O_4$ (up to 4% MnO); *Cr-magnetite* $Fe(Fe,Cr)_2O_4$ (up to 7% Cr_2O_3; *V-magnetite* $Fe(Fe,V)_2O_4$ (up to 22% V_2O_3); *Ti-magnetite* $(Fe,Ti)Fe_2O_4$; *Ni-magnetite* $(Fe,Ti)Fe_2O_4$; (up to 9% NiO); *Cr,V-magnetite* $Fe(Fe,V,Cr)_2O_4$ up to 8% Cr_2O_3 and 23% V_2O_3; *Cr-pleonast* $(Mg,Fe)(Al,Cr)_2O_4$ (up to 18% Cr_2O_3); *V-pleonast* $(Mg,Fe)(Al,V)_2O_4$ (up to 27% V_2O_3); *Zn-pleonast* $(Mg,Fe,Zn)Al_2O_4$ (up to 2.3% ZnO); *ferrochromite* $FeCr_2O_4$; *alumoferrochromite* $Fe(Cr,Al)_2O_4$; *Mn-chromite* $(Fe,Mn)Cr_2O_4$; *Ti-chromite* up to 10% TiO_2; *Ti-alumochromite; Al-magnesiochromite; Mn-magnesiochromite; Zn,Mn-magnesiochromite; ScY,REE-perovskite* $(Ca,Sc,Y,REE)TiO_3$ (up to 6% Y_2O_3 and 1.6% Sc_2O_3); *V-perovskite* $Ca(Ti,V)O_3$ (up to 1.5% V_2O_3); *Nb-rich perovskite* $Ca(Ti,Nb)O_3$; *V-ilmenite* $Fe(Ti,V)O_3$ (up to 2% V_2O_3); *Mn-ilmenite* $(Fe,Mn)TiO_3$ (10–20% MnO); *Mg-ilmenite* $(Fe,Mg)TiO_3$ (7–10% MgO); *Mn,Mg-ilmenite* $(Fe,Mn,Mg)TiO_3$ (up to 19% MnO and 10% MgO); *V-rich hibonite* up to 3% V_2O_3; *$CaAl_2O_4$; $CaAl_{24}O_{37}$; V-rich aluminate* $Ca_4(Al,V)_{20}O_{40}$; *Sc-aluminate; Ti_4O_7; Ti_5O_9; Ti_6O_{13}; Ti_8O_{15}; Ti_9O_{17}; $Ti_{10}O_{19}$; Mg-armalcolite* $(Mg,Fe)Ti_2O_5$; *Cr,Zr-armalcolite* up to 9% Cr_2O_3 and 1.2% ZrO_2; *Al_2TiO_5; zirkelite-like mineral; Ca,Al,Ti,Mg-oxide; Ti,Ca,Mg, Al-oxide; Ti,Ca,Sc,Zr-oxide; Zr,Y-oxide; V-oxide* V_2O_3; *(Ti,Zr,Si)(Al,Ti)$_2O_5$; mineral-T* $(Ca,Mg)Ti_3O_7$; *Ti,Ca,Mg,Al-oxide; Ti,Ca,Sc,Zr-oxide; Ca,Al,Ti,Mg-oxide; Ca,V-oxide.*

Hydrated oxides and hydrooxides

Goethite	α-FeO(OH)	Orthorhombic
Akaganeite	β-FeO(OH,Cl)	Tetragonal
Lepidocrokite	γ-FeO(OH,Cl)	Orthorhombic
Brucite	$Mg(OH)_2$	Tetragonal
Gibbsite	$Al(OH)_3$	Orthorhombic
Ferrihydrite	$5Fe_2O_3*9H_2O$	Hexagonal
Portlandite	$Ca(OH)_2$	Hexagonal

S-Ni-rich ferrhydrite; $Ni(OH)_2$; gell of Fe-hydroxide; hollandite $(Fe_{15}Ni)(O_{12}(OH)_{20})Cl(OH)_2$.

Sulfates, phosphates, carbonates, silicophosphates, wolframates, molybdates, vanadates

Anhydrite	$CaSO_4$	Orthorhombic
Barite	$BaSO_4$	Orthorhombic
Epsomite	$MgSO_4*7H_2O$	Orthorhombic
Gypsum	$CaSO_4*2H_2O$	Monoclinic
Bloedite	$Na_2Mg(SO_4)_2*4H_2O$	Monoclinic
Melanterite	$FeSO_4*7H_2O$	Monoclinic
Copiapite	$FeFe_4(SO_4)_6(OH)_2*20H_2O$	Triclinic
Jarosite	$KFe_3(SO_4)_2(OH)_6$	Triclinic
Hexahydrite	$MgSO_4*6H_2O$	Monoclinic
Buchwaldrite	$NaCaPO_4$	Orthorhombic
Brianite	$Na_2CaMg(PO_4)_2$	Monoclinic
Panetite	$(Na,Ca,K)_2(Mg,Fe,Mn)_2(PO_4)_2$	Monoclinic
Farringtonite	$Mg_3(PO_4)_2$	Monoclinic
Sarcopside	$(Fe,Mn,Mg)_3(PO_4)_2$	Monoclinic
Beusite	$Fe_{1.5}Mn_{1.5}(PO_4)_2$	Monoclinic
Graftonite	$(Fe,Mn,Ca)_3(PO_4)_2$	Monoclinic

Table 7 (continued)

Sulfates, phosphates, carbonates, silicophosphates, wolframates, molybdates, vanadates		
Stanfieldite	$Ca_4Mg_3Fe_2(PO_4)_6$	Monoclinic
Whitlokite (= merrillite)	$Na_2Ca_{18}Mg,Fe)_2(PO_4)_{14}$	Trigonal
Chladniite	$Na_2CaMg_7(PO_4)_6$	Hexagonal
Maricite	$FeNaPO_4$	Orthorhombic
Collinsite	$Ca_2(Mg,Fe,Ni)(PO_4)_2*2H_2O$	Triclinic
Cassidyite	$Ca_2(Ni,Mg)(PO_4)_2*2H_2O$	Triclinic
Lipscombite	$(Fe,Mn)Fe_2(PO_4)_2(OH)_2$	Tetragonal
Vivianite	$Fe_3(PO_4)_2*8H_2O$	Monoclinic
Monazite	$CePO_4$	Monoclinic
Arupite	$Ni_3(PO_4)_2*8H_2O$	Monoclinic
Chlorapatite	$Ca_5(PO_4)_3Cl$	Hexagonal
Fluorapatite	$Ca_5(PO_4)_3F$	Hexagonal
Calcite	$CaCO_3$	Trigonal
Vaterite	$CaCO_3$	Hexagonal
Magnesite	$MgCO_3$	Trigonal
Siderite	$FeCO_3$	Trigonal
Rhodochrosite	$MnCO_3$	Trigonal
Dolomite	$CaMg(CO_3)_2$	Trigonal
Ankerite	$CaFe(CO_3)_2$	Trigonal
Breunnerite	$(Fe,Mg)CO_3$	Monoclinic
Nyerereite	$Na_2Ca(CO_3)_2$	Orthorhombic
Barringtonite	$MgCO_3*2H_2O$	Triclinic
Hydromagnesite	$Mg_5(CO_3)_4(OH)_2*4H_2O$	Monoclinic
Nesquehonite	$Mg(HCO_3)(OH)*2H_2O$	Monoclinic
Reevesite	$Ni_6Fe_2(CO_3)(OH)_{14}*4H_2O$	Trigonal
Sheelite	$CaWO_4$	Tetragonal
Powellite	$CaMoO_4$	Tetragonal

Bassanite $2CaSO_4*H_2O$; *Fe,Ni-sulfate; Mg-sulfate; Fe-merrillite* (Na,Ca) $Ca_{18}(Fe,Mg)_2(PO_4)_{14}$; *Ca-merrillite* (Ca,Na)$Ca_{18}(Mg,Fe)_2(PO_4)_{14}$; *REE-merrillie* Ca_{18} $(Y,REE)_2$ $(Mg,Fe)_2(PO_4)_{14}$; *Na,Fe-phosphate* $(Fe,Na,Mn)_3(PO_4)_2$ (up to 5% Na_2O); *Na,Fe-phosphate* $Na(Mg,Fe)_{2.5}(PO_4)_2$; *Fe-phosphate; Mg,Na,K-phsophate* up to 7% Na_2O and 5% K_2O; *Mg,Ca,Fe,Na-silicophosphate; Fe,Mn,Na,K-phosphate* $(Na,K)_2(Fe,Mn)_8(PO_4)_6$; *Fe,Mn,K,Na-phosphate* $(Na,K)_2(Fe,Mn)_8(PO_4)_6$; *Mg,Ni,K-phosphate; Na,Mg-phosphate* $Na_{1+x}Mg(PO_4)F$; *Na,Ti-phosphate* $Na_2Ti(PO_4)_2$; *Ca-phosphate; hydroxylapatite* $Ca_5(PO_4)_3(OH)$; *aragonite* $CaCO_3$; *Mn-siderite* $(Fe,Mn)CO_3$; *Mn-dolomite* $Ca(Mg,Mn)(CO_3)_2$; *hydrophase II* $Mg(HCO_3)(OH)*6H_2O$; *zaratite* $Ni_3(CO_3)(OH)_4*4H_2O$; *molybdosheelite* $Ca(W,Mo)O_4$; *Ca-vanadate; Ru-rich Ca,Fe-molybdate-phosphate; Fe-molybdate; Fe-molybdate-vanadate; Fe-vanadate.*

Orthosilicates		
Forsterite	$Mg_2[SiO_4]$	Orthorhombic
Olivine	$(Mg,Fe)_2[SiO_4]$	Orthorhombic
Fayalite	$Fe_2[SiO_4]$	Orthorhombic
Montichellite	$CaMg[SiO_4]$	Orthorhombic
Kirschsteinite	$CaFe[SiO_4]$	Orthorhombic
Almandine	$Fe_3Al_2[SiO_4]_3$	Cubic
Grossular	$Ca_3Al_2[SiO_4]_3$	Cubic
Andradite	$Ca_3Fe_2[SiO_4]_3$	Cubic
Majorite	$Mg_3(Fe,Si)_2[SiO_4]_3$	Cubic
Zircon	$Zr[SiO_4]$	Tetragonal

Table 7 (continued)

Ringwoodite	γ-$(Mg,Fe)_2[SiO_4]$	Cubic
Wadsleyite	β-$(Mg,Fe)_2[SiO_4]$	Orthorhombic
Kyanite	$Al_2[SiO_4]O$	Triclinic
Sphene (= titanite)	$CaTi[SiO_4]O$	Monoclinic
Akermanite	$Ca_2Mg[Si_2O_7]$	Tetragonal
Melilite	$Ca_2(Mg,Al)[(Si,Al)SiO_7]$	Tetragonal
Gehlenite	$Ca_2Al[AlSiO_7]$	Tetragonal
Cordierite	$(Mg,Fe)_2Al_3[AlSi_5O_{18}]$	Orthorhombic
Roedderite	$(Na,K)_2(Mg,Fe)_5[Si_{12}O_{30}]$	Hexagonal
Merrihueite	$(Na,K)_2(Fe,Mg)_5[Si_{12}O_{30}]$	Hexagonal
Osumulite	$(K,Na)(Fe,Mg)_2(Al,Fe)_2(Al,Fe)_3[(Si,Al)_{12}O_{30}]$	Hexagonal
Yagiite	$(Na,K)_{1.5}Mg_2(Al,Mg,Fe)_3[(Si,Al)_{12}O_{30}]$	Hexagonal

Mn-forsterite $(Mg,Mn)_2[SiO_4]$ (up to 2.7% MnO); *Cr-forsterite* up to 0.65% Cr_2O_3; *Ca-rich olivine* up to 12% CaO; *Ni-olivine* up to 0.7% NiO; *Cr-olivine* up to 1.4% Cr_2O_3; *P-olivine-* $(Mg,Fe)_2[(Si,P)O_4]$ l(up to 5% P_2O_5); *Fe-montichellite* $Ca(Mg,Fe)[SiO_4]_3$; *Mg-kirschsteinite* $Ca(Fe,Mg)[SiO_4]$; *grossular-andradite* $Ca_3(Al,Fe)_2(SiO_4)$; *hydrogarnet; cocharite* $Mg_3Fe_2-[SiO_4]_3$; *pyrope* $Mg_3Al_2[SiO_4]_3$; *humite* $3Mg_2SiO_4*Mg(F,OH)_2$; *vesuvianite* $Ca_{10}(Mg, Fe)_2Al_4-[SiO_4]_5[Si_2O_7]_2(OH,F)_4$; *pumpellyite* $Ca_2(Al,Fe)_3[SiO_4]$ $[Si_2O_7](OH)_2*nH_2O$; *epidot* $Ca_2Al_2-FeSi_3O_{12}(OH)$; *prehnite* $Ca_2Al_2Si_3O_{10}(OH)$; *Na-melilite* $(Ca,Na)_2(Mg,Al)[(Si,Al)SiO_7]$; *Ca,Ti,Al-silicate* $Ca_3Ti(Al,Ti)_2[(Si,Al)_3O_{14}]$.

Pyroxenes, pyroxenoides and amphiboles

Clinoenstatite	$Mg_2[Si_2O_6]$	Monoclinic
Clinobronsite	$(Mg,Fe)_2[Si_2O_6]$	Monoclinic
Clinohypersthene	$(Fe,Mg)_2[Si_2O_6]$	Monoclinic
Pigeonite	$(Mg,Fe,Ca)(Mg,Fe)$ $[Si_2O_6]$	Monoclinic
Augite	$(Ca,Na)(Mg,Fe,Al,Ti)[(Si,Al)_2O_6]$	Monoclinic
Diopside	$CaMg[Si_2O_6]$	Monoclinic
Omphacite	$(Ca,Na)(Mg,Al)[Si,Al)_2O_6]$	Monoclinic
Salite	$Ca(Mg,Fe)[Si_2O_6]$	Monoclinic
Ferrosalite	$Ca(Fe,Mg)[Si_2O_6]$	Monoclinic
Hedenbergite	$CaFe[Si_2O_6]$	Monoclinic
Fassaite	$(Ca,Mg,Fe)(Mg,Fe,Al)[(Si,Al)_2O_6]$	Monoclinic
Jadeite	$Na(Al,Fe)[Si_2O_6]$	Monoclinic
Kosmochlor (= ureyite)	$NaCr[Si_2O_6]$	Monoclinic
Enstatite	$Mg_2[Si_2O_6]$	Orthorhombic
Bronzite	$(Mg,Fe)_2[Si_2O_6]$	Orthorhombic
Hypersthene	$(Fe,Mg)_2[Si_2O_6]$	Orthorhombic
Ferrohyperstene	$(Fe,Mg)_2[Si_2O_6]$	Orthorhombic
Wollastonite	$Ca_3[Si_3O_9]$	Triclinic
Rhodonite	$CaMn_4[Si_5O_{15}]$	Triclinic
Rhonite	$Ca_2(Mg,Fe)_4FeTiO_2[Si_3Al_3O_{18}]$	Triclinic
Krinovite	$Na_2Mg_4Cr_2O_2[Si_6O_{18}]$	Triclinic
Sapphirine	$(Mg,Al)_7(Mg,Al)O_2[Al,Si)_6O_{18}]$	Triclinic
Pyroxferroite	$(Fe,Mn,Ca)_7[Si_7O_{21}]$	Triclinic
Richterite	$Na_2Ca(Mg,Fe)_5[Si_8O_{22}](F,OH)_2$	Monoclinic
Kaersutite	$NaCa_2(Mg,Fe)_4Ti[Si_6Al_2O_{22}](OH)O$	Monoclinic

Table 7 (continued)

Cr-clinoenstatite up to 0.7% Cr_2O_3; *Al-clinohypersthene; Mn-augite; ferroaugite; Cr,Mn-augite* up to 2.7% Cr_2O_3 and 2.6% MnO; *Mn-enstatite* up to 19% MnO; *Al-enstatite* up to 7.5% Al_2O_3; *Ni-bronsite* up to 0.3% Ni; *Cr-hyperstene* up to 2.5% Cr_2O_3; *Cr-diopside* up to 2.3% Cr_2O_3; *Fe-fassaite; Mg-fassaite; Cr-fassaite* up to 2.4% Cr_2O_3; *Sc-fassaite* up to 18% Sc_2O_3 and 8% ZrO_2; *Al,Ti-fassaite; V-fassaite* up to 10.3% V_2O_3; *Ti-fassaite* up to 18% TiO_2; *acmite* $Na(Al,Fe)[Si_2O_6]$; *aegirine* $NaFe[Si_2O_6]$; *magnesiorichterite* $Na_2Ca(Mg,Fe)_5[Si_8O_{22}]-(F,OH)_2$; *ferrokaersutite* $NaCa_2(Fe,Mg)_4Ti[Si_6Al_2O_{22}](OH)O$; *mullite* $Al[Al_xSi_{2-x}O_{5.5-0.5x}]$.

Phyllosilicates

Kaolinite	$Al_4[Si_4O_{10}](OH)_8$	Triclinic
Serpentine (= chrysotile)	$Mg_6[Si_4O_{10}](OH)_8$	Monoclinic
Lizardite	$Mg_6[Si_4O_{10}](OH)_8$	Trigonal and hexagonal
Antigorite	$Mg_6[Si_4O_{10}](OH)_8$	Monoclinic
Clinochrysotile	$Mg_6[Si_4O_{10}](OH)_8$	Monoclinic
Berthierine	$(Fe,Mg)_{4-6}(Si,Al)_4O_{10}(OH)_8$	Monoclinic
Talc	$Mg_3[Si_4O_{10}](OH)_2$	Monoclinic and triclinic
Pyrophyllite	$Al_2[Si_4O_{10}](OH)_8$	Monoclinic and triclinic
Montmorillonite	$(Na,Ca)_{0.3}(Al,Mg)_2[Si_4O_{10}](OH)_2*nH_2O$	Monoclinic
Saponite (= kerolite)	$(Ca,Na)_{0.3}(Mg,Fe)_3[Si_4O_{10}](OH)_2*nH_2O$	Monoclinic
Clinochlor	$(Mg,Fe)_5Al[AlSi_3O_{10}](OH)_8$	Monoclinic
Chamosite	$(Fe,Mg)_5Al[AlSi_3O_{10}](OH)_8$	Monoclinic
Kronstedtite	$Fe_4Fe_2[Fe_2Si_2O_{10}](OH)_8$	Monoclinic and trigonal
Greenalite	$Fe_6[Si_4O_{10}](OH)_8$	Monoclinic
Clintonite	$Ca(Mg,Al)_3[Al_3SiO_{10}](OH)_2$	Monoclinic
Margarite	$CaAl_2[Al_2Si_2O_{10}](OH,F)_2$	Monoclinic

Alumoserpentine $(Mg,Al)_{6-x}[Si_4O_{10}](OH)_8$; *Ni-serpentine* $(Mg,Ni)_6[Si_4O_{10}](OH)_8$; *pecoraite* $Ni_6[Si_4O_{10}](OH)_8$; *ferroantigorite* $(Mg,Fe)_6[Si_4O_{10}](OH)_8$; *metahalloysite* $Al_4[Si_4O_{10}](OH)_8$; *Na-talc; sericite* $KAl_2[AlSi_3O_{10}](OH,F)_2$; *muscovite* $KAl_2[AlSi_3O_{10}](OH,F)_2$; *phlogopite* $KMg_3[AlSi_3O_{10}](OH,F)_2$; *Na-phlogopite* $(Na,K)Mg_3[AlSi_3O_{10}](OH)_2$; *seladonite* $K(Fe,Al)-(Mg,Fe)(OH)_2[Si_4O_{10}]*nH_2O$; *vermiculite* $(Mg,Fe,Al)_3[(Al,Si)_4O_{10}](OH)_2*4H_2O$; *Na-saponite* $(Na, Ca)_{0.3}(Fe,Mg)_3[Si,Al)_4O_{10}](OH)_2*nH_2O$; *ferrosaponite* $(Ca,Na)_{0.3}(Fe,Mg)_3[(Si,Al)_4O_{10}]-(OH)_2*nH_2O$; *pennine; ripidolite; hysingerite* $Fe_4Si_4O_{10}(OH)_8*4H_2O$; *palygorskite* $(Mg,Al)_2-Si_4O_{10}(OH)*4H_2O$; *sepiolite* $Mg_4Si_6O_{15}(OH)_2*6H_2O$.

Alumosilicates of the frame structures

Albite	$Na[AlSi_3O_8]$	Triclinic
Oligoclase	$Ab_{90-70}An_{10-30}$	Triclinic
Andesine	$Ab_{70-50}An_{30-50}$	Triclinic
Labradore	$Ab_{50-30}An_{70-50}$	Triclinic
Bitownite	$Ab_{10-30}An_{90-70}$	Triclinic
Anortite	$Ca[Al_2Si_2O_8]$	Triclinic
Celsian	$Ba[Al_2Si_2O_8]$	Monoclinic
Nepheline	$(Na,K)[AlSiO_4]$	Hexagonal
Sodalite	$Na_8[AlSiO_4]_6Cl_2$	Cubic

Table 7 (continued)

K-feldspar; anortoclase; sanidine $K[AlSi_3O_8]$; *kalsilite* $K[AlSiO_4]$; *maskelenite* $(Na,Ca)[Al(Al,Si)Si_2O_8]$; *scapolite* $(Na,Ca)_4[Al(Al,Si)Si_2O_8](Cl,CO_3)$; *meionite* $Ca_4(Al_2Si_2O_8)CO_3$; *5-1-zeolite; 4-4-1-zeolite; S6r/D6R-zeolite; chabasite* $(Ca,Na)_2[Al_2Si_4O_{12}]*6H_2O$; *ferrierite* $(Na,K)_2Mg[(Si,Al)_{18}O_{36}](OH)*9H_2O$; *stilbite* $NaCa_2Al_5Si_{13}O_{36}*14H_2O$.

Halides

Halite	NaCl	Cubic
Sylvite	KCl	Cubic
Lawrencite	$(Fe,Ni)Cl_2$	Trigonal
Molysite	$FeCl_3$	Hexagonal

Organic minerals

Weddellite	$CaC_2O_4*H_2O$	Tetragonal

Mineral Phases with Unknown Structures

Ni-rich Mg,Ca,Al,Na,K-silicate; Na,Mg,Ca,Fe,Al-silicate; Hydrated Ni-phillosiliate; Na,-K,Al-silicate $(K,Na)[AlSi_5O_{12}]$; *Fe,Ca,Al-silicate; Cr-silicate* $Ca_{0.5}Mg_{0.5}Fe_{0.2}Cr_{0.5}[SiO_4]$, *Na,Ti-silicate.*

Mineral Mixtures and Glasses

Glasses; lechatelierite; iddingsite; plessit. HAP (= *h*igh *a*luminum *p*hyllosilicate); *LAP* (= *l*ow *a*luminum *p*hyllosilicate); *PCP* [= *p*oor (or *p*artly) *c*haracterized *p*hase].

environment was plasma (Cassidy and Kern 1993) – an electrically neutral gas containing a high proportion of its component molecules in the ionized state, with charge balance satisfied by the presence of free electrons.

Until now diamond, graphite, chaoite, SiC, TiC, corundum, spinel, and Si_3N_4 have been identified as interstellar grains in meteorites. Early work on interstellar material in meteorites has been reviewed by Anders (1988); for recent reviews, see Anders and Zinner (1993) and Ott (1993). Many interstellar grains in meteorites are presolar and have extremely anomalous isotopic compositions which indicate circumstellar origin. Type II supernova have previously been proposed as stellar sources of these presolar grains (Amari et al. 1994a, Zinner et al. 1995). Meyer et al. (1995) report yields for a large number of isotopes in eight distinct zones in the ejecta form a 25 M⊙ supernova.

High $^{12}C/^{13}C$ and $^{16}O/^{17}O$ and low $^{16}O/^{18}O$ ratios in some graphite and SiC grains show the signature of the He/C zone in presupernona stars. The dominant components for isotopically anomalous noble gases in these grains show the signature of the *s*-process (neutron capture on a *s*low time scale) and appa-

rently come from AGB (*A*symptotic *G*iant *B*ranch) stars (Amari et al. 1994b). Moreover, two extreme types of *s*-Kr imply two kinds of AGB-stars with different mean neutron exposures. In additional to neon from AGB-stars, He-burning shells of interstellar graphite grains also contain monoisotopic ^{22}Ne from the β^+-decay of ^{22}Na ($t_{1/2} = 2.58$ a), which was chemically trapped in grains. The short half-life of ^{22}Ne requires a short time scale, and suggests the presence in interstellar graphite grains of material form nova and supernova ejects. Thus, interstellar graphite includes contributions from different stars and their shells.

Additional evidence of the presence of nova and supernova materials in interstellar grains comes from the large variety and unusual isotopic compositions of potassium and calcium, reflecting their stellar sources. Some interstellar grains have ^{41}K excesses due to the decay of ^{41}Ca($t_{1/2} = 1.03 \times 10^5$ a) and ^{44}Ca excesses due to the decay of short-lived ^{44}Ti ($t_{1/2} = 52$ a). Evidence for ^{41}Ca and ^{44}Ti in some interstellar grains strongly suggests mixing between the C-rich and O-rich zones and contributions from the innermost zone to the supernova ejecta from which the grains formed. Thus, the wide range of isotopic ratios for different chemical elements in interstellar grains provides additional evidence for extensive and deep heterogeneous mixing in supernova explosions, confirming astronomical observations and hydrodynamic calculations. Moreover, isotopic data suggest that interstellar grains in primitive meteorites include contributions from different known star sources: AGB-stars, supernovae, novae, and perhaps Wolf-Rayet (WR) stars (Amari et al. 1995).

Isotopic featuries and properties of interstellar grains in different types of primitive chondrites (Cl, CM, CV EH, LL, etc.) with the exception of grain size, are very similar. Differences in grain sizes of interstellar components may represent size sorting or selective destruction of fine-grained material in the nebula (Gao et al. 1995).

Since interstellar grains formed in stellar atmospheres, their investigation provides information on different processes (nuclear, chemical, etc.) in stars. The first kind of information to be obtained from isotopic studies of interstellar grains in meteorites is the number of stellar sources that admitted material into the solar system (e.g., Alexander 1993; Zinner 1995). The second is obtained "from single-grain isotopic data that either have no counterpart in astronomical observations or that cannot be explained by existing models of nucleosynthesis and thus provide stimulation for further theoretical works" (Zinner 1995; e.g., Meyer et al. 1995).

Interstellar grains were found not only in meteorites. Brilliant et al. (1992) studied the isotopic composition of nitrogen in lunar soil separates. They found that the nitrogen release and isotope profile of the major component corresponded exactly to that encountered when interstellar diamonds from primitive meteorites are analyzed before removal of contaminating organic material. Therefore, these authors tentatively interpret isotopic data as the first recognition of interstellar grains in the lunar regolith. Unfortunately, we know of no appropriate investigations to confirm this conclusion.

Isotopic data from Yates et al. (1992) strongly suggest that interstellar grains are in terrestrial sedimentary rocks (e.g., cryoconite – dark sediments from temporary ice lakes on the Greenland ice sheet; it contains both melted extraterrestrial sperules and unmelted micrometeorites). Thus, the sources of interstellar grains for laboratory investigations may be not only primitive chondrites.

1.8.5 Cosmic Spherules in Terrestrial Environments

Cosmic spherules are subspherical to spherical objects produced by melting *i*nterplanetary *d*ust *p*articles (IDPs) and large objects during atmospheric entry. Evidence that precursors of these spherules are extraterrestrial material has been presented by many investigators (see, e.g., Taylor and Brownlee 1991). Most of the cosmic spherules form the Antarctic and Greenland ice caps, deep-sea sediments, ancient oceanic deposits, and salt formations are melted IDPs. On the basis of mineral and chemical composition, IDPs are divided into three main types. ***Iron spherules*** (I-type) consist of magnetite crystal and interstitial wustite. Some of the iron spherules contain Fe-Ni metal beads and small Pt-group nuggets (Brownlee et al. 1984). *High-iron **glassy** spherules* (G-type) compositionally have over 50% FeO and are predominantly dendritic magnetite in a glassy matrix. Some of them also contain Fe-Ni metal beads. ***Stony** spherules* (S-Type) are the most common type and composed of olivine, magnetite, and glass. Bonte et al. (1987) found Pt-group nuggets in them. Work by Taylor and Brownlee (1991) on cosmic spherules with different ages and from a variety of sedimentary environments suggests that proportions of spherule types change as a function of time, with the number of iron spherules increasing with the age of the sample. However, it is not clear, if this variation in spherule types represents a real change in the meteoroid complex or is a result of differential weathering of spherules in the Earth's environment.

1.8.6 Stages in the Complex Processes of Meteorite Origin

A key problem in meteoritics is that of the origin of meteorites. In this question there are two points of view, which however, do not completely exclude one another. According to the first, meteorites are fragments of asteroids; according to the second, fragments of nucleis of "dead" comets.

Both points of view are based on the same facts – parameters of orbits and features of the chemical composition of matter. At present, the most convincing is the hypothesis of an asteroidal origin of meteorites.

One of the important questions in the problem of the origin of meteorites is the question of the character of the protomaterial of their parent bodies. The isotopic composition of bulk meteorites shows minimum differences from the suggested initial protoplanetary substance, and is primary; that is, the distribu-

tion of isotopes approximate averages their contents on the Sun and in processes of nucleo synthesis. The analysis of the chemical and isotopic composition of meteorites has allowed many researchers (e.g., Wood 1971; Wasson 1985; Heide Wlotzka 1995) to suggest that the composition of carbonaceous chondrites CI-type (except hydrogen, helium, and some other volatile components), as well as the ratios of major chemical elements (for example, Na/Ca, S/Ca) are close to solar values. This can be specified by genetic relationships between the substance of CI-chondrites and the Sun. The presence of volatile components and hydrous silicates in CI-chondrites permits considering the latter as matter not altered by essential changes and heat for the past 4.5×10^9 years, and reflecting the primary composition of gas-dust nebula. The chondritic meteorites of types other than CI were changed more significantly. Their textures, bearing bright attributes of thermal recrystallization, show that these types of chondritic materials were subjected to essential heating (possibly up to 800 °C) (Wood 1971). However, most chondrites did not pass through the stage of complete melting. On the contrary, the composition and texture of achondrites, stony-iron meteorites, and most irons, specify that they are probably products of a remelting process.

The systematization of the extensive data on meteorite research has allowed a general scheme of origin meteorites (Wood 1971, 1988; McSween 1987). Under this scheme, the parent bodies of meteorites are asteroids, formed as a result of condensation and aggregation of solid materials from gas-dust nebula and having a primary composition close to composition of carbonaceous chondrite.

At the beginning of geological history ($\sim4.5\times10^9$ years ago), the internal parts of asteroids were subjected to strong heating (source of heat could be, for example, decay of ^{26}Al or ^{60}Fe), partial or complete melting, and igneous differentiation of substance. The external parts of parent bodies have not undergone heating. They were considerably heated up, but nonremelting took place in intermediate layers. Fragments of internal layers of asteroids are probably achondrites, stony-iron meteorites, and some irons. The chondritic meteorites represent fragments of an intermediate layer, and carbonaceous chondrites the material of the outside (unaltered) part of asteroids.

The formation of asteroids occurred in various parts of the asteroid belt, characterized by some features of chemical composition. These features of chemical composition can be determined in the observed composition of meteorites. This scheme of formation of meteorites is widely believed, but not unique. There are reasonable representations (Vinogradov 1971; Dodd 1986), that some separate classes and groups of meteorites could be formed directly as a result of condensation and agglomeration from high-temperature nebula.

There are several main stages in the history of formation of meteoritic materials. A complex sequence of events is recorded in the micro- and macrochemical, isotopic, and textural patterns of meteorite minerals. We can resolve the following discrete stages.

The interstellar stage. Atoms had an existence prior to the collapse of the interstellar material which formed the Sun and protosolar nebula. Some refractory objects and the matrix in some types of chondrites appear to preserve presolar grains with unusual isotopic patterns.

Solar nebula stage. The young Sun was surrounded by a rotating disk of gas and dust. Interstellar dust accreting to the young Sun was transformed at high temperature into the chondrules and some kind of inclusions.

Aggregation of chondrite components stage. After the chondrite components were formed, they aggregated into planetosimales. Accreting solids were not uniform in composition.

Stage of metamorphic alteration and igneous melting. After the accretion stage was finished, chondrite planetosimales were heated internally. Two types of alterations have been observed in different chondrites (Wood 1988): anhydrous metamorphism at relatively high temperature (700–1200 K) and low-temperature hydrothermal metamorphysm that altered mafic mineral phases into clay minerals. In the interior parts of planetosimales, solid materials may be melted. As a result of this process, achondritic magmas and other silicate-metal-sulfide melts may be generated.

Collisions of planetosimale stage. As a result of the collision of planetosimales, the latter grew in size and became asteroids.

Ejection stage. Some planetosimales were disturbed by shock events and small fragments were ejected into space.

Orbital evolution stage. Initially near-circular heliocentric orbits of these fragments were perturbed by the gravity of large planets, into elliptical orbits and were captured by Earth. The time during which meteorites existed as small fragments in space is typically a few tens of millions of years.

Fall to the Earth stage. During the atmospheric flight, the fragments were friction-heated and their surfaces were melted, but melted materials is ablated as fast as it is heated.

After falling to the Earth. The "terrestrial life" of meteorites begins. Less than 1% of fall meteorites have been collected. Most fall meteorites weather and become the substance of the Earth's crust.

Different minerals in space bodies are indicators of all of these stages in the history of the formation materials that we now call meteorites.

1.8.7 Meteorite Ages

The absolute ages of meteorites, dating the time of their chemical fractionation by melting in the parent bodies determined by ^{207}Pb-^{206}Pb, ^{87}Rb-^{87}Sr, or ^{187}Re-^{187}Os methods [$4.4-4.7\times10^9$ years (Birk et al. 1975; Church 1975; Minster and Allegre 1976)], correspond to (at present) the accepted time of age of the Solar System, and are one of the proofs of the simultaneous origin of the Earth and the parent bodies of meteorites.

The ages of retaining rare gases in meteorites (or ages of cooling and crystallization of molten material), determined by $^{40}K/^{40}Ar$- and U-Th-He-methods, give various interpretations, which change from 0.5 to 4.5×10^9 years (Dymek et al. 1976; Jessberger et al. 1977; Schultz and Signer 1977; Wasserburg and Burnett 1978).

These variations reflect the effects of collisions of meteorite parent bodies, the heating-up of these bodies, with their partial or complete melting, and loss of gases. In general, in the interpretation of data on meteorite ages, it is always necessary to take into account, that the geological history of meteorites can be rather complex. Secondary processes (especially shock metamorphism) frequently yield rejuvenation values for the absolute age of meteorites. Moreover, it is necessary to consider that some meteorites are breccia and consist of separate clasts with a different igneous history.

In addition to the ages of differentiation and crystallization of meteorites, there are cosmic-ray ages, which characterize the duration of irradiation after the reduction of the meteorite to meter-sized fragments. These ages determine the time since the moment of breakup of the meteorite parent bodies (as a result of shock processes); that is the time of the independent existence of a meteorite in space. Cosmic-ray irradiation ages of meteorites are much shorter than the ages of differentiation and gas retention. The space ages are different for the various groups of meteorites.

1.8.8 Isotopic Composition and Isotopic Anomalies of Elements in Meteorites

Studies of the isotopic composition of Mg, Cr, Ag, Tl, U, and Xe in samples from primitive meteorites have established the presence of several short-lived nuclides with a mean life $\geq\sim1$ Ma in the early Solar System (Wasserburg 1985; Cameron 1993). The presence of these nuclides in the early Solar System solids manifests itself in an excess in their daughter nuclide concentrations (e.g., ^{26}Mg in the case of ^{26}Al). A list of some radioactive nuclei and their decay products is given in Table 8. Although a "fossil" origin for such excesses was also suggested (see, e.g., Clayton 1986), the experimental data, particularly the correlation between the excess in the daughter nuclide concentration and abundance of the stable isotope in the parent elements (e.g., correlation of excess ^{26}Mg in CAIs with their ^{27}Al content), argues against such a proposition. These stu-

Table 8. Short-lived nuclides

Parent	Product	$T_{1/2}$Ma
^{41}Ca	^{41}K	0.15
^{99}Tc	^{99}Ru	0.21
^{60}Fe	^{60}Ni	0.3
^{36}Cl	^{36}Ar	0.31
^{26}Al	^{26}Mg	0.72
^{53}Mn	^{53}Cr	3.7
^{98}Tc	^{98}Ru	4.2
^{107}Pd	^{107}Ag	6.5
^{182}Hf	^{182}W	9
^{205}Pb	^{205}Tl	14
^{247}Cm	^{235}U	16
^{129}I	^{129}Xe	17
^{244}Pu	^{232}Th, SF	82
^{146}Sm	^{142}Nd	103

dies have also suggested possible heterogeneities in the distribution of ^{26}Al in the solar nebula, and have helped in elucidating the processes leading to the formation of the CAIs themselves (e.g., MacPherson et al. 1988). The studies of coarse-grained CAIs, in particular, showed relationsships specific between their magnesium isotopic compositions and petrological types. For example, some type B1 CAIs are characterized by the presence of ^{26}Mg excess due to decay of extinct ^{26}Al, and yield well-behaved Mg-Al isochrons with $(^{26}Al/^{27}Al)_9$ at the time of formation of these inclusions, clustering around the value 5×10^{-5}. The Mg-Al systematics in the type B2 CAIs, on the other hand, are often disturbed, and are characterized by a lower value for $(^{26}Al/^{27}Al)_0$, indicating late disturbances in the magnesium isotopic systematics due to reequilibrium of magnesium isotopes and/or heterogeneity in the distribution of ^{26}Al in the solar nebula (Goswami et al. 1994).

The presence of short-lived nuclides in early Solar System solids limits the time interval between the last addition of freshly synthesized material to the solar nebula and the formation of these solids. Obviously, this time interval can be better limited through the observation of radionuclides with the shortest mean life. Until very recent times, ^{26}Al, with a mean life of 1 Ma, was the shortest-lived radionuclide whose presence in the early Solar System was conclusively established. Recently, the search for other shorter-lived nuclides (e.g., ^{36}Cl, ^{41}Ca, ^{60}Fe, ^{99}Tc, etc.) has yielded conclusive results (e.g., Srinivasan et al. 1994). These studies have presented strong evidence in favor of the presence of short-lived nuclides with a mean life of <1 Ma in the early Solar System.

Another type of isotopic effect found in meteorites also appears to call for some memory of the chemical state in which nuclei were carried into the solar nebula (Meyer et al. 1995). These effects include ^{16}O excesses (Clayton et al. 1973) and correlated ^{48}Ca, ^{50}Ti, and ^{54}Cr isotopic anomalies (e.g., Ireland 1990) in CAIs from carbonaceous chondrites. Then understanding of these isotopic

effects would aid in constructing the chemical history of matter in the interstellar medium.

1.8.9 Links Between Asteroids and Meteorites

Almost all meteorites are derived from the asteroidal belt. A comparison of asteroid and meteorite spectra should identify the possible meteorite parent bodies. However, only a few asteroids with unique spectral characteristics have been linked with some meteorite types. They include: (1) asteroid 4 Vesta, which for more than 20 years has been debated as the parent body for the HED (howardite, eucrite, and diogenite) basaltic achondrites; (2) asteroids 19 Fortuna and 13 Egeria appear to be possible CM chondrite parent bodies; (3) asteroid 3103 Eger has spectral characteristics very similar to aubrites, and (4) small asteroid 3628 (estimated diameter 7 km) could be the source body for ordinary chondrites (e.g., Binzel et al. 1993, Burbine and Binzel 1995). A discrepancy between the observed flux of ordinary chondrite meteorites and the virtual lack of observed ordinary chondrite asteroids may be due to two processes (Binzel et al. 1993): (1) space weathering alters the surface of asteroids and, therefore, changes the spectral characteristics; (2) ordinary chondrite bodies exist only among small asteroids. Continued spectroscopic surveys of asteroids hold exciting promise for further success.

References

Alexander CMO'D (1993) Presolar SiC in chondrites: how variable and how many sources. Geochim Cosmochim Acta 57:2869–2888

Amari S, Lewis RS, Anders E (1994a) Interstellar grains in meteorites: III. Graphite and its noble gases. Geochim Cosmochim Acta 59:1411–1426

Amari S, Zinner E, Lewis RS (1994b) C-, N-, O-, Si-, and Ti-isotopic ratios of low density graphite grains from Murchison indicate a supernova origin. Lunar Planet Sci 25: 2728

Anders E (1988) Circumstellar material in meteorites, noble gases, carbon, and nitrogen. In: Kerridge JF, Matthews MS (eds) Meteorites and the early solar systm. University of Arizona Press, Tucson, pp 927–955

Anders E, Zinner E (1993) Interstellar grains in primitive meteorites: Diamond, silicon carbide, and graphite. Meteoritics 28:490–514

Binzel RP, Xu S, Bus SJ, Skrutskie MF, Meyer M, Knezek P, Barker ES (1993) The asteroid-meteorite connection: the discovery of a main belt ordinary chondrite asteroid. Meteoritics 28:324

Birk JL, Minster JF, Allegre CJ (1975) ^{87}Rb-^{87}Sr chronology of achondrites. Meteoritics 10:364–365

Bonte Ph, Jehanno C, Maurette M, Brownlee DE (1987) Platinum metals and microstructure in magnetic deep sea cosmic sperules. Proc Lunar Planet Sci Conf 17:E641–E648

Brilliant DR, Franchi IA, Arden JW, Pillinger CT (1992) An interstellar component in the lunar regolith. Meteoritics 27:206–207

Brownlee DE, Bates BA, Wheelock MM (1984) Extraterrestrial platinum group nuggets in deep-sea sediments. Nature 309:693–695

Burbine TH, Binzel RP (1995) Could G asteroids be the parent bodies of the CM chondrites? Meteoritic 30:494
Cameron AGW (1993) Nucleosynthesis and star formation. In: Levy EH, Lunine J (eds) Protostars and planets III. University of Arizona Press, Tucson
Cassidy WA, Kern CM (1993) Primordial mineral growth in a plasma. Meteoritics 28:335–336
Church SE (1975) Radiogenic isotope research. Rev Geophys Space Phys 13:98–101
Clayton DD (1986) Interstellar fossil ^{26}Mg and its possible relationship to excess meteoritic ^{26}Mg. Astrophys J 310:490–198
Clayton RN (1993) Oxygen isotopes in meteorites. Ann Rev Earth Planet Sci 21:115–119
Clayton RN, Grossman L, Mageda TK (1973) A component of primitive nuclear composition in carbonaceous meteorites. Science 182:485–488
Dodd RT (1986) Meteorites. Petrology and geochemistry. Moscow, Mir, 384 pp (in Russian)
Dymek RF, Albee AL, Chodos AA, Wasserburg GJ (1976) Petrography of isotopically dated clasts in the Kapoeta howardite and petrologic constraints on the evolution of its parent body. Geochim Cosmochim Acta 40:1115–1130
Farrington OS (1915) Meteorites, Published by the author, Chicago, Illinois
Gao X, Nittler LR, Swan PD, Walter RM (1995) Presolar grains in Indarch. Meteoritics 30:508
Goswami JN, Srinivasan G, Ulyanov AA (1994) Ion microprobe studies of Efremovka CAIs: I. Magnesium isotope composition. Geochim Cosmochim Acta 58:431–447
Grossman L (1980) Refractory inclusions in the Allende meteorite. Annu Rev Earth Planet Sci 8:559–608
Heide F (1934) Kleine Meteoritenkunde. Springer, Berlin Heidelberg New York
Heide F, Wlotzka F (1995) Meteorites. Messengers from space. Springer, Berlin Heidelberg New York
Ireland T (1990) Presolar isotopic and chemical signatures in hibonite-bearing refractory inclusions from the Murchison carbonaceous chondrite. Geochim Cosmochim Acta 54:3219–3237
Jessberger EK, Standacher Th, Dominik B, Herzog GF (1977) Ar^{40}-Ar^{39} dating of the Pueblo-to de Allende meteorite. Meteoritics 12:266–269
Krinov EL (1955) The basis of meteoritika. Moscow, Gostechizdat, 392 pp (in Russian)
Kurat G, Hoinkes G, Fredriksson K (1975) Zoned Ca-Al-rich chondrule in Bali: new evidence against the primordial condensation model. Earth Planet Sci Lett 26:140–144
Lavruchina AK (1973) Differenciation of the chemical elements in protoplanetary nebula. Meteoritika 32:7–24 (in Russian)
Levin BYu, Simonenko AN (1977) Unresolved problems in origin of meteorites. Meteoritika 36:3–22 (in Russian)
MacPherson GD, Wark DA, Armstrong JT (1988) Primitive material surviving in chondrites: refractory inclusions. In: Kerridge JF, Matthews MS (eds) Meteorites and the early solar system. University of Arizona Press, Tucson, pp 746–807
Mason B (1967) Extraterrestrial mineralogy. Am Mineral 52:307–325
Mason B (1972) The mineralogy of meteorites. Meteoritics 7:309–326
McSween HY (1987) Meteorites and their parent planets. Cambridge University Press, Cambridge
Meyer BS, Waver TA, Woosley SE (1995) Isotope source table for a $25M_{\odot}$ supernova. Meteoritics 30:325–334
Minster JF, Allegre CJ (1976) ^{87}Rb-^{87}Sr history of Norton County enstatite achondrite. Earth Planet Sci Lett 32:191–198
Ott U (1993) Interstellar grains in meteorites. Nature 364:25–33
Petaev MI (1988) List of meteorite minerals. Meteoritika 47:156–166 (in Russian)
Schultz L, Signer P (1977) Noble gases in the St. Mesmin chondrite: implications to the irradiation history of a brecciated meyeorite. Earth Planet Sci Lett 36:363–371

Schulze H, Bischoff A, Palme H, Spettel B, Dreibus G, Otto J (1994) Mineralogy and chemistry of Rumuruti: the first meteorite fall of the new R chondrite group. Meteoritics 29:275–286

Sears DWG, Shaoiong H, Benoit PH (1995) Chondrule formation, metamorphism, brecciation, an important new primary chondrule group, and the classification of chondrules. Earth Planet Sci Lett 131:27–39

Srinivasan G, Ulyanov AA, Goswami JN (1994) ^{41}Ca in the early solar system. Astrophys J Lett 431:L67–L70

Taylor S, Brownlee DE (1991) Cosmic spherules in the geologic record. Meteoritics 26:203–211

Tshermak G (1885) Die mikroskopische Beschaffenheit der Meteoriten. Stuttgart. (Facsimile reprint, with English translation in Smithson Contrib Astrophys 1964, 4:239 p)

Ulyanov AA (1991) The meteorite minerals. In: 14th Brown-Vernadsky Microsymposium on Comparative Planetology, Moscow, 20 pp

Van Schmus WR, Wood JA (1967) A chemical-petrologic classification for the chondritic meteorites. Geochim Cosmochim Acta 31:747–765

Vdovykin GP (1967) Carbonaceous matter in meteorites. Moscow, Nauka, 269 pp (in Russian)

Vinogradov AP (1971) High-temperature protoplanetary processes. Geohimiya 11:1283–1296 (in Russian)

Wark DA, Lovering JF (1977) Marker events in the early evolution of the solar system: evidence from rims on Ca-Al-rich inclusions in carbonaceous chondrites. Proc 8th Lunar Sci Conf 1:95–112 Pergamon Press, Oxford

Wasserburg GJ (1985) Short-lived nucli in the early solar system. In: Black DC, Matthews MS (eds) Protostar and planets II. University of Arizona Press, Tucson, pp 703–773

Wasserburg GJ, Burnett DS (1978) The status of isotopic age determinations on iron and stone meteorites. Proc Symp Meteorite Research, Dordrecht, pp 467–479

Wasson JT (1985) Meteorites. Their record of early solar system history. WH Freeman, New York

Weisberg MK, Prinz M, Kojima H, Yanai K, Clayton RN, Mayeda TK (1991) The Carlisle Lakes-type chondrites: a new grouplet with high Δ^{18}O and evidence for nebular oxidation. Geochim Cosmochim Acta 55:2657–2669

Wood JA (1971) Meteorites and origin of the solar system. Moscow, Mir, 172 pp (in Russian)

Wood JA (1988) Chondritic meteorites and the solar nebula. Annu Rev Earth Planet Sci 16:53–72

Yaroshevsky AA, Ulyanov AA (1994) Catalogue of meteorite minerals. Meteor Conf 22: 91–92 (in Russian)

Yavnel' AA (1973) Classification of meteorites and its role in the problem of the origin of meteorites. Meteoritika 32:25–36 (in Russian)

Yates PD, Arden JW, Wright IP, Pillinger CT, Hutchison R (1992) A search for pre-solar material within an acid-resistant residue of Greenland cryoconite. Meteoritics 27: 309–310

Yudin IA, Kolomensky BD (1987) Mineralogy of meteorites. Sverdlovsk, Ural Sci Centre USSR Acad Sci, 200 pp (in Russian)

Zinner E (1995) Astronomy by mass spectrometry: interstellar grains in meteorite. Meteoritics 29:555

Zinner E, Amari S, Ravaglio C, Gallino R, Busso M, Woosley S (1995) The isotopic composition of interstellar graphite from the Murchison meteorite: evidence for supernova mixing. Lunar Planet Sci 26:1561–1562

1.9 Irradiation Effects on the Lunar Solids and Meteorites: Solar Wind, Solar Flares, and Galactic Cosmic Ray Records in the Lunar Minerals; Ion Implantation

L. L. KASHKAROV

Cosmic materials such as interplanetary dust particles, micrometeorites, meteorites, and the regolith matter of the Moon and asteroids constantly undergo irradiation by cosmic ray particles. Depending on the flux value, composition, energy spectrum, spatial variation, and angular distribution of the interplanetary charged particles in the inner Solar System, there are four basic constituents of the particle irradiation: solar wind (SW), suprathermal ions (STI), solar flares (SF), and galactic cosmic rays (GCR).

Fundamental components in cosmic radiation are protons (hydrogen nuclei, ~90%) and α-particles (nuclei of helium ~7%). The iron-group nuclei ($23 < Z < 28$) account for $\sim 10^{-3}$% of the total cosmic particle flux only. These three groups of particles are the most important from the point of view of their interaction with exposed material that gives specific quantitatively measured radiation effects.

In total, irradiation effects are the results of the energy loss process (ionization, nuclear excitation, nuclear spallation reactions, etc.) by the charged particles during their penetration through material under exposure; the depth of these effects is due to a particle kinetic energy (Fig. 18). The differential energy spectrum for the total Solar System charged particle flux is shown in Fig. 19.

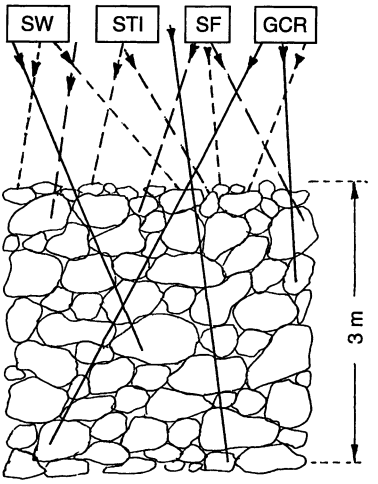

Fig. 18. Schematic sketch through the surface layer of the lunar regolith or the stone meteorite breccia illustrating the depth penetrating for the SW, STI, SF and GCR charged particles

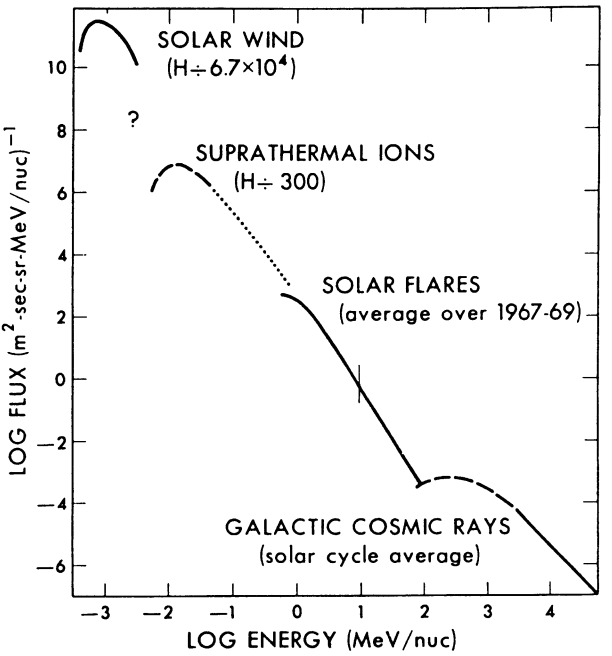

Fig. 19. Average present-day energy spectrum of the iron group nuclei and protons (H-nuclei) in the interplanetary space

The SW-particles with E~1 keV are very easily absorbed in the very thin (up to ~0.1 μm) surface layer of crystals. Thus, the radiation effects induced by SW-ions can be preciseley determined and measured only in the case of the thin-crushed micron-sized dust grains and microcrystal material under exposure. These effects are: (1) very high concentrations of solar-type rare gases (^{4}He, ^{20}Ne, ^{38}Ar, etc.) implanted in the exposed material, and (2) a superficial layer of amorphous coatings on the crystalline grains, whose thickness is about 0.05 nm.

The penetration depth in crystals for the STI with kinetic energy E ~ (0.01–0.1) MeV/nucleon is up to ~1 μm. As the result of stopping such intense STI flux in the thin surface layer of crystals and the SW-ions, the implantation of solar-type rare gases the formation of deeper amorphous layers are observed. In addition, the following STI irradiation effects were identified. With the help of high-voltage electron microscopy, in the micron-sized crystal grains nonetched latent nuclear particle tracks were observed – the linear trails of radiation-damaged material with a diameter of ~100 Å and track-density values (number of tracks measured on square unity of the search crystal surface) equal to 10^{10}–10^{12} track/cm^2. Upon heating (thermal annealing), these tracks act as nucleation sites and are transformed into track crystallites.

One of the very important irradiation effects of iron metal blebs accumulation in the lunar soils can be considered. The production of the iron metal

occurs in a complex process, including: (1) implantation of SW and STI hydrogen in soil microcrystals; (2) micrometeorite impact events; (3) production in the small fuse volumes of the glass phase; and (4) near-instantaneous reduction of Fe^{2+} in the melt material. So-called agglutinated glasses containing iron metal are widespread in lunar soils. The ratio of extremely fine-grained iron metal particles (<30 nm) to total iron oxide (I_s/FeO) is an accepted measure of the soil's "maturity" – the characteristic of their residence times on the lunar surface. The estimated effective times or the surface exposure ages for lunar regolith samples generally vary from 100 to 10000 times longer than for chondrite breccias.

The SF-charged particles, due to their higher kinetic energy in interaction with the silicate materials, penetrate in the material to a depth of up to some millimeters. However, in comparison with SW and STI particles, the SF have an essentially lesser degree of intensity and correspondly higher exposure times on the regolith surface of the cosmic objects are needed to obtain quantitatively measured radiation effects. The main radiation effects from SF particles consist of: (1) the formation of tracks from the iron-group nuclei characterized by specific track-density depth gradient inside the first 100–200-μm layer from the individual crystal surface, with the track-density values from 10^6–10^9 track/cm^2 interval; (2) disordered crystal structure up to the amorphous state, analogous to a metamictization process under high-fluency α-irradiation in zircons and other minerals with high U and Th concentration.

The GCR high energy p- and α-particles (E > 100 MeV/nucleon) give rise to a number of spallation nuclear reactions, for example: $^{26}Mg(p,n)^{26}Al$, $^{25}Mg(p,\alpha)^{22}Na$, etc. The depth of penetration in silicate matter of protons with E > 1000 MeV is equal to 300–400 g/cm^2, but the integral flux in these depths is strongly decreased. Thus, the products of p-induced nuclear reactions can be measured in the lunar regolith soil at different depths, but the total output of this radiation effect is decreased from the upper several centimeters down to some meters by ~100 times. Besides primary p-and α-particles in the nuclear interactions, a great number of secondary nuclear-active (neutrons, π-mesons, etc.) and X- and γ-ray radiation are generated. Under the influence of these secondary particles in matter, different nuclear reactions occur, one of which (ca. some MeV energy) is the formation of recoil nuclei, as a result of which process a great number of dislocations in the crystalline lattice are seen.

Chiefly under X- and γ-ray radiation in silicate crystals, the process of thermoluminescence storage occurs.

Neutrons of moderate energy give rise to fission of heavy nuclei (Th, U), and then, by thermalized (E > 0.01 eV) neutrons with high probability, fission of ^{235}U isotope nuclei occurs.

At the end of the total path of the GCR iron-group nuclei in silicate crystals tracks are formed with a length 10–20 μm, and track-density values 10^5–10^7 track/cm^2.

References

Allen CC, Morris RV, Lauer HV Jr, McKay DS (1993) Microscopic iron metal on glass and minerals – a tool for studying regolith maturity. Icarus 104:291–300
Crabb J, Schultz L (1981) cosmic ray exposure ages of ordinary chondrites and their significance for parent body stratigraphy. Geochim Cosmochim Acta 45:2151–2160
Durrani SA, Bull RK (1987) Solid State nuclear track detection principles. Pergamon Press, Harwell, UK
Fleischer RL (1981) Nuclear track production in solids. In: Progress in materials science. Chalmers Anniversary Volume. Pergamon Press, New York, pp 97–123
Hartmann WK (1983) Moons and planets. Wadsworth Publishing, Belmont, California
Housen KR, Wilkening LL (1982) Regoliths on small bodies in the solar system. Annu Rev Earth Planet Sci 10:355–376
Kashkarov LL (1988) High-energy cosmic ray VH-nuclei in the early solar system. Izv Acad Nauk USSR Ser Phys 52:2321–2324
Kashkarov LL (1990) Low-energy VH-nuclei cosmic ray tracks in meteorites. In: Int Worksh on solid state track detectors and their applications. Dubna, Russia, pp 87–91
Kashkarov LL (1995) VH-nuclei cosmic-ray tracks in chondrites as indicators for radiation-thermal history of the meteorite matter at the early stage of Solar system primary body formation. Radiat Measurements 25:311–314
Kashkarov LL, Genaeva LI, Kalinia GV, Lavrukhina AK (1988) Irradiation effects for the ordinary chondrites in the early stage of the Solar system body formation. Meteoritika 47:113–122
McSween HY Jr (1987) Meteroites and their parent planets. Cambridge University Press, New York
Morris RV (1980) Origins and size distribution of metallic iron particles in the lunar regolith. Proc Lunar Planet Sci Conf 11th:1697–1712
Perron C, Naury M (1986) Very heavy ion track etching in olivine. Nucl Tracks 11:73–80
Price PB (1982) Applications of nuclear track-recording solids to high-energy phenomena. Philos Mag 45:331–346
Wasson JT (1985) Meteroites, their record of early solar system history. WH Freeman, New York

1.10 Mineralogy of Astroblems – Terrestrial Impact Craters

1.10.1 Introduction

A. Deutsch and F. Langenhorst

Hypervelocity collision of extraterrestrial projectiles with the Earth (impact process) has played a crucial role in the evolution of the atmosphere and life, and still represents a certain danger for man. The importance of terrestrial cratering was acknowledged by the geoscience community only in 1980, when the

Advanced Mineralogy, Volume 3
Mineral Matter in Space, Mantle, Ocean Floor, Biosphere, Environmental Management, and Jewelry (ed. by A. S. Marfunin)

impact of a roughly 10 km projectile was proposed as the cause for the long-known mass extinction at the Cretaceous-Tertiary (K/T) boundary. From that time research on all aspects of cratering started to flourish. The discovery of the 65 Ma Chicxulub impact structure, Mexico, as source crater of the ejecta layer at the K/T boundary, and the impact of the comet Shoemaker-Levi 9 on Jupiter in summer 1994 finally convinced a broader audience of the fundamental importance of hypervelocity impact as a geological process.

This chapter aims to review current knowledge of minerals which occur either in direct spatial relation to terrestrial impact structures or as constituents of distant ejecta deposits. In addition, a few specific, well-investigated structures of proved or suggested impact origin will be discussed in the light of recent mineralogical and geochemical research. As a preface to these topics, concise sections cover basic aspects of shock processes, cratering, and the general geology of impact craters and ejecta layers. For a comprehensive introduction to impact processes with particular emphasis on physical conditions, we refer the reader to Melosh (1989). More special aspects, such as geology, geophysical properties, and dating of terrestrial impact structures, mineralogical and geological shock effects, are reviewed by, e.g., Masaitis et al. (1980), Grieve (1991), Pilkington and Grieve (1992), Deutsch and Schärer (1994), Stöffler and Langenhorst (1994), Grieve and Shoemaker (1994), and Grieve et al. (1996).

Beyond phenomenological descriptions of minerals produced in or affected by impact process, this chapter focuses on the characteristics of these minerals on the submicroscopic scale, as well as on the processes and physical conditions which cause shock effects. This basic information is necessary to combine observational data at natural impact craters and shock experiments with theoretically derived models of cratering mechanics. Instructive examples are given on the basis of the most detailed investigated minerals in the environment of impact craters and ejecta layers. The important contribution of modern geochemical and mineralogical research to a better understanding of impact processes will be shown in the context of the impact structures reviewed, Nördlinger Ries, Sudbury, Vredefort, and Popigai.

1.10.2 Cratering and Shock Metamorphism

A. Deutsch and F. Langenhorst

Cratering and Shock Physics

Impact craters on Earth are produced by the hypervelocity impact of asteroids and comets at velocities between 11 and 72 km s^{-1}, with a mean relative collision velocity of around 20 km s^{-1}. Crater formation is subdivided into three subsequent but overlapping stages: (1) Contact of the projectile with the target

Advanced Mineralogy, Volume 3
Mineral Matter in Space, Mantle, Ocean Floor, Biosphere,
Environmental Management, and Jewelry (ed. by A. S. Marfunin)

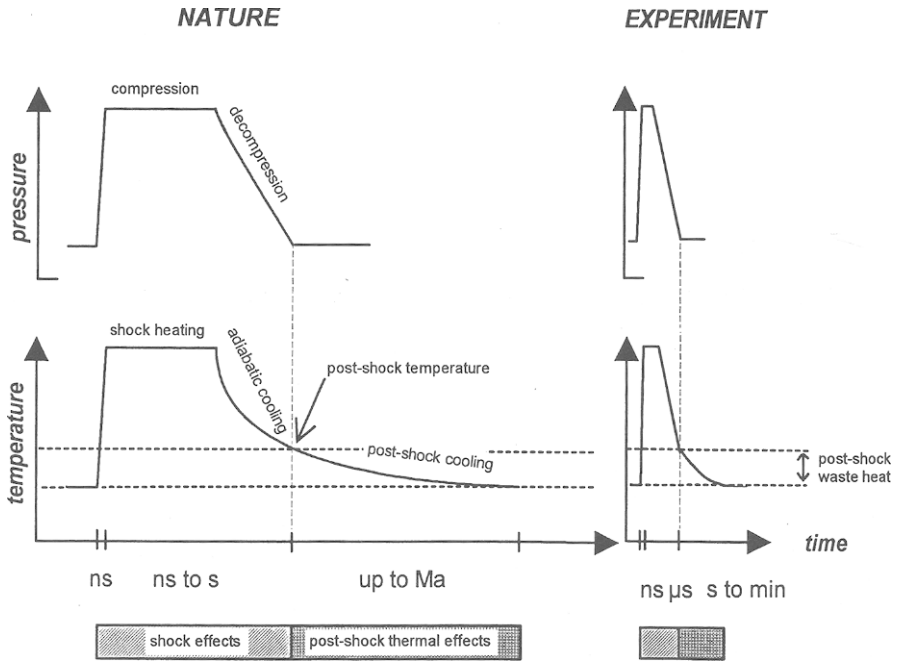

Fig. 20. Schematic pressure and temperature vs. time profiles for a shock event in nature (*left*) and experiment (*right*). Note change in time scale between *nature* and *experiment*. Shock and post-shock thermal effects are related to different stages of the process

surface, followed by compression and vaporization of the projectile and parts of the target, (2) excavation, and (3) modification of the crater. During the initial contact of the projectile with the surface, impact-melted target material is ejected as a primary jet at supersonic speed at low angles; this material forms tektites. Strong compression waves (shock waves) propagate with supersonic velocity into both projectile and target as most of the impactor's kinetic energy is transferred to the target. Shock waves result in drastic changes in the physical parameters of the affected material, which are idealized as discontinuities in pressure, temperature, density, and internal energy. This is shown schematically in Fig. 20. An even faster travelling rarefraction wave follows, resulting in decompression of the compressed material. In contrast to "normal" compression waves, shock waves are accompanied by a high-speed material transport behind the shock front giving rise to particle motion and ejection. As a result of the nonisentropic nature of shock compression, residual heat remains in the shocked material after pressure release (post-shock waste heat in Fig. 20). The projectile and parts of the target rocks are vaporized at pressures, which may reach several 100 GPa (Gigapascal), and temperatures of a few 10^4 Kelvin, forming an expanding vapor plume above the growing crater. In the target, the hemispherical shock wave and the rarefraction wave lead to shock metamor-

phism, material excavation, and ejection, until a bowl-shaped "transient" crater is formed within seconds. Due to gravitational forces, the transient cavity collapses rapidly during the modification stage of the crater, leading to turbulent mixing of shocked and unshocked materials, and slumping of material along the crater walls.

The cratering process results in different, characteristic geological formations. Figure 21 illustrates the distribution of these impact formations in and around a complex crater formed in a crystalline target. About 80 vol.% of the target affected by the shock wave consists of undisplaced or slightly rotated target rocks underneath and around the crater ([par-]authochtonous or authigenic breccias). The remaining 20% is formed by displaced, allochthonous (allogenic) breccias showing various degrees of shock metamorphic overprint, and impact melt rocks, with the relative proportion of melt rocks increasing with crater size. Clastic matrix breccias with melt particles (suevitic breccias) compose up to 10% of the displaced masses, but the dominant material are breccias devoid of impact melt.

Shock Metamorphism

Shock metamorphism is a fundamental and common process in the Solar System. It is caused by the short pulse of high dynamic pressure, which occurs exclusively in the context of natural impact events, nuclear or chemical explosions, or shock experiments. In shock metamorphism, pressure, temperature, as well as strain and quench rates, exceed by orders of magnitude the conditions existing during endogenic processes. This fundamental difference is illustrated in Fig. 22 for pressure and temperature. Typical strain rates acting during shock compression range from 10^6 to 10^9 s^{-1}, roughly 20 orders of magnitude higher than typical strain rates of endogenic metamorphism. However, these exceptional physical conditions prevail at the maximum for a few seconds only, even in the case of very large impact events (Fig. 20). The extreme and ultra-short shock stress causes unique physical and chemical disequilibrium changes in minerals and rocks. Rocks are the subject of textural changes, ranging from brecciation, through melting, to vaporization, i.e., ceasing of target and projectile material as a physical entity. Minerals show a variety of microscopic to sub-microscopic changes, e.g., formation of lattice defects or high-pressure polymorphs and dissociation, the so-called (residual) shock effects. These different categories of change and formation in rocks and minerals have been traditionally summarized as shock or impact metamorphism, although these terms are not synonymous in a strict sense. The latter term has to be preferred because several phenomena identified in the context of impact craters and ejecta layers are not directly related to shock compression and decompression. Impact metamorphism covers, in addition, a variety of processes confined by a geological "normal" p-T-time space. For example, post-shock cooling, differentiation, and crystallization of a large impact melt pool resemble the formation of a suite of

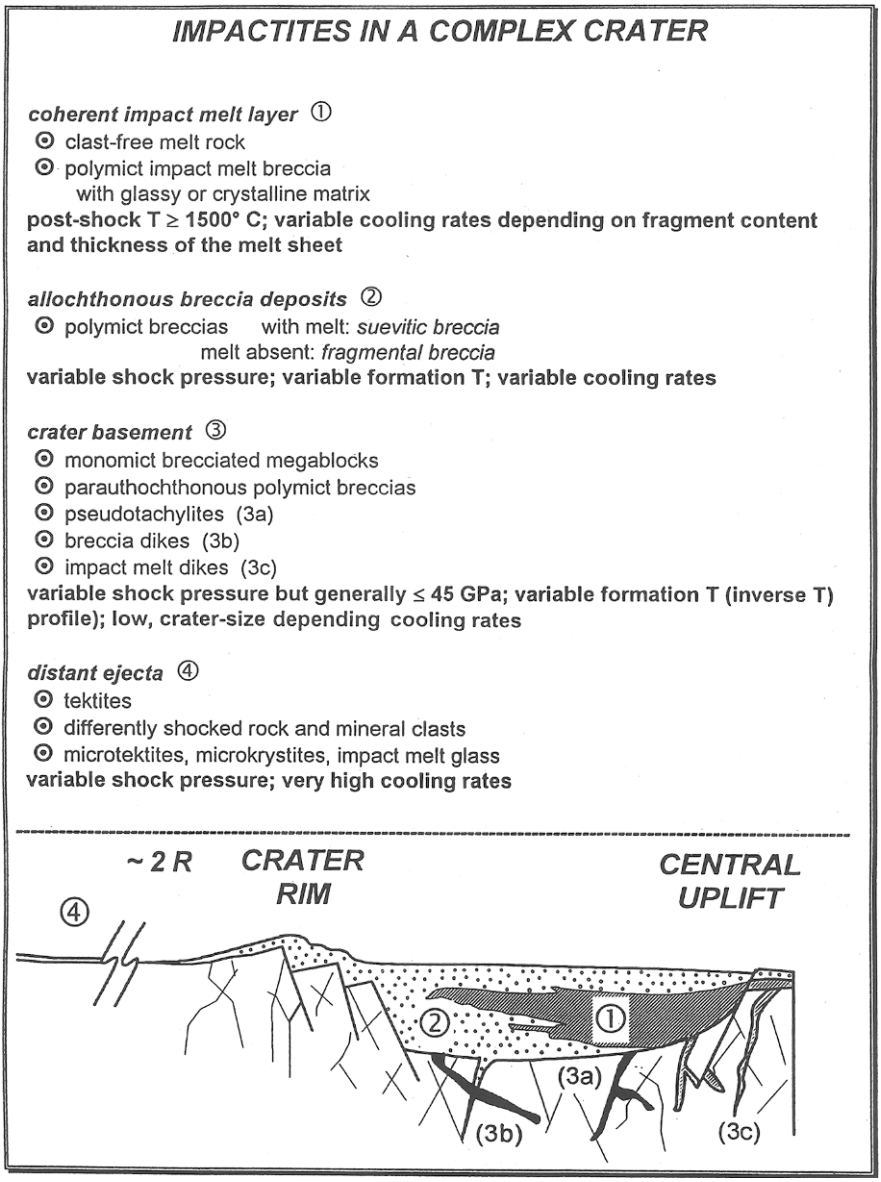

Fig. 21. Schematic cross-section of a complex crater with a central uplift showing locations of the different impact formations, arranged according to their variable pressure-temperature history. *R* Radius of the final (modified) crater. Not to scale

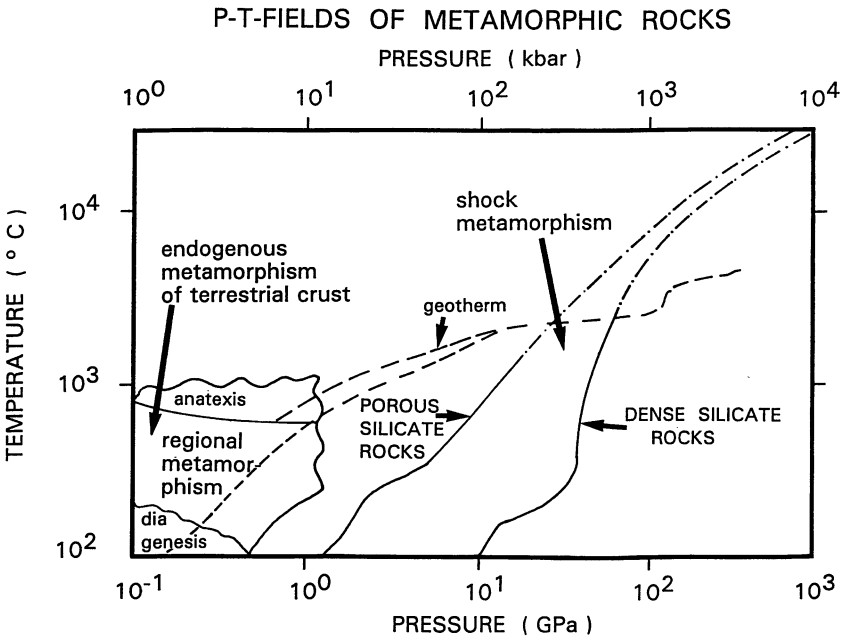

Fig. 22. Schematic pressure vs. temperature diagram, delineating fields for endogenic metamorphism of the terrestrial crust and for shock metamorphism

endogenic magmatic rocks, but cannot be considered as metamorphic processes. Rocks being affected by impact metamorphism are summarized under the collective term impactite.

In this chapter, a clear distinction is drawn between primary shock effects related to shock compression and pressure release (shock metamorphism in the strict sense) and post-shock thermal effects, which occur after decompression (Fig. 20). We will concentrate exclusively on such shock and post-shock phenomena that are characteristic of impact. The current interpretation and understanding of shock effects in minerals relies mainly on careful transmission electron microscope (TEM) studies as well as on systematic shock experiments. A recent example of the use and combination of both techniques is given in Langenhorst and Deutsch (1994) and Langenhorst (1994).

Shock and Cratering Experiments

Shock recovery and cratering experiments have yielded important findings for the understanding of impact processes, including, for example, the calibration of threshold pressures for particular shock features or ejecta mechanisms (e.g., Boslough 1991). The two most commonly used set-ups for the acceleration of

projectiles in experiments are light-gas guns (compressed air, one- and two-stage argon or helium devices) and high-explosive devices.

Recently, powerful lasers and electric discharge techniques have gained in importance, and shock pressures in excess of 100 GPa can be reached with coherent waves. In addition, investigations at nuclear test-sites have resulted in significant scientific contributions to cratering research.

Distinct differences between shock waves generated in the laboratory compared to nature have to be considered in interpreting experimental data. For example, and as illustrated in Fig. 20, the duration of the peak pressure plateau lasts for orders of magnitude longer in natural impacts than in experiments. This shorter pressure pulse is only a consequence of the small thickness of projectiles in all types of experiments. Other differences originate from the geometry of the shock waves, the energy density at the projectile's stagnation point compared to chemical or nuclear charges, and the loading path to reach the peak pressure. Moreover, shock and post-shock temperatures are significantly lowered compared to the natural case if techniques with multiple shock reverberations are used. Major advantages of shock recovery experiments, which were pioneered by Milton and DeCarli (1959), are (1) the precise control of physical and chemical properties of the specimen, (2) direct measurements of physical parameters and their change during shock compression by sophisticated VISAR methods (*V*elocity *I*nterferometer *S*ystem for *A*ny *R*eflector), and (3) separation of effects which originate directly during shock compression from those, caused by post-shock annealing after pressure release. The latter point makes recovery experiments indispensable in unraveling the original nature of shock effects. Numerous investigations have shown that, despite the above-named caveats, minerals display identical shock features in both experiment and nature down to the atomic scale as long as they are related only to the magnitude of the shock pressure. Therefore, shock and cratering experiments are established as important tools to investigate the physics of impact metamorphism and cratering, and to calibrate shock effects in minerals.

1.10.3 Characteristics of Terrestrial Impact Structures

A. Deutsch and F. Langenhorst

Recognition

Distinctive evidence for confirming the impact origin of a geological structure is established by the occurrence of (1) residual shock effects in minerals and/or certain high-pressure polymorphs, (2) shatter cones, and, in special cases, (3) projectile remnants adjacent to the crater (Small Meteorite Craters, p 86). Second-order diagnostic tools are (4) breccia sequences and breccia dikes,

Advanced Mineralogy, Volume 3
Mineral Matter in Space, Mantle, Ocean Floor, Biosphere,
Environmental Management, and Jewelry (ed. by A. S. Marfunin)

including melt bodies with rock and mineral fragments and pseudotachylites (frictional melt rocks), (5) circular geophysical anomalies, (6) topographic features imaged by aerial photographs or remote sensing techniques, (7) overturned stratigraphy in the breccias of the ejecta deposits, and (8) geochemical signatures, such as enhancement of certain siderophile elements (e.g., Ni, Co, Cr, and PGEs), or isotope ratios, for example, a low $^{187}Os/^{188}Os$ ratio. (9) Exotic chemical compounds such as fullerenes have been detected only in the context of the Sudbury impact structure, Ontario, Canada, and in K/T ejecta deposits; their diagnostic value is unknown so far. None of the features listed under (4) to (8), however, provides alone ultimate proof for an impact origin of a geological structure or a distinct layer embedded in a sedimentary sequence. Criteria for recognizing deeply eroded impact structures have yet to be developed.

Temporal, Spatial, and Size Distribution of Impact Craters

By the end of 1996, 156 terrestrial impact structures were known, ranging in diameter (D) from 15 m (Haviland, Kansas, USA) to about 350 km; the oldest structures have an age of about 2 Ga (billion years), the youngest were formed in historical times: Kaalijärvi, Estonia, for example, is dated at about 4000 B.C. A crater list containing information on size, age, and projectile type (if known) was published by Grieve and Shoemaker (1994). R.A.F. Grieve at the Canadian Geological Survey, Ottawa, regularly presents an updated report of confirmed craters, including the newly discovered impact structures – at present, at a rate of up to five craters per year (http://gdcinfo.agg.emr.ca/crater/world_craters.html).

The craters on land show concentrations in North America (especially Canada), Australia, parts of the former Soviet Union, and northern Europe. This distribution reflects active crater-search programs in some countries and the fact that these regions are old cratonic areas with small time-integrated erosion rates, long exposed to the cosmic bombardment, and, therefore, with a larger cumulative number of craters. Other stable shields, e.g., in Africa, S. America, or China, have not yet been searched systematically for impact structures, but recent discoveries indicate the presence of a significant number of additional craters in these areas as well. On land, terrestrial craters show varying stages of preservation and exposure, ranging from deeply eroded, e.g., Vredefort, South Africa, to examples with well-preserved ejecta deposits outside the rim of the final crater, e.g., Nördlinger Ries, Germany. About 30% of the known crater population are completely buried by sedimentary rocks, and, in rare cases, tectonism resulted in re-shaping of the circular form as exemplified by Beaverhead, Montana, USA, or the Sudbury Structure, Ontario, Canada. In general, however, impact structures are circular, except that projectiles with a very low impact angle produce extended scars, such as the Spider Structure, W.A., Australia. If the size-frequency distribution of terrestrial craters is com-

pared with that on other planetary bodies, a distinct deficiency for craters with $D \leq 20$ km is obvious due to preferred removal of smaller craters by endogenic and exogenic forces.

About 60% of the known terrestrial craters are younger than 200 Ma (million years), reflecting again the highly dynamic nature of the crust. For about one third of the total crater population, isotopic ages are available, and for about 30 craters, the relative precision on the age is better than 10%. However, even for some of these, the age significance is under dispute. Other methods of dating are biostratigraphy in post-crater sediments and paleomagnetic methods; under favorable conditions, both methods can yield an age with high precision and accuracy. Age data and size distribution indicate quite clearly that our knowledge of the terrestrial cratering record is strongly biased towards younger and larger craters. This was taken into account in an estimation of the recent terrestrial cratering rate, which is $5.6 \pm 2.8 \times 10^{-15}$ km^{-2}a^{-1}, using only craters with $D \geq 20$ km and younger than 120 Ma (Grieve and Shoemaker 1994). Despite the inherent bias in the cratering record, a periodicity in cratering during Phanerozoic times with a period of 26–33 Ma has been claimed. The insufficient number of high-quality crater ages limits any analysis of whether this assumption is statistically valid (see discussion in Grieve and Shoemaker 1994).

The morphology of relatively well-preserved impact craters on Earth compares, in principle, well with crater forms on other planetary bodies ranging with increasing diameter from simple, bowl-shaped depressions, to complex craters with a central peak, a peak-ring, a ring basin, to multi-ring basins. The relations of the morphometric parameters and their definition have been reviewed in detail by Grieve (1987). Differences in the morphometric parameters to, for example, the lunar data, are due to gravitational effects, which influence crater modification and erosion. In the following, simple and complex craters are characterized, and special cases of terrestrial cratering are outlined.

Historic Collisions

Tunguska. The great fireball near the Podkamennaya-Tunguska river, Siberia, on the morning of June 30, 1908, is the only historically well-documented encounter of a high-energetic extraterrestrial body with planet Earth: The body, probably a 50-m fragment of a stony meteoroid, did not strike the surface, but disintegrated at an estimated altitude of about 8.5 km, causing atmospheric over-pressure pulses, and, by coupling to the ground, seismic waves, which both were recorded as far away as Greenwich, Jena, or Tiflis. Analysis of barograms, seismic records, and scaling from nuclear airburst yields an estimated kinetic energy of 12 up to 48 megatons TNT equivalent ($\approx 10^{17}$ J) for the Tunguska bolide. The event resulted in devastation of more than 2000 km^2 of Siberian taiga. Despite intense research, only minute traces of cosmic material in the form of glass and magnetite spheres have been recovered on the ground. Peat

at the impact site contains a weak Ir signal (17.2 pg g^{-1}), whereas, Crête Site B ice core, drilled in the ice sheet at Central Greenland, lacks an Ir anomaly related to the Tunguska event (Rasmussen et al. 1995).

Besides Tunguska, two other collisional events occurred in this century. In February 1947, a bolide with an estimated kinetic energy of 1.7 kt TNT equivalent ($\approx 10^{14}$ J) broke up at an altitude of about 6 km over Shikote-Aline, Siberia, yielding more than 100 craters with a diameter ranging from 0.5 up to 26.5 m. More than 23 tons of the iron meteorite fragments have been recovered. A similar, although much smaller and about 4 ka (10^3 years) old meteorite-strewn field is known in South Australia (the Henbury craters). In March 1965, a bright fireball was observed over southern British Columbia, Canada, due to the passage of an object with an estimated kinetic energy of 20 ktTNT equivalent. Near Revelstoke, tiny fragments of a carbonaceous chondrite with a total mass of 1 g were discovered and, in addition, airborne collectors over the United States gathered a large number of silicate glass and magnetite spherules.

Simple Impact Craters

The basic form of a simple crater is a shallow bowl surrounded by a structurally uplifted rim. Beneath the floor of this so-called apparent crater, a lens of allochthonous impact breccias lies on top of the brecciated, authochthonous crater basement. The interface between breccia lens and authochthonous rocks defines the true crater, which shows a roughly parabolic cross-section. The typical depth/diameter ratio of the true crater is 1 : 3. Several simple craters have been investigated in great detail, using geological and geophysical exploration techniques as well as shallow and deep drilling. The most outstanding examples are the 49.7 ka Barringer (Meteor) crater, Arizona, USA, the 450 Ma Brent crater, Ontario, Canada, and the 455 Ma Kärdla crater, Estonia.

Barringer crater, with a diameter of 1.2 km, still displays morphological features nearly unchanged by erosional forces. The apparent crater is about 200 m deep. The rim uplifted about 50 m above the original ground surface, is covered by an overturned flap of ejecta material, which continues into the hummocky outer ejecta blanket. The exceptional stratigraphic control of the sedimentary target and the wealth of observational data allowed to constrain all parameters relevant for calculating impact conditions for the Barringer crater (Roddy et al. 1975). Brent with D = 3.8 km is the largest simple crater in a crystalline target (Grieve 1978). This crater owes its excellent preservation to a 260 m thick cover of post-impact sediments, which sealed the up to 630 m thick breccia lens. Brent has a thin basal zone of impact melt rocks directly overlying a parauthochtonous breccia of the brecciated crater floor. Mineralogical data form Brent have served to define the radial attenuation of shock pressure in simple craters. Kärdla, with D = 4 km, has a stratified target of Ordovician and Lower Cambrian sand- and siltstones on top of Proterozoic crystalline rocks

(Plado et al. 1996). More than 300 drill holes penetrated the breccia lens, the rim as well as the brecciated basement. Remnants of the ejecta occur in the sediments up to 50 km away from the crater rim. A very small central uplift indicates that Kärdla is close to the transition from simple to complex crater forms.

Small Meteorite Craters Formed by Iron Meteorites. Meteorite craters are considered a special group of prehistoric impact scars because – under favorable climatic conditions – remnants of the projectile are partly conserved. Under morphological aspects, however, this type of crater belongs to the simple bowl-shaped craters. The projectiles are high-density iron or stony-iron meteorites less than 150 m in diameter. They can penetrate the atmosphere, whereas, weaker stony bodies of similar dimension are disrupted by atmospheric break-up. The only known exception is the 100 ka Rio Cuarto cratering field, Argentina, where a low impact angle resulted in ricochet of the chondritic projectile, remnants of which have been recovered at the impact site. The largest meteorite crater is the 49.70±0.85 ka Barringer Crater. This age is based on different techniques, i.e. surface dating of boulders in the ejecta blanket using ^{10}Be and ^{26}Al exposure ages, ^{14}C-dating of organic material in rock varnish, and thermoluminescence dating of quartz in shocked sandstone (e.g., Nishiizumi et al. 1991; Phillips et al. 1991).

In the surroundings of meteorite craters, several types of impactor-related particles are recognized. They include ablation spherules produced during atmospheric entry of the projectile, shattered fragments of the meteorite itself and metal oxide fragments with meteoritic Fe/Ni ratios, glassy spherules composed of target and impactor material, and melted target rock particles with vesicular texture. Holohyaline spherules (impactite lapilli) at the Barringer Crater contain up 24 wt.% meteoritic material, and carry metal spherules with up to 90 wt.% Ni, interpreted as partially oxidized, molten meteoritic material (Kargel et al. 1996). At the Berringer Crater, geochemical properties of the projectile (Canyon Diablo IA iron meteorite, original diameter of the projectile 30 m) and target formations are well constrained, allowing a mass balance for several elements in minerals and rocks of the ejecta blanket. At the elliptical-shaped 310-ka Wolfe Creek crater, W.A., Australia (D = 300 m), remnants of the III AB iron projectile are altered to laminated shale balls consisting of Ni-serpentine and Ni-carbonate.

Complex Impact Structures

Transition from simple to complex craterform structures occurs on Earth at diameters above 2 km in sedimentary targets, and 4 km in crystalline targets. The most characteristic features of complex craters are (1) modified rim areas, and (2) uplifted areas expressed as central peak and/or topographic rings; moreover, complex impact structures are shallower than simple craters with respect to

their depth/diameter ratio. The presence of near-surface lithologies of the pre-impact target stratigraphy within the rim and annular trough indicates that the maximum radial excavation by the cratering flow field is restricted to half the distance of the final structural rim. The depth of excavation is on the order of 0.05 times the final rim diameter. The rim area itself, often displaying terrace-like morphology, consist of blocks faulted inwards towards the center of the structure. In complex impact structures, annular troughs and central basins are filled with allochthonous impact breccias; if crystalline rocks dominate among target lithologies, a coherent impact melt layer is present. Examples for complex impact structures are illustrated below.

Rocks in the central hump are uplifted from maximum depths on the order of one tenth of the diameter of the final crater rim. According to geomechanical models using hydrocodes, some overshooting may occur during formation of this central peak (Ivanov 1994). Good examples for this structural uplift are found at the 15 Ma Steinheim Basin, Germany (D = 3.8 km), which most probably represents a twin crater of the Nördlinger Ries, or at the about 175 Ma Puchez-Katunki, Russia (D = 80 km). The central uplift of this exceptionally well-preserved structure is drilled to a depth of 5374 km (Vorotilov deep borehole). Down to about 3 km it consist of 100 m sized megablocks. Impact metamorphic overprint in the central uplift decreases with depth and is apparently concentrated at interblock boundaries (Masaitis et al. 1995).

It is important to note that erosion may preferentially remove brecciated material, resulting in a significantly modified ore even inverse topographical expression of the final crater. An excellent example of this is the 142.5 Ma Gosses Bluff, WA, Australia, showing only a 6 km wide structural uplift as topographic relic in the center of the structure with an original diameter of 22 km. Erosional effects also reshaped the morphology of the 23 Ma Haughton Dome, N.W.T., Canada (D = 24 km), and of the 280 Ma Clearwater West crater, Quebec, Canada (D = 36 km). Both impact structures display prominent topographic rings, which are formed not by structurally uplifted material, but simply by the preservation of more erosion-resistant rocks.

Submarine Impact Structures

Although submarine craters cannot be considered as a distinct group with regard to size or age, they are a specific problem because of their small number. Only a few confirmed underwater craters are known: Montagnais located offshore Nova Scotia, Canada (50.5 Ma, D ≈ 45 km), Tvären, Sweden (455 Ma, D = 2 km), Mjølnir in the Barents Sea (Gudlaugsson 1993), north of Norway (Jurassic; D ≈ 40 km), and Chesapeake Bay offshore the Atlantic coast of Virginia, USA (≈ 35 Ma; D ≈ 90 km). Additionally, half the Chicxulub structure is buried offshore the Yucatan platform below thick post-impact sediments, and the Kara Sea, Russia, contains relics of a crater representing either a twin structure of the 71 Ma Kara crater, named Ust-Kara, or part of the Kara crater itself. A Late Plio-

cene impact is recorded in an about 300 000 km^2 area of the South Pacific (Eltanin Sea Mt.) by the occurrence of microtektites and an iridium anomaly in absyssal sediments, yet the small-sized projectile ($\varnothing \leq 0.5$ km) probably did not reach the ocean floor (≈ 5000 m) there (Margolis et al. 1991; Gersonde et al. 1997). The debris layer is conserved in sediment cores from the Bellinghausen Sea; so far, vesicular impact melt, glassy spherules and unmelted meteorite clasts have been recovered in the cored material. Craters on oceanic crust are unknown to date, reflecting not only the young mean age of the oceanic crust, but also our relatively poor knowledge of two thirds of the Earth's solid surface.

Projectile Identification

Larger impacting bodies penetrate the atmosphere and collide with cosmic velocities, yielding shock pressures in the MPa range and extremely high shock and post-shock temperatures. These extreme conditions cause melting and vaporization of both the projectile and the target. Recondensation and admixture of the projectile material to impactites in the crater, especially impact melt material, and to ejected impact glass, produce a geochemical signature, allowing, in principle, identification of the projectile type by analyzing platinum group elements (PGEs), nickel, cobalt, and chromium, as well as Re-Os isotope systematics (e.g., Evans et al. 1993; Koeberl and Shirey 1997). These trace elements, which are depleted to various degrees in the Earth's crust, occur in high abundances and with distinctive interelement ratios (like ruthenium/iridium or rhenium/iridium) in certain groups of meteorites. For example, Irons show a pronounced enrichment in rhodium, while all types of chondrites have a flat C1 normalized distribution pattern limiting the use of PGEs for fine classification. Achondrites are enriched in Cr compared to most terrestrial rocks; in contrast, other types of impactors, like iridium- and osmium-poor Stony-Irons, are chemically inconspicuous and will not leave traces in impact melt rocks. Using the characteristic meteoritic signature to identify the projectile type and evaluate the projectile's contribution to the geochemical composition of an impactite, the so-called meteoritic component, is hampered by two facts. Constraining the net amount of the meteoritic component requires subtraction of the indigenous component which is derived from the target rocks. If the target has a heterogeneous composition with presence of mafic to ultramafic rocks, a precise knowledge of the relative proportions of the different lithologies in the crater area is required to avoid overestimation of the indigenous component. The second impediment in projectile identification via PGEs results from the fact that fractionation of the siderophile elements can occur, either directly during the impact process or by post-impact alteration processes. Ir proved to be the most diagnostic element, while Re, for example, shows some mobility in weathered material.

Despite these complications, the projectile type has been identified for 27 larger impact craters (Grieve and Shoemaker 1994). In some cases, however,

specification relies on only a few elements, requiring reanalysis with more sophisticated methods. The analyzed impact melt rocks usually contain 1 wt.% projectile material, but knowledge of the three-dimensional distribution of the meteoritic component within an impact melt sheet is poor. PGE data indicate a uniquely high amount of 7.4 wt.% chondritic component in impact melt rocks of the 280 Ma East Clearwater structure, Quebec, Canada (Palme et al. 1979). This observation is explained by a low impact velocity (≤ 17 km s^{-1}). It is assumed that the metal component of the projectile was only melted but not vaporized, and directly incorporated down into the vaporized and melted target rocks. The principal reliability of PGE data for determining projectile contribution has gained enormous importance in constraining the general influx of extraterrestrial material, and, of even greater interest, in the search for distal ejecta layers.

1.10.4 Geological Formations in and around Impact Structures

A. Deutsch and F. Langenhorst

Based on their regular distribution, up to four different geological formations can be distinguished in and around an impact crater: (1) crater basement, (2) allochthonous breccia deposits, (3) coherent impact melt layer, and (4) distant ejecta. Distribution of these formations is shown in Fig. 21, giving a schematic cross-section through a complex impact structure with a central uplift. The geological formations are characterized by certain impact metamorphic features, which are discussed below; in part, these characteristics reflect the distinct post-shock thermal histories. The three main textural types of polymict impact breccias which occur as essential lithologies in the context of an impact structure and their characteristics are explained in Fig. 23. It is important to note that no general consensus about the terminology for imapctites has been reached yet, and local terms or names comprising both genetic and descriptive attributes are still in use. A straightforward rock classification, allowing identification of impactites in meteorites, the lunar collection, and terrestrial impact craters, is not available to date. A draft of a consistent nomenclature is currently being reviewed by the IUGS subcommission on the systematics of metamorphic rocks, study group for impactites (Stöffler and Grieve 1994).

Crater Basement

The crater basement consists of monomict brecciated megablocks and parauthochthonous and authochthonous (authigenic) breccias, which are either polymict or monomict, depending on the target stratigraphy. Dikes of fragmental breccias, pseudotachylites, and impact melt rocks transect the basement

Advanced Mineralogy, Volume 3
Mineral Matter in Space, Mantle, Ocean Floor, Biosphere,
Environmental Management, and Jewelry (ed. by A. S. Marfunin)

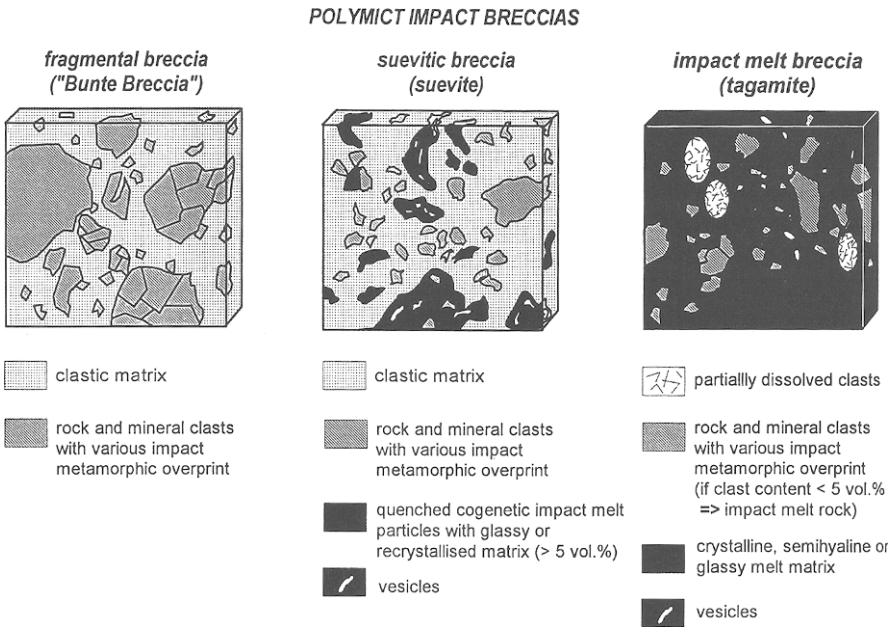

Fig. 23. Schematic drawing of the three main textural types of polymict impact breccias. The size of clasts and cogenetic melt particles (in suevitic breccias) may vary for orders of magnitudes. Rock fragments may display internal brecciation.

(Fig. 21); contact relationships, matrix type, and clast population suggest that the dike breccias originate during compression and decompression as well as in the crater's modification stage. Knowledge of this impact formation relies on research in deeply eroded craters or in the central uplift of complex structures as well as on drilling and geophysical measurements. Maximum shock pressures recorded in the crater basement are about 45 GPa; above this threshold, partial melting starts. Usually, shock features in quartz and feldspar are used for shock wave barometry. Isobars indicate a systematic decay of the maximum recorded shock pressure from the stagnation point of the projectile towards the crater rim and with depth, and trace the upwelling in the central mount, e.g. at Puchez-Katunki. The regular distribution of isobars has been used successfully to reconstruct the original dimension of now deeply eroded impact structures. Shatter cones corresponding to a shock pressure in the 4 ± 2 GPa range, are the diagnostic shock effects which occur radially most outwards from the crater center. There are good reasons to believe that the formation of shatter cones fades out at about 0.6 to 1 radii of the outer rim of the transient cavity. Shocked minerals are unknown from regions outside the rim of the transient cavity, where the rocks only show various kinds of brecciation.

Post-impact thermal history in the crater basement is determined by post-shock waste heat in rocks of this basement and annealing by the overlying

crater fill, which may comprise impact melt. A voluminous melt sheet can cause a reverse temperature gradient in the crater floor, and produce a thermal contact aureole in the footwall. In large impact structures, such as Sudbury, where the transient cavity reaches deep crustal levels, cooling rates in the basement also depend on the ambient geothermal situation. Cooling is, therefore, related to the crater size, and temperature decay is slow compared to all other impact formations. A special thermal situation is documented at some impact structures, e.g., at Puchez-Katunki, where shear heating due to differential movement of large blocks has produced zones of coptoblastolithes, i.e., impact metamorphosed rocks, which have undergone high-temperature solid state recrystallization (Masaitis and Mashchak 1996).

Allochthonous Breccia Deposits

Allochthonous breccia deposits occur in the crater fill as breccia lens, and, up to two to three crater radii away from the tectonic rim of an impact structure (Fig. 22), as part of the continuos ejecta blanket which can contain large amounts of local, unshocked surface material. Mineral and rock fragments in the polymict breccias display a wide range of impact metamorphic features; melt particles may be present (Fig. 23). The breccia lens is formed by material which remained inside the hemispherically growing transient crater, slumping back from the crater walls during the modification, and by fallback clasts of all size. Late fallback material from the vapor cloud, rich in glassy particles, may form a thin layer on top of these deposits. Ballistic sedimentation is the process forming the breccia deposits outside the crater: debris formed by the passage of the shock wave are ejected ballistically in an expanding ejecta curtain during crater growth at predominantly subsonic speed, followed by radially outward flow at the surface. This flow erodes the surface layer and incorporates significant amounts of local material. Part of the debris found outside the crater rim is laid down by a base surge, which is a gravity-driven density current descending from the expanding vapor cloud above the crater. The observed polymict nature of the breccia deposits is due to the complex material movement in both types of processes.

In allochthonous breccia formations, thermal equilibrium is reached quickly after deposition. Depending on the abundance of melt particles, the equilibrium temperature may exceed 600 °C in suevitic breccias. Observations at the Ries crater indicate that cooling of the about 400 m thick suevite layer to ambient conditions occurred on the order of months to a few hundred years. Hot gases and fluids, rising form deeper levels of the crater, result in more complex thermal histories of allochthonous breccias and can cause partial obliteration of shock effects.

Coherent Impact Melt Layers

The coherent impact melt layer ranges from clast-free melt rocks to polymict breccias with a melt matrix that contain shocked and unshocked rock and mineral fragments in varying abundance (Fig. 23). The melt matrix is holohyaline to holocrystalline, occasionally showing a coarse-grained igneous texture. Massive impact melt rocks are called tagamites after the Tagamy hills in the Popigai crater, Russia. Size and thickness of the coherent impact melt sheet is scaled with the crater dimension, and the relative amount of melt increases with the crater size (Cintala and Grieve 1994). Coherent melt layers are extremely rare to absent in craters with sedimentary target materials, especially when carbonates dominate. Melting on the whole rock scale is confined to a hemispherical zone shocked at pressures in excess of about 60 to 80 GPa. Partial melting is restricted to highly shocked material, which is engulfed by the impact melt, and to contact zones, where it may occur after deposition of the coherent melt layer in the crater. Time scales for cooling depend on fragment content and thickness of the melt layer, and are variable, with the center of the melt sheet remaining hot much longer than the clast-rich marginal facies. Good examples of coherent impact melt sheets exist in the 100 km sized 210 Ma Manicouagan structure, Quebec, Canada, where up to 230 m of the melt layer is preserved, at Popigai with an up to 600 m thick melt layer, and at Sudbury.

Independent of crater size and target material, unaltered impact melt rocks display common characteristics. Geochemically, the melt rocks duplicate the composition of target rock mixture, except in certain cases, when enhanced abundances of some siderophile elements and Cr occur due to projectile contamination. In coherent impact melt layers, most major and minor elements are well homogenized with respect to the precursor material. This characteristic homogenization is a corollary of material mixing during the turbulent, high-velocity flow of the melt within the expanding transient cavity. It can be estimated from the Manicouagan melt sheet that chemical homogeneity reaches at least over horizontal distances of tens of kilometers and vertical distances exceeding 200 m, although local irregularities exist (Floran et al. 1978). Commonly observed variations in alkali elements may be due to preferred assimilation of country rock material with a low melting point or to secondary processes, documented for a number of craters. Excess of calcium and, to a lesser degree, of magnesium may indicate a cover of carbonatic sediments in the target area at the time of the impact, which has now been eroded. Within a crater, the observed variation in REE abundances between different melt rock samples is less than that for the target lithologies, whose REE distribution patterns bracket those of the impactites. On the level of isotopes, complete homogenization is rarely reported. Variable initial Sr isotopic ratios are an important primary characteristic of coherent impact melt layers (Jahn et al. 1978), and the Rb-Sr data for whole rock samples define mixing lines or cluster in the field delimited by target lithologies. Samarium-neodymium isotope systematics seem to be determined by the presence of inherited refractory minerals – at

least at the kg scale of whole rock samples, and, hence, Nd model ages help to delimit precursor material of impact melt rocks. If sufficient geochemical and geological data are available, the relative proportions of target lithologies contributing to the impact melt rocks can be modeled as mixtures of particular basement lithologies by means of least-squares mixing programs. This has be done for several craters, and usually silica, aluminum, and iron yield the best fits. It should be noted, however, that hydrothermal processes initiated by, e.g., circulating fluids driven off crater basement lithologies by the hot overlying melt sheet, may obliterate some of the given clear geochemical features.

At small craters with limited impact melt layers, differentiation, if it occurs at all, is certainly restricted, due to the extreme sheet-like character of the melt body and the high viscosity of the clast-laden melt during crystallization. At Sudbury, however, the more than 2.5 km thick impact melt (so-called Sudbury Igneous Complex) differentiated like a classical endogenic magma (see below). So far, other examples for differentiated impact melt sheets are unknown from terrestrial impact structures.

Distant Ejecta

Distant ejecta comprise variably shocked mineral and rock fragments, high-pressure phases, impact melt glass, including tektites, as well as spherules of widely varying chemical and textural composition and morphology, amongst them so-called microkrystites, and exotic spinel crystals; the latter probably represent high-temperature condensates from the vapor plume. Distant ejecta material may be heavily contaminated by constituents of the impactor, resulting in enhanced abundances of siderophile elements (mostly PGEs). Exotic chemical components such as fullerenes and extraterrestrial amino acids (α-amino-isobutric acid, and racemic isovalin) have been reported only from the K/T boundary ejecta layer and are still a subject of discussion. Geochemical signals like sharp excursions in the stable isotope record may characterize marine sediments on top of distant ejecta deposits. However, these "anomalies" are secondary consequences of impact, and can only be related to the short- and long-term corollaries of a cratering event if unambiguous mineralogical evidence for impact metamorphism is documented (e.g., planar deformation features in quartz). Distant ejecta can occur up to thousands of kilometers away from the crater. The material, having suffered rapid quenching, is either ejected ballistically or suspended and transported by large-scale motions in the stratosphere.

Tektites (derived from $\tau\varepsilon\kappa\tau o\sigma$ = molten) are a subgroup of impact glasses characterized by their chemical homogeneity and an H_2O content below 0.02 wt.% (Koeberl 1994; Beran and Koeberl 1997). Compared to volcanic glasses of similar silica-rich composition, tektites are depleted in elements of different volatility (e.g., Cu, Ce, Sn, Pb), whereas, enrichments in Cr, Ni, and Co, as well as low $^{187}Os/^{188}Os$ isotope ratios, reflect incorporation of vaporized projectile material. Tektites may contain inclusions of lechatelierite (SiO_2

glass), coesite, relics of shocked minerals, and baddeleyite as decomposition product after zircon. The subgroup of Moung Nong-type tektites displays alternating light- and dark-colored layers and carries submicron-sized crystals of corund, zircon, rutile, and chromite. Tektites originate extremely early in a cratering event by impact melting of the uppermost target rock layer, followed by jet ejection of the melt at low angles with supersonic velocity. The up to several centimeters large objects often display spherical symmetry like teardrops or dumbbells due to quenching of rotating liquids during transport. The aerodynamically shaped flange-button Australites provide evidence for re-melting in the course of re-entering the atmosphere. Moung-Nong-type tektites have a blocky appearance and the mass of single objects may exceed 24 kg. Geochemical characteristics of tektites, e.g., ^{10}Be abundances, reflect the origin from near-surface material, and their Sr-Nd isotope systematics have been used successfully in some cases to delimit the source region or to identify the precursor lithologies (Blum et al. 1992).

Tektites, which are ideal objects for Ar-Ar dating, occur in four major strewn fields (e.g., Koeberl 1994). These are the Australasian, the Ivory Coast, the Central European (= Moldavites), and the North American strewn fields. Isolated discoveries are, e.g., the 24 Ma Urengonites in Siberia (Deutsch et al. 1997), tektite-like objects near the Frasnien-Fammenian boundary in Belgium and China, and microtektites with a diameter of generally less than 1 mm in deep-sea drill cores, for example, the ca. 35.5 Ma microtektites detected in Caribbean Sea cores close to the Eocene-Oligocene boundary. Impact melt glasses display shapes similar to tektites, but differ by a slightly higher H_2O content (0.02 to 0.06 wt.%) and more heterogeneous chemistries. This has been documented, e.g., for impact melt glass droplets at the K/T boundary covering a broad range from calcium to silica-rich compositions due to the incorporation of varying proportions of different sedimentary precursor rocks. Apparently, impact melt glasses originate from deeper levels of a growing impact crater than tektites.

The Creataceous-Tertiary boundary stands as uniquely documented example for the so far only known global occurrence of distant ejecta (Smit 1994). This may be due to the fact that the knife-sharp extinction horizon in the marine realm, and the well-known fern-spore peak in continental sediments of North America facilitate the precise location of the sometimes very thin ejecta layer (<mm) in undisturbed sections. Mineralogical, sedimentological, and geochemical anomalies characterize this ejecta layer, which is linked to the Chicxulub impact structure with a diameter on the order of 200 km (Morgan et al. 1997). Compared to the number of proven craters, impact debris is very scarce in the stratigraphic column (Grieve 1997). Only in three other cases, the source crater for distant ejecta material impact has been identified unambiguously. These are (1) the 1.03 Ma Ivory Coast tektites with a total mass of 20×10^9 g, which are connected with the Bosumtwi Structure (D = 10.5 km) in Ghana, (2) Moldavites with a total mass of 3×10^9 g, which are correlated with the 15 Ma Nördlinger Ries, and (3) the ejecta horizon of the approximately

590 Ma Lake Acraman Structure (D = 90 km), which has been traced over an area of 20000 km^2 in the monotonous Late Proterozoic shaly sediments of the Adelaide Geosyncline, South Australia. This ejecta layer consists of up to fist-sized rock fragments, shocked minerals, spherules, and shards pseudomorphosed after impact glass, and shows a pronounced anomaly of siderophile elements (Gostin et al. 1989). In addition, based on magnetostratigraphic, chemostratigraphic, and biostratigraphic arguments, Popigai (D = 100 km) is suggested as source crater for the PGE-enriched layer at the end of the Eocene (Langenhorst 1996), where shocked mineral grains and microtektites occur, but confirmation by high-precision ages is so far lacking. Most recently, the Chesapeake Bay impact structure has been proposed as source crater for tektites of the 35.5 Ma North American strewn field (Poag 1996).

Systematic search of the sedimentary record for distant ejecta layers by, for example, examination of quartz for shock features has proved to be painstaking and unsuccessful due to dilution by undeformed quartz grains of sedimentary origin (e.g., Schmitz et al. 1994). So far, distant ejecta deposits have been recognized first by Ir anomalies, followed by very detailed mineralogical analysis to prove the impact origin. Still controversially interpreted are unusual spherule deposits in the Early Archenan Barberton greenstone belt of South Africa (for a recent critical discussion, see Koeberl and Reimold 1995). The two beds, up to 1.5 m thick, are enriched in Ir and contain spinels of peculiar morphology, composed dominantly of chalcophile elements and with high Ni and ferric iron contents. The spinels are seen as products of condensation from a mixed target bolide vapor. If this interpretation is correct, these layers, and a recently proposed horizon in the around 2.5 Ga Hamersley group, W.A., Australia (Simonson et al. 1996), would represent the Earth's oldest distant ejecta deposits. The high cratering rate in the Early Archean implies that more distant ejecta layers should exist in such old sediments; they are, however, not yet identified.

1.10.5 Minerals in Terrestrial Impact Structures and their Characteristic Features

F. LANGENHORST and A. DEUTSCH

In the context of impact events, minerals can be affected or formed by a large variety of processes. From the genetic and chronological point of view, a distinction must be made between (1) primary minerals displaying shock-metamorphic overprint (including formation of glass and high-pressure polymorphs), and (2) new minerals formed by post-shock crystallization of impact melt or post-shock condensation of vaporized material. Shocked minerals are unequivocal indicators of impact events. They are, therefore, not only indispensable to prove the impact origin of a suspected crater-form structure, but also to finally confirm certain sedimentary features as distal ejecta layers (Bohor et al.

Advanced Mineralogy, Volume 3
Mineral Matter in Space, Mantle, Ocean Floor, Biosphere, Environmental Management, and Jewelry (ed. by A. S. Marfunin)

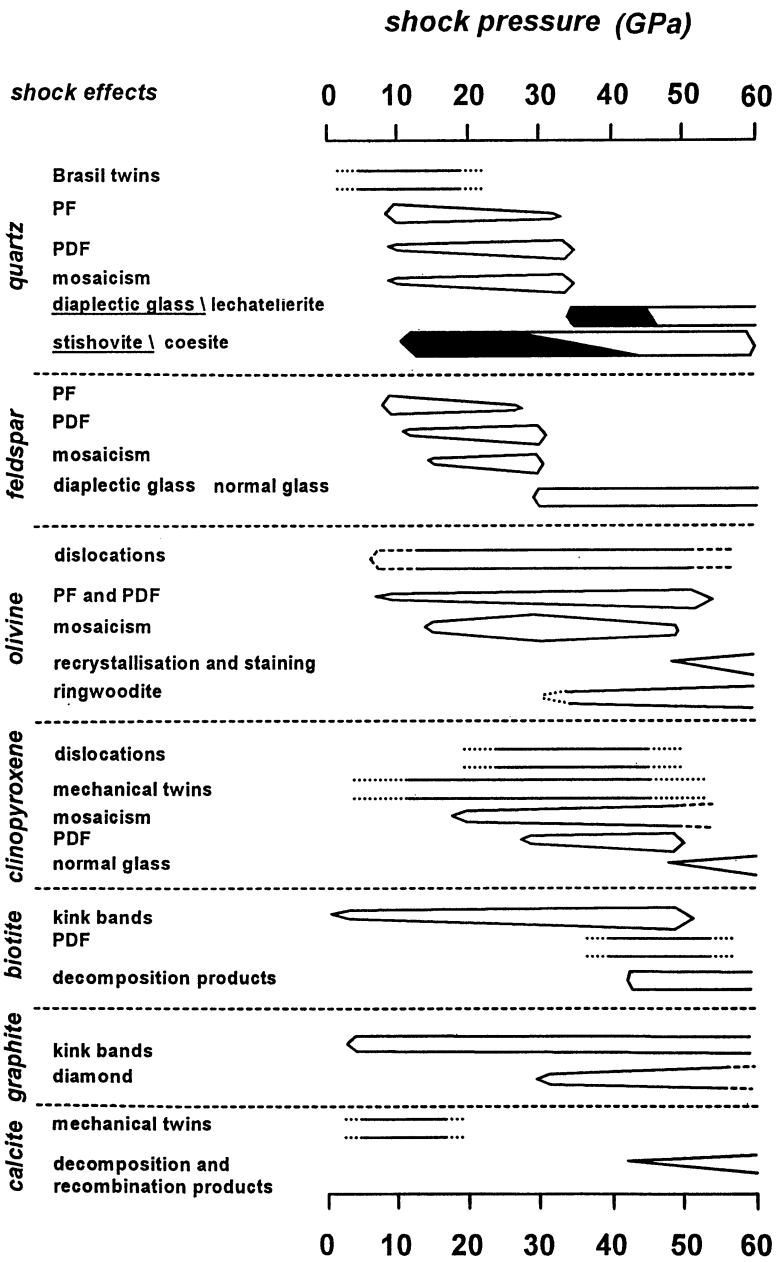

Fig. 24. Occurrence of specific shock effects in rock-forming minerals as function of shock pressure. Data obtained by shock experiments on compact samples.

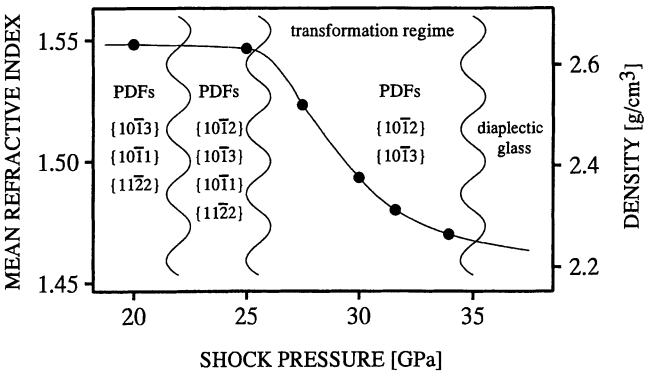

Fig. 25. Mean refractive index, density, and combinations of PDF orientations of experimentally shocked quartz as function of shock pressure. These properties serve as shock barometers (Langenhorst and Deutsch 1994).

1984). In addition, shock signatures of primary minerals provide important clues to shock conditions. Calibration data on the formation of specific shock effects in certain pressure regimes are available from shock recovery experiments on rocks or minerals (Figs. 24, 25). The knowledge of shock pressure and its attenuation rate is crucial for scaling impact craters and understanding cratering mechanics. Among newly formed minerals, spinels in distant ejecta deposits are of special interest, as their characteristics could help to better model physical and chemical processes taking place in the expanding vapor plume, although, so far, knowledge in this field is rather limited. Characteristics and conditions of formation of both shocked and newly formed minerals and their significance in impact research are the subjects of this chapter. Both types of minerals are often altered by post-shock annealing and/or hydrothermal overprinting. In as far as these processes yield secondary features or minerals, which are still suggestive of impact, they will also be discussed.

Shock Deformation and Transformation of Minerals

During shock compression and decompression, unique physical and chemical changes in minerals and rocks, generally referred to as shock effects, are induced. Shock effect is a collective and neutral term covering different categories of shock-induced changes, such as formation of lattice defects, high-pressure polymorphs, and diaplectic glasses, as well as changes in physical properties. Changes in physical properties are considered as indirect shock effects simply reflecting shock-induced phase transformations. In general, the term shock effect should be used only for changes originating during shock compression and decompression. Post-shock thermal effects, such as dissociation of minerals in a superheated ($\geq$2000 °C) impact melt, can be typical for

the impact environment, but are not directly related to the shock process (Fig. 20). As a consequence of their short formation time (<1 s in nature), shock effects represent disequilibrium changes that are, to some extent, unknown for minerals deformed in endogenic regimes.

Although a basic knowledge of some shock phenomena was already available from the petrographic study of meteorites (e. g., "maskelynite", a diaplectic plagioclase glass, was first described by Tschermak in 1872), most shock effects were discovered only in the late 1950 and early 1960 in either experimentally or naturally shocked material. At that time, shock effects were characterized by optical microscopy, which, due to limited resolution, prevents a clear recognition of the physical nature of shock effects. Recent transmission electron microscope (TEM) observations have largely improved knowledge and understanding of shock effects and have even led to the discovery of new submicroscopic shock effects, such as dislocations and microtwins; this field of research established a link to the material sciences. In this chapter, we concentrate on the new information which is now available for the rock-forming minerals, quartz, feldspar, olivine, and pyroxene. Characterization and definition of the most important shock effects are summarized in Table 9.

Table 9. Shock effects in minerals

Characteristic shock effects in minerals	Short definition
1. Formation of crystal defects	
a) Dislocations	Linear lattice defect
b) Planar microstructures	
– Planar fractures	Crystallographically oriented cleavage planes activated under dynamic compression
– Planar deformation features	Crystallographically oriented sets of amorphous lamellae (undecorated PDFs) and their post-shock modifications (decorated PDFs)
c) Mechanical twins	Crystal domains related by a point symmetry element (mirror, rotation or inversion axis), produced by deformation
d) Kink bands	Externally rotated crystal domains without crystallographic relationship to the host lattice, produced by deformation
e) Mosaicism	Internal blocky structure of shocked crystals
2. Transformations to	
a) High-pressure polymorphs	Densely packed modifications of minerals
b) Diaplectic glass	Quenched high-pressure melt preserving shape, internal textures, and composition of the precursor crystal
3. Decomposition	Dissociation of minerals into new solid phases (and gaseous species)
4. Melting and vaporization	Production of rock and mineral melt, and vapor

Dislocations

In its simplest form, a dislocation is a narrow line defect in which a plane of atoms stops within a crystal. Formation and migration of dislocations is the mechanism of deforming crystals under high stress. TEM analyses indicate that dynamic (shock) deformation is able to produce a large number of dislocations in certain minerals. Shocked olivine and clinopyroxene stand as instructive examples for minerals with high dislocation densities. On the other hand, shock cannot activate dislocations in minerals like quartz, in which the known formation mechanisms are simply too slow for activation of dislocations within the μs to s shock pulse.

Quartz. The lack of perfect dislocations in shocked quartz is due to its special mechanical behavior (Stöffler and Langenhorst 1994). Static deformation experiments have shown that the strength of dry quartz is comparable to the theoretical elastic limit of a few GPa. In the presence of water, however, quartz becomes ductile, a phenomenon known as hydrolytic weakening. Water in quartz crystals is the source for grown-in point defects. Diffusion of these water-related defects controls formation and mobility of dislocations. This is an extremely slow process compared to the time scale of shock compression, impeding formation and multiplication of dislocations in dynamically deformed quartz. When naturally shocked quartz contains numerous dislocations, these may have been formed by pre- or post-shock tectonic deformation.

Olivine. Dislocations are highly concentrated in olivine crystals from shock experiments and heavily shocked meteorites with densities up to 2×10^{14} m^{-2} (Fig. 26a). Since dislocations in olivine generally occur in the immediate vicinity of planar fractures, fracturing is interpreted as the cause of their formation (Langenhorst et al. 1995). The dislocations are almost exclusively of pure screw character and have the Burgers vector [001]. If present, edge segments are very short, enabling determination of the shock-induced slip systems, which are (100)[001], {110}[001], and (010)[001]. Apparently, dislocations with the Burgers vector [001] are quicker to activate than the energetically favorable dislocations with the shorter Burgers vector [100]. This consideration is consistent with results for olivine of static deformation experiments, revealing the dominance of dislocations with the Burgers vector [001] at relatively high strain rates (Carter and Avé Lallemant 1970).

Clinopyroxene. Shocked clinopyroxene is dominated by edge dislocations occurring with densities of up to 10^{14} m^{-2}. The predominant slip systems of dislocations are (100)[001] and, to a lesser extent, {110}[001]. Instead of a random distribution as in olivine, dislocations in clinopyroxene are often organized in the form of bands. As revealed by shock experiments (Leroux et al. 1994a), these dislocations originate at Frank-Read sources (Fig. 26b). A migration velocity of 500 ms^{-1} has been calculated from the distance to Frank-Read

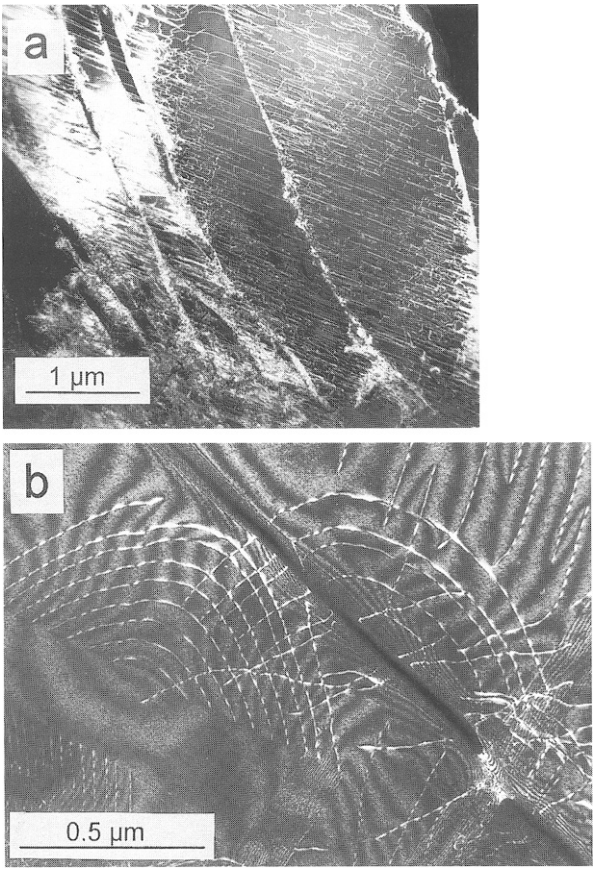

Fig. 26 a, b. TEM dark field images of one-dimensional shock defects (dislocations) in olivine and pyroxene. **a** Dislocations with Burgers vector [001] and irregular fractures in olivine from the Kernouvé chondrite, which has been experimentally shocked at 35 GPa. **b** Frank-Read source in diopside experimentally shocked at 45 GPa (Courtesy H. Leroux).

sources and the length of the shock pulse. Due to the significantly longer shock pulse in natural impact events, Frank-Read sources are more difficult to detect in naturally shocked clinopyroxene, since dislocations have migrated far away from their source.

Planar Microstructures

Many rock-forming minerals, e.g., quartz, feldspars, and mafics fail mechanically upon shock compression in two basic modes: by formation of planar fractures and planar deformation features. "Planar microstructures" as defined by Stöffler and Langenhorst (1994) is a collective term for these two different

types of microstructures, which are both oriented parallel to rational crystallographic planes of low Miller indices.

Planar Fractures (PFs). PFs usually form sets of parallel open fissures with a spacing of about 20–30 μm, allowing unambiguous recognition with the optical microscope, and occur in nearly all rock-forming silicates such as quartz, pyroxene, olivine, feldspar, amphibole, and garnet. PFs are unequivocal shock indicators if they are present (1) in minerals without normal cleavage, or (2) along planes which are not parallel to the normal cleavage of a mineral. Quartz, for example, known for brittle and irregular fracturing when statically deformed, develops under shock compression distinct PFs parallel to low index planes such as (0001) and $\{10\bar{1}\ 1\}$ (Fig. 27a). Olivine, displaying in the unshocked state only indistinct cleavage, fractures under shock compression preferentially parallel to the crystallographic planes (100), (010), (001), (110), (130), and (111). Orthopyroxene stands as example of a mineral, in which the shock-developed PF orientations such as (001) and (010) differ from the normal cleavage, which is parallel to (210) and (100). In some minerals, PFs commonly act as grain boundaries for the much more closely spaced planar deformation features.

Planar Deformation Features (PDFs). PDFs are multiple sets of parallel, planar optical discontinuities with a typical spacing <5 μm (Grieve et al. 1996). PDFs of the undecorated type ("fresh" PDFs) are resolvable by the optical microscope as unsharp, thin (<1–2 μm) lamellae. PDFs become clearly visible if, as an effect of post-shock annealing, their planes are decorated with tiny vugs (decorated PDFs). Decoration of PDFs is well known for quartz. At the TEM scale, fresh PDFs represent thin glass lamellae with a composition identical to the host crystal. These glass lamellae have been detected by TEM in quartz, feldspar, and clinopyroxene (e.g., Kitamura et al. 1977; Gratz et al. 1992; Leroux et al. 1994a; Fig. 27b, c). Based on optical observations, "PDFs" have been reported for a number of other minerals, e.g., olivine, amphibole, scapolite, biotite, sillimanite, apatite, and zircon (Stöffler 1972; Bohor et al. 1993), yet confirmation of the glassy nature of these planar microstructures by TEM is lacking. Minerals such as quartz and feldspars with a relatively low density, i.e., <3 g cm^{-3}, and thus high compressibility, tend to develop more and thicker PDFs than mafics such as pyroxene and olivine.

Quartz. Shocked quartz displays multiple sets of well-developed PDFs pervading the entire host crystal. Single quartz crystals may contain up to 15 differently oriented sets of PDFs. Displacements are not observed at the intercepts of PDF sets, indicating a shearless formation. The recent model of PDF formation assumes an origin directly in the shock front, which separates as sharp boundary uncompressed and compressed parts of the affected crystal (Goltrant et al. 1992). The lattice misfit between the two parts is compensated by the formation of densely packed amorphous lamellae, the PDFs. Predominant PDF

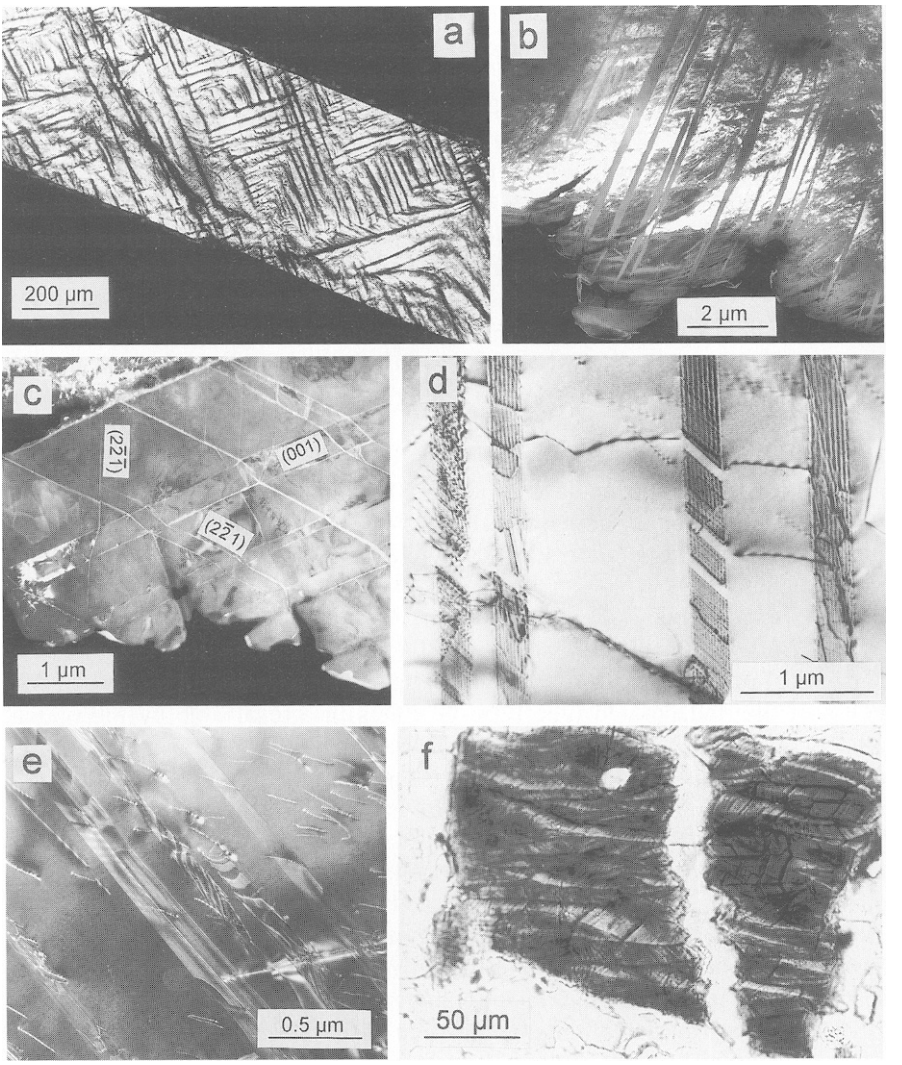

Fig. 27a–f. Two-dimensional shock effects (planar microstructures, mechanical twins, kink bands) in minerals. **a** Optical micrograph of planar fractures (PFs) in quartz experimentally shocked at 27.5 GPa (Langenhorst and Deutsch 1994). PFs are oriented parallel to {10$\bar{1}$1}. **b** TEM bright field image of amorphous lamellae, the PDFs, in quartz experimentally shocked at 30 GPa (Langenhorst 1994). **c** TEM dark field image of two PDF sets parallel to {221} in shocked diopside from the ordinary chondrite Tenham (Langenhorst et al. 1995). PDFs are deflected by mechanical twins parallel to (001). **d** TEM bright field image of basal Brazil twins in shocked quartz from the collar region of the Vredefort impact structure. (Courtesy H. Leroux). Twins are inclined to the electron beam giving rise to the formation of the fringe pattern. Twin boundaries contain numerous partial dislocations. **e** TEM dark field image of shocked diopside in the ordinary chondrite Tenham. Fringe patterns are inclined twins parallel to (100). Besides perfect dislocations, partial dislocations are visible in the twin boundaries. **f** Optical micrograph of kink bands in biotite in a suevitic granite clast from Seelbronn, Ries crater.

orientations in quartz are rhombohedral forms $\{10\bar{1}\,n\}$ with n = 1, 2, and 3, and trigonal bipyramids $\{11\bar{2}\,n\}$ with n = 1 and 2. Identification of other reported orientations, e.g., $\{21\bar{3}\,1\}$, $\{22\bar{4}\,1\}$, $\{51\bar{6}\,1\}$, $\{10\bar{1}\,0\}$, and $\{11\bar{2}\,0\}$ is based only on optical measurements. The frequently reported orientation (0001), known as basal deformation features (Carter 1965), does not belong to the PDF type of microstructures but is a fundamentally different type of defect, namely Brazil twins.

Universal stage measurements on PDFs in naturally shocked quartz have revealed that specific crystallographic PDF orientations or combinations thereof vary systematically with increasing shock intensity (von Engelhardt and Bertsch 1969; Robertson and Grieve 1977; Gurov and Gurova 1991; see literature in Stöffler and Langenhorst 1994). This pressure dependence of PDF orientations has been calibrated experimentally (Hörz 1968; Langenhorst and Deutsch 1994), and serves as a reliable barometer for estimating shock pressures in impactites; a compilation of PDF orientation data combined with refractivity and density data is given in Fig. 25. TEM studies on experimentally shocked quartz indicate that the mean thickness of PDFs correlates with pressure: below 25 GPa, PDFs are 20 to 30 nm thick, whereas those produced above 25 GPa are about 200 nm thick (Ashworth and Schneider 1985; Langenhorst 1994).

Physical properties of shocked quartz are distinctly influenced by the amount of PDFs. Larger amounts of these amorphous lamellae cause a reduction in refractivity and density. Enhanced lattice parameters of experimentally shocked quartz have also been explained by the presence of PDFs, which produce a distortion of the crystal lattice (Langenhorst 1994).

Feldspars. PDFs in feldspars also consist of amorphous material; they closely resemble those in quartz, and occur in a similar pressure range from 10 to 30 GPa. Their thickness may amount to 300 nm. Due to the variable composition and low symmetry of feldspars, especially plagioclase, it is difficult to reliably index PDF planes with stereographic projection. Dominant PDF orientations in andesine and labradorite are (001), (010), and (100); other reported orientations are (101), (111), $(1\bar{2}0)$, (130), and (203) (Stöffler 1972).

Clinopyroxene. The occurrence of PDFs in clinopyroxene was noted long ago by optical microscopy, but conclusive evidence for their presence has been provided only recently by TEM studies on clinopyroxene, either experimentally shocked or occurring in heavily shocked ordinary chondrites (Leroux et al. 1994a; Langenhorst et al. 1995; Fig. 27c). PDFs in clinopyroxene start to appear above 30 GPa and are thin (~ 50 nm) glass lamellae with a typical spacing < 1 μm. The monoclinic prisms {221} and {331} are the dominant PDF forms in clinopyroxene; they generally coexist with mechanical twins. In contrast to quartz, shearing seems to play an important role in PDF formation in clinopyroxene because PDF sets are displaced if they intersect each other or mechanical twins.

Mechanical Twins

Twinning is a common reaction of minerals of low symmetry to shock deformation. Mechanical twins in shocked minerals are visible under the optical microscope as narrow (<10 μm) polysynthetic bands; due to this appearance, the twins could be mistaken as exsolution lamellae. Extended and massive twin areas, however, are unknown in shocked minerals. Shock-induced mechanical twin lamellae have been reported for quartz, clinopyroxene, amphibole, sphene, ilmenite, and calcite.

Quartz. TEM studies revealed that one characteristic feature of weakly shocked quartz is mechanical Brazil twins with a mean thickness of about 50 nm; they are oriented exclusively parallel to (0001) (Kieffer et al. 1976; Goltrant et al. 1992; Leroux et al. 1994a). The twin boundaries contain numerous partial dislocations, indicating the mechanical nature of the Brazil twins (Fig. 27d). Identification of this feature by optical methods is complicated in thin sections of normal thickness if the twin boundaries are free of tiny fluid inclusions due to secondary alteration (decorated Brazil twins). The similar appearance of decorated PDFs and decorated Brazil twin boundaries was the reason for the erroneous description of the mechanical twins as PDFs.

Brazil twinning involves a change form left- to right-handed quartz or vice versa. It is known as either deformation or growth defect. The deformation Brazil twins are exclusively oriented parallel to (0001) and decorated with partial dislocations. In contrast, growth Brazil twins lack such dislocations and occur parallel to $\{10\bar{1}1\}$ and $\{11\bar{2}0\}$. Mechanical Brazil twins have not yet been reported for quartz shocked experimentally in the critical pressure range up to 15–20 GPa for probably two reasons: (1) thorough TEM search for Brazil twins in such material is still lacking, and (2) shock experiments were mainly performed with unfavorable quartz orientations [e.g., shock front parallel to (0001)], which impede high shear forces on (0001) and, thus, the production of Brazil twins. In static deformation experiments, however, thin mechanical Brazil twin lamellae develop if high (>1.5 GPa) and rapid shear stress is applied on (0001) (McLaren and Phakey 1966). Such conditions are absent in endogenous environments, and, hence, the occurrence of mechanical Brazil twins parallel to the basal plane is diagnostic for shock deformation in nature. The presence of Brazil twins proved to be an especially useful shock indicator when post-shock annealing has caused disappearance of the less robust PDFs.

Clinopyroxene. Clinopyroxene shocked in experiments, nuclear explosions, and natural impact events shows two types of mechanical twins with twin boundaries parallel to (100) and (001) (Müller 1993; Leroux et al. 1994a; Langenhorst et al. 1995; Fig. 27c, e). Both twin operations involve a change in the crystal orientation. The (100) twins are distinctly thinner (<10 nm) than the (001) twins (<0.5 μm). Therefore, only the latter can be identified by optical

microscopy on the basis of alternating extinction. The (100) twin boundaries contain concentric partial dislocations which are absent in the (001) boundaries. Thus, (100) twins are interpreted to form by gliding of partial dislocations, whereas (001) twins might originate from a rapid kinking process. If this explanation is correct, (001) twins represent a specific type of kink bands with a crystallographic relationship to the host crystal. Both types of twins have been produced in static experiments with high strain rates (10^{-4} s^{-1}; Kirby and Christie 1977); however, boundaries of the statically produced (001) twins contain partial dislocations, indicating a formation by gliding. Tectonically deformed diopside shows only (100) twins (Skrotzki 1994). The occurrence of dislocation-free (001) twins in diopside is therefore considered as reliable shock indicator.

Other Minerals. Little is known of the twinning behavior of other minerals. Amphibole has been reported to develop mechanical twins parallel to (001) and (100). In ilmenite, twins occur parallel to $\{10\bar{1}1\}$ and (0001), and sphene displays twins parallel to $\{221\}$. Mechanical twins were assumed to be rarely present in plagioclase, but proof for their mechanical nature is difficult because this mineral shows a large variety of polysynthetic growth twins. Shock-induced mechanical twinning probably takes place in carbonates. Calcite in limestones with shatter cones from impact structures shows intense microtwinning parallel to $\{01\bar{1}2\}$ and $\{10\bar{1}1\}$ (Robertson and Mason 1975). Similar twins form also in static deformation experiments (Barber and Wenk 1979).

Kink Bands

Kinking is a deformation mode commonly found in minerals with a sheet structure, e.g., micas and graphite, which exhibit only one dominant glide plane. Kinking develops if stress is applied in such a manner that extensive gliding is geometrically impossible, i.e., if the shock front is approximately perpendicular to the glide plane. In contrast to deformation twins, kink bands are not oriented parallel to rational crystallographic planes and display variable disorientation with respect to the host lattice.

Biotite. Kink bands have been studied most intensely in shocked biotite from the Ries crater, shock experiments, and nuclear test sites (Cummings 1964; Schneider 1972; Lambert and MacKinnon 1984; Fig. 27f). Compared to tectonically deformed biotite, shocked biotite shows a strong asymmetry of kink bands. Degree of asymmetry, frequency, and width of kink bands are correlated to shock pressure. In the case of the Ries crater, the orientation of kink bands has been used successfully to reconstruct the original position of ejected and overturned megablocks of the crystalline basement (Graup 1978).

Mosaicism

The term mosaicism describes the internal fragmentation of a single crystal into a mosaic of slightly disoriented crystal domains. Mosaicism is a common shock-wave damage in minerals, often accompanied by other shock effects such as planar microstructures. In thin sections, mosaicism appears as a highly irregular, "mottled" extinction pattern, which is distinctly different from undulatory extinction. The internal fragmentation causes a reduction of the long-range order of a crystal, allowing unambiguous detection by various X-ray and electron diffraction techniques (see references in Stöffler and Langenhorst 1994). In single-crystal diffraction patterns, mosaicism results in streakiness and broadening of the diffraction spots. In powder diffraction patterns, line broadening and a loss of higher-order reflections is observed, indicating domain sizes of <200 nm and the presence of internal strain. Successful attempts were made to quantitatively correlate domain size and internal strain with shock pressure using quartz, pyroxene, and carbonates (e.g., Dachille et al. 1968; Hörz and Quaide 1972; Hanss et al. 1978; Schneider et al. 1984; Ashworth and Schneider 1985; Langenhorst 1994; Martinez et al. 1995).

Diaplectic Glass

Minerals known to develop PDFs show at enhanced shock pressures an isochemical transformation to the amorphous state. This shock-produced glass is defined as diaplectic (from the Greek *διαπλεσσοσ* = to destroy by striking; von Engelhardt et al. 1967) or thetomorphic glass, yet the latter term has not gained acceptance, and is considered obsolete. Diaplectic glass is characterized by the preservation of morphological and textural features of the former crystal, e.g., crystal shape and twin boundaries, and by the absence of flow structures and vesicles. These features allow a clear distinction between diaplectic and shock-induced melt glass in thin sections. Diaplectic glass displays higher refractive index and density than synthetic glass of identical chemical composition. The formation of diaplectic glass, one of the most characteristic features of shock metamorphism, is mainly restricted to quartz and feldspars, i.e., minerals with open crystal structures containing three-dimensionally linked [SiO_4] tetrahedra. Transformation to diaplectic glass is strongly related to the formation of PDFs (Langenhorst 1994).

Quartz. In shocked quartz, amount and width of amorphous lamellae (PDFs) increase gradually with shock pressure until the PDFs coagulate at about 35 GPa to an entirely amorphous phase, the diaplectic glass. Calculation of shock temperatures and TEM observations indicate that PDFs formed at pressures >25 GPa represent, in compressed state, molten bands of silica. Therefore, diaplectic quartz glass has been interpreted as a high-pressure melt phase quenched upon decompression (Langenhorst 1994). Diaplectic quartz

glass may hence have maintained the densified structure of the melt, resulting in enhanced refractivity and density; its refractive index ranges up to 1.468, in contrast to 1.459 for synthetic silica glass (Stöffler and Langenhorst 1994). In nature, diaplectic quartz glass often coexists with the high-pressure polymorphs coesite and, to a minor extent, stishovite.

Due to the continuous nature of the transformation from shocked quartz with PDFs to diaplectic glass, refractive indices, birefringence, and density change continuously in the pressure range from 25 to 35 GPa (Fig. 25). These properties have been precisely calibrated by shock experiments on single crystal quartz, and serve as the most accurate indicator in shock barometry of terrestrial impactites. Careful application of the calibration data is required because pre-shock properties of the rock such as porosity, temperature, and polycrystallinity of the quartz influence onset and completion of the transformation, causing a shift in the pressure reading.

Feldspars. Diaplectic feldspar glass is a common constituent of terrestrial, lunar, martian impact lithologies, and ordinary chondrites (Stöffler et al. 1991). Maskelynite is a synonym for diaplectic glass of plagioclase composition. Formation of diaplectic feldspar glass is assumed to equal the transformation of shocked quartz to diaplectic quartz glass. Shocked feldspars also develop broad PDFs (although not to the same amount as quartz), which coagulate at enhanced pressures to an entirely amorphous phase. Chemical composition of unaltered diaplectic feldspar glass resembles that of the former feldspar; substantial loss of alkalies has not been observed. Systematic shock experiments have shown that the change in optical properties of alkali feldspars and plagioclases correlates with shock pressure (Ostertag 1983). According to the incipient decrease of refractive indices, transformation to diaplectic plagioclase glass begins in the pressure range of 22 to 25 GPa, and is complete between 26 and 30 GPa, dependent on the chemical composition. Albite transforms at higher pressures, and shows a stronger decrease in refractivity than anorthite. The gradual change in physical properties of feldspars also serves as a shock barometer, although it is less sensitive to pressure than in the case of quartz. This is due to the fact that the drop in refractivity is less significant, and, moreover, variable chemical compositions yield additional uncertainties. A peculiarity of diaplectic feldspar glasses is that they can have refractive indices and densities comparable to those of the unshocked original crystals.

High-Pressure Polymorphs

The presence of high-pressure polymorphs is striking evidence for natural impact events and, in some cases, has provided the ultimate proof for the impact origin of controversially interpreted geological structures such as the Ries and Vredefort. Quartz, graphite, orthopyroxene, and olivine are known to undergo partial or complete phase transitions to high-pressure polymorphs. Quartz

transforms to coesite and stishovite, graphite to diamond and lonsdaleite, orthopyroxene to majorite, ilmenite, and perovskite, and olivine to wadsleyite and ringwoodite. Except the solid-state transitions in the carbon system, these transformations are not direct and require, in an intermediate state, the formation of a high-pressure melt from which the high-pressure polymorphs crystallize. On the basis of Hugoniot data, the presence of high-pressure polymorphs has been proposed for zircon, rutile, and plagioclase, yet such phases have never been observed in naturally or experimentally shocked material.

Coesite and Stishovite. Both silica high-pressure polymorphs occur in dense crystalline impactites, shocked sandstone with high porosity, and thin pseudotachylite veins in quartzite country rocks (Stöffler 1971; Kieffer et al. 1976; Martini 1991; White 1993; Leroux et al. 1994b). In dense crystalline rocks, up to 40% of the host quartz is transformed to coesite, and up to 5% to stishovite. Coesite is found in quartz with PDFs and reduced refractive index, and, more frequently, in diaplectic glass, whereas stishovite occurs commonly in quartz with PDFs and less frequently in diaplectic glass. The estimated pressure ranges for the formation of coesite and stishovite are 30–60 GPa, and 12–45 GPa, respectively (Stöffler and Langenhorst 1994). Significant amounts of high-pressure polymorphs have been found in the porous Coconino sandstone of the Barringer crater but, in this case, coesite coexists with more than 80% of quartz, displaying PFs and diaplectic quartz glass. Stishovite occurs in Coconino sandstone at a higher shock level in an assemblage consisting of fractured quartz, amorphous silica, and coesite. The coexistence of the high-pressure polymorphs with fractured quartz implies formation at rather low shock pressures on the order of about 10 GPa. Thin pseudotachylites veins at the Vredefort Structure contain coesite and stishovite in paragenesis with silica glass and recrystallized quartz (Martini 1991); the immediate wall rocks carry quartz with mechanical Brazil twins.

According to TEM studies, coesite and stishovite form fine-grained (<3 μm), polycrystalline aggregates (White 1993; Leroux et al. 1994b). Coesite shows intense growth twinning parallel to (010) (Fig. 28a). These characteristics, as well as the general association of both high-pressure phases with diaplectic quartz glass or lechatelierite, provide evidence for a formation by rapid crystallization from a high-pressure silica melt.

Stishovite has been synthesized in shock experiments on quartz but, due to the extremely short pressure pulse of experiments (cf. Fig. 20), to a distinctly lesser extent ($\leqslant$1%) than in nature. This observation supports the outlined crystallization model. Formation of coesite has been reported in a shock experiment with quartz powder (Deribas et al. 1966) but could not be duplicated since.

Coesite, interpreted as an unambiguous shock indicator, has also been discovered in highly tectonized slabs of subduction zones and volcanic diatremes as inclusions in high-pressure phases such as diamond and pyrope. Mineral assemblages, texture, and crystal appearance, however, allow a clear distinction between endogenic and shock-produced coesite.

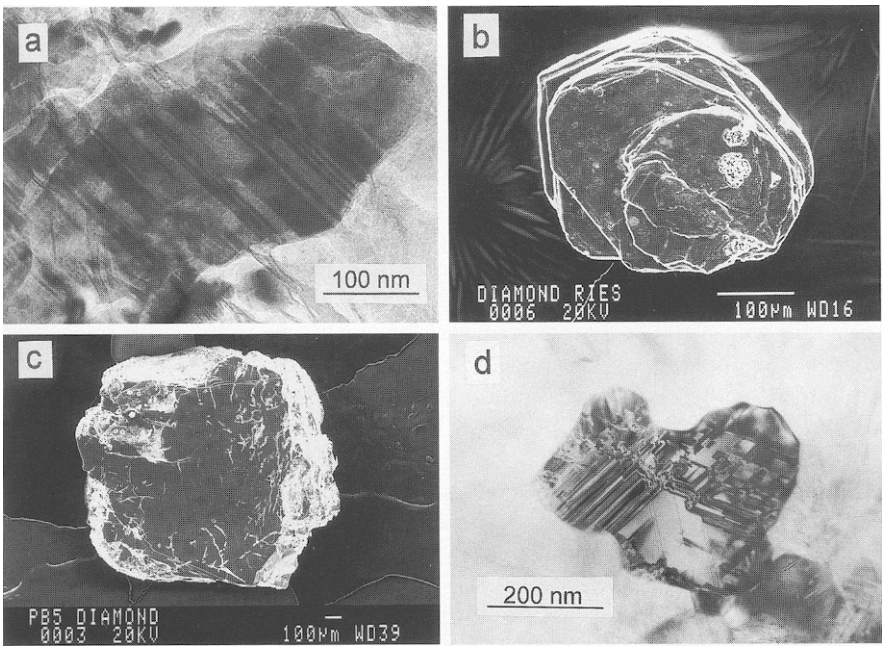

Fig. 28a–d. High-pressure phases found in terrestrial and extraterrestrial impactites. **a** TEM bright field image of a small coesite grain within a polycrystalline coesite aggregate in a suevitic granite clast from Bollstadt, Ries crater. The grain is pervaded by numerous growth twins parallel to (010). **b** Secondary electron image of an idiomorphic diamond platelet extracted from a suevite of the Otting quarry, Ries. **c** Secondary electron image of a black, polycrystalline diamond from the Popigai impact crater, Russia. **d** TEM dark field image of a ringwoodite grain in a shock vein of the ordinary chondrite Tenham. Planar defects are stacking faults parallel to {110} planes (Langenhorst et al. 1995).

Diamond and Lonsdaleite. Shock-produced diamond and the hexagonal carbon polymorph, lonsdaleite, were first synthesized in shock experiments (DeCarli and Jamieson 1961; Trueb 1971). On the basis of these experimental results it has then been realized that the long known diamonds in ureilites and the iron meteorite Canyon Diablo are of impact origin (Lipschutz 1964; Hannemann et al. 1967; Frondel and Marvin 1967; Clarke et al. 1981). Subsequently, impact diamonds have been detected in terrestrial impact structures, e.g., Popigai (Masaitis et al. 1972; Valter et al. 1992), several other craters of the former USSR territory (Gurov et al. 1985; Masaitis 1993), the Ries (Rost et al. 1978; Hough et al. 1995), and at two sites of the Cretaceous/Tertiary ejecta layer (Carlisle and Braman 1991; Gilmour et al. 1992). Shock-produced diamonds show frequently anomalous birefringence, and various colors, ranging from colorless, yellow, gray, to black, and are characterized by light carbon isotopes. They commonly occur as idiomorphic platelets or fragments of platelets. This morphology and other structural features (twins, layered structure) are inherited from the precursor mineral graphite, which has undergone a shock-

induced, martensitic solid-state transformation. Due to the inherited properties, platy impact diamonds are also called apographitic diamonds or paramorphs. X-ray diffraction experiments revealed the polycrystallinity of the paramorphs and an orientation relationship between diamond and graphite with (111) parallel to (0001), respectively. Diamond paramorphs are found as inclusions in strongly shocked (>30 GPa) crystalline clasts (mostly gneisses) of suevites and tagamites. In most cases, diamond paramorphs coexist with the hexagonal carbon polymorph, lonsdaleite, which, according to X-ray diffraction may amount up to 50–60% of the paragenesis. Lonsdaleite could not yet be imaged with TEM in these impact diamonds (Hough et al. 1995). Variable lonsdaleite contents may cause the variations in the color and the unusual birefringence of impact diamonds.

Impact diamonds formed by transformation of coal in sedimentary rocks present a peculiarity at the Kara crater. This type of impact diamonds is porous, has variable color (white, brown, black), and shows textural relics of the coal.

In suevites of the Ries, tiny skeletal diamonds intergrown with hexagonal and cubic SiC, phases forming at ambient pressure and high temperature, have recently been reported by Hough et al. (1995). Since epitaxial intergrowth of these phases is known from chemical vapor deposition (CVD) experiments, Hough et al. (1995) concluded that the skeletal Ries diamonds originated from vapor condensation. If this interpretation is correct, formation of CVD diamonds is not a primary shock effect, but related to vapor plume cooling.

Carbonados occurring exclusively in placers and low-grade metamorphic rocks of Precambrian age show similarities to impact diamonds (Grieve and Masaitis 1994). They also are irregular polycrystalline aggregates; their light $\delta^{13}C$ values and noble gas contents indicate trapped atmosphere, and rare earth element abundances point to a crustal source. This overall signature could indicate that carbonados are remnants of large Precambrian impact events (Smith and Dawson 1985; Hough et al. 1995). However, recent TEM studies revealed distinctly different microstructures in carbonados and impact diamonds (Langenhorst 1997). Impact diamonds are pervaded by planar defects (stacking faults) parallel to {111}, whereas carbonados display perfect and helically shaped dislocations in the {111} glide planes, pointing to plastic deformation in the deeper crust or upper mantle.

Majorite, Wadsleyite, Ringwoodite, Ilmenite, and Perovskite. These high-pressure phases are major phases of the Earth's lower mantle and transition zone, and have been thoroughly studied in static high-pressure experiments (e.g., Manghnani and Syono 1987). These phases have also been detected as components of melt veins in heavily shocked ordinary chondrites (Putnis and Price 1979; Madon and Poirier 1983; Mori 1984; Langenhorst et al. 1995; Chen et al. 1996; Sharp et al. 1997). On Earth, however, these high-pressure polymorphs have not yet been identified in impactites, but may occur in pseudotachylites transecting ultramafic lithologies such as peridotites. Among these minerals, only ringwoodite can be unambiguously identified on the optical scale by its

distinct violet color. Majorite, ilmenite, and perovskite have pyroxene composition $(Mg,Fe)SiO_3$ and crystallize in the garnet, ilmenite, and perovskite structures, respectively. Wadsleyite and ringwoodite are $(Mg,Fe)_2SiO_4$ high-pressure polymorphs and crystallize in the β- and γ-spinel structures, respectively. Characterization of lattice defects revealed the presence of stacking faults in the spinels, occurring parallel to (100) in wadsleyite, and parallel to {110} in ringwoodite (Fig. 28 d).

Recent TEM studies of heavily shocked (shock stage S5 or S6) ordinary chondrites have revealed a large variety of disequilibrium high-pressure mineral assemblages occurring as fine-grained, polycrystalline aggregates in thin shock dikes. Majorite has been found in the Sixangkou L6 chondrite in high-pressure assemblages with magnesiowüstite or ringwoodite (Chen et al. 1996). The majorite, which is cogenetic with magnesiowüstite, shows enhanced contents of minor elements such as, for example, Na, Ca, Al, Cr, and it thus represents a majorite-pyrope solid solution. The difference in composition to enstatite in the host meteorite suggests crystallization from a high-pressure melt as formation mechanism. On the other hand, the majorite (low Ca) plus ringwoodite assemblage shows no significant compositional deviation from the host enstatite and olivine, respectively. This assemblage has been interpreted as having formed by a solid-state transformation.

Mori (1994) reports a high-pressure assemblage of amorphous $(Mg,Fe)SiO_3$ grains plus magnesiowüstite. It is assumed that perovskite was the precursor phase of the $(Mg,Fe)SiO_3$ glass since perovskite, at ambient pressure and moderate temperature (>150 °C), is unstable. A new mineral assemblage consisting of ringwoodite, $(Mg,Fe)SiO_3$ ilmenite, and amorphous $(Mg,Fe)SiO_3$ grains, which are also interpreted to be the result of perovskite amorphization, has been discovered in the L5-6 chondrite Acfer 040 (Sharp et al. 1997). It is concluded that crystallization from the high-pressure melt started with perovskite formation and was followed by growth of ilmenite and ringwoodite. Recently, crystalline $(Mg,Fe)SiO_3$ perovskite and ilmenite have also been identified in topotaxial relationship with pyroxene in the Tenham meteorite (Tomioka and Fujino 1997).

Shock experiments on olivine and enstatite generally failed to synthesize high-pressure Mg-silicates, with one exception. Jakubith and Hornemann (1981) report the production of majorite at 40 and 45 GPa. The detection of majorite was based on X-ray photoelectron spectroscopy (XPS) and X-ray diffraction techniques. Conclusive evidence is, however, lacking because imaging techniques have not been employed, and other attempts to synthesize majorite failed (Ahrens and Gaffney 1971).

Decomposition

Shock-induced decomposition of volatile-bearing minerals, e.g., sulfates, carbonates, and hydrous silicates (micas, serpentine, amphibole) played an important role in the formation of the early atmosphere. In the context of the mass

extinction at the K/T boundary, the amount of CO_2 and SO_2 shock-released from the sediments in the Chicxulub target area is crucial for evaluating possible atmospheric perturbation (Brett 1992; Pope et al. 1994). Experimental data for the threshold pressure of outgassing are inconclusive and lower than those estimated from thermodynamical equilibrium calculations (Martinez et al. 1995). Grain size and sample porosity have strong effects on lowering the pressure for incipient volatilization, the experimental set-up also seems to influence the result.

Sulfates. Sulfates are highly resistant to shock loading. The shock pressure for incipient vaporization of anhydrite is about 80 GPa, whereas an anhydrite-quartz mixture starts to devolatilize in experiments already at about 30 to 40 GPa. The mineralogical proof for the reaction, for example, in the form of a solid reaction product such as $CaSiO_3$, has neither been reported from the recovered experimental material nor discovered in naturally shocked sulfates (Chen et al. 1994).

Carbonates. CO_2 release from porous chalk has been observed in experiments at particularly low pressures around 10 GPa, which is attributed to the formation of localized hot spots. Recent experiments indicate that devolatilization of non-porous dolomite and calcite starts at 55 to 65, and 35 to 45 GPa, respectively, which is in good accordance with thermodynamical calculations (Martinez et al. 1995). Mineralogical corroboration for shock-induced degassing of carbonates by the occurrence of newly formed minerals requires TEM techniques. So far, solid reaction products are documented in only two cases. Dolomite, shocked experimentally at 60 GPa, contains 20-nm-sized MgO crystals. At the Haughton crater, Ca-Mg-rich melt glass, larnite, and augite crystals occur in highly shocked clasts of carbonate sediments. One likely reason for the apparent lack of calcium-magnesium oxides, hydroxides, and silicates in shocked carbonates is the immediate back reaction of CO_2 with the very fine-grained CaO/MgO crystals, known for their efficiency in trapping carbon dioxide (Agrinier et al. 1995).This process has been documented via stable isotope measurements in the allochthonous breccia deposits at the Haughton Crater (Martinez et al. 1994). Most recently, up to 2 cm sized dolomite spheroids in the ca. 15 m thick K/T ejecta deposits in Belize have been interpreted by Pope et al. (1996) as recondensates of the Chicxulub vapor cloud; yet these spheroids may represent an alteration feature (caliche).

Hydrous Silicates suffer under shock compression substantial loss of water. Dehydration of shocked hydrous silicates is often evidenced by darkening and pervasive vesiculation of the mineral grains. In some cases, shock experiments provide data on the amount of dehydration as function of shock pressure. Incipient and complete dehydration of serpentine is observed at 20 and 65 GPa, respectively (Lange et al. 1985). Shock experiments on gneisses reveal that the water loss in micas is accompanied with shock-melting (Lambert and Mackinnon 1984). Complete water loss in biotite has been noted at 70 GPa.

Shock-Fused Glass

Shock-induced melting and vaporization represents the highest degrees of shock. Calculations of shock temperatures indicate that highly shocked (>50 GPa) minerals melt already under compression, whereas vaporization takes place during decompression when the liquid-vapor boundary is approached (Melosh and Vickery 1991).

Shock-Fused Glasses with Mineral Composition. Threshold pressures for shock melting of minerals are variable and depend largely on the compressibility of the respective mineral as well as on pre-shock temperature, and porosity of the host rock. Strongly shocked, polymineralic rocks undergo selective melting. Post-shock quenching of the melts results in formation of glasses with mineral composition, which, in contrast to diaplectic glasses, show flow structures and vesicles, and obliteration of the original crystal shape. This observation indicates that shock-fused glasses were, for a short period of time after decompression, still molten. The occurrence of these glasses has been reported for leucocratic minerals and a few mafics. Glasses of plagioclase or alkali feldspar compositions are widely observed in crystalline rocks shocked at pressures >45 GPa. Silica glass with flow structures, lechatelierite, quite commonly occurs in impact craters formed in sedimentary rocks or loose quartz-rich sediments (French and Short 1968; Kieffer et al. 1976; Hörz et al. 1989; Stöffler and Langenhorst 1994). Formation of lechatelierite in dense rocks requires pressures in excess of 50 GPa.

Mafic minerals such as (OH)-bearing phases (micas, amphiboles) either decompose incongruently or form glass matching the starting material in composition, except that crystal water is quantitatively driven off (Lambert and McKinnon 1984). Despite quenching, nm-sized spinels of unusual composition may crystallize in such shock-fused glasses (Martinez et al. 1993; Schrand et al. 1996). Monomineralic melts of other mafics, such as olivine, are not capable of being quenched to glass, but rapidly crystallize in the form of fine-grained polycrystalline aggregates. This phenomenon is erroneously referred to as recrystallization although the term is restricted to solid state processes.

Rock Glasses. Melting at the whole-rock scale occurs for most dense rocks at pressures exceeding 80 to 100 GPa. The resulting melt is deposited as splash-form glass particles and "bombs" in suevitic breccias or as coherent impact melt body. Small melt volumes might be quenched to rock glasses, whereas in the case of large coherent impact melt sheets such as observed at Sudbury, rapid quenching to glass is impossible and the melt crystallizes as observed in endogenic magmatic complexes. Initial post-shock temperatures of coherent melt bodies are on the order of 2000 °C. Another type of impact melt is produced very early in cratering from the uppermost target layers and ejected ballistically at high velocities; it forms the tektites (see p. 93).

Formation of New Minerals in Impact Melt and Vapor

Crystallization of impact melt and condensation of the vapor result in formation of new minerals. In the case of large impact melt bodies, e.g., at Sudbury, the slow cooling allows differentiation, yielding a "normal" igneous crystallization sequence. Minerals suggestive of impact, however, form in smaller impact melt volumes due to quenching with distinct undercooling. The solid state can already be achieved during the ballistic transport or immediately after deposition in close contact with cold neighboring lithologies. In both cases, quenching is accelerated by the admixture of cold solid clasts, and results in the formation of minerals with exotic crystal shapes. For example, plagioclase whiskers with hollow crystal morphologies and forked faces are a typical constituent in parts of impact melt sheets with glassy matrix and perlitic textures, e.g., at the Scandinavian craters Dellen, Mien, and Lappajärvi (Carstens 1975; Deutsch et al. 1992). This plagioclase shows oscillating zoning and the rectangular holes are filled with glass.

Metal Spherules. Impact glasses are important carriers of metallic spherules with diameters ranging from a few μm up to 100 μm (El Goresy et al. 1968; Fregerslev and Carstens 1976). Metal spherules are usually found at craters formed by impact of iron meteorites, e.g, Barringer, Bosumtwi, Henbury, Montaruqui, Chile (D = 460 m), and Wabar, Saudi Arabia (D = 97 m); such spherules occur also in craters produced by a stony projectile, e.g., at Lappajärvi. The metallic spherules consist of an FeNi metal core surrounded by pyrrhotite. Other sulfides, e.g., chalcopyrite, pentlandite, and millerite, are present to a minor extent.

Spinels in Microtektites. Spinels are important new mineral phases in distal ejecta horizons such as the K/T and Eocene/Oligocene boundaries and the Late Pliocene sediments of the South Pacific close to the Eltanin Mt. impact (Smit and Kyte 1984; Robin et al. 1992; Kyte and Bostwick 1995). The spinels are constituents of quenched impact melt droplets, less than 1 mm in diameter (microtektites), which are assumed to form in the ejecta plume. Small grain sizes (<10–20 μm) and skeletal/dendritic crystal morphologies suggest an origin of the spinels by rapid crystallization from the melt. The impact spinels are almost exclusively magnesioferrites, or magnetites with low Ti and Cr, but high Ni, Mg, and Al contents, making them distinctly different to all other terrestrial spinels. Due to this peculiar chemical composition, the spinels serve as good indicators for large-scale impact events. Their high Fe^{3+}/Fe^{2+} ratio reflects the highly oxidizing conditions during formation in the atmosphere. Recently, Ni-rich magnesiowüstite, a phase crystallizing only from ultrarefractory MgO-rich liquids, has also been detected in K/T microtektites (Kyte and Bohor 1995). Although the glassy groundmass of these K/T microtektites is generally replaced by sanidine and glauconite, the spinels survived this alteration. In the case of the Eltanin Mt. impact, the impact glass is still preserved (Margolis et al. 1991; Fig. 29a, b).

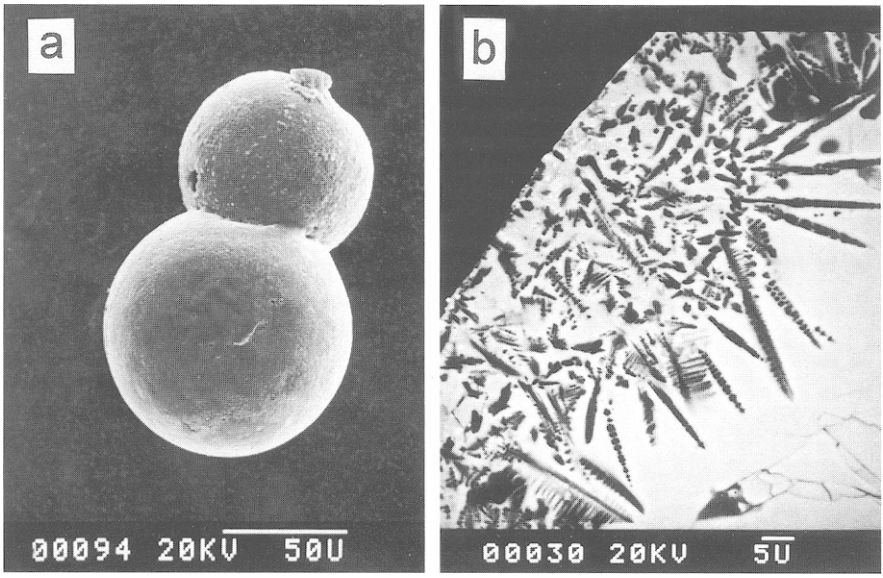

Fig. 29a, b. Secondary electron images of microtektites found in Late Pliocene sediments containing debris from a small asteroid impact in the Southern Ocean. (Courtesy P. Claeys). **a** Two spherules sticking together. **b** Cross-section of a glass spherule with dendritic spinels

Decomposition Products. Along with decomposition and devolatilization of minerals under shock and decompression, decomposition also occurs as a corollary to annealing if minerals are incorporated in superheated impact melts. Decay of zircon to baddeleyite and silica glass is a common phenomenon in impact glasses, e. g., at Bosumtwi, Henbury, and the Ries, and is also known for Libyan desert glass (El Goresy et al. 1968; Kleinmann 1969). The reaction starts above 1676 °C, which is well above the temperature regime in melts of endogenous origin. A further example for post-shock decomposition is the breakdown of Cr-rich spinels to eskolaite (Cr_2O_3) and spinel ($MgAl_2O_4$) (El Goresy et al. 1968).

Post-shock Annealing and Alteration of Shocked Minerals

After deposition of impact debris and melt in and around the modified crater, shocked minerals are exposed to annealing and hydrothermal alteration. Annealing effects and alteration products develop particularly in impact melt rocks and suevitic breccias because of their high residual temperatures; circulating hydrothermal fluids are the second fundamental factor in these post-shock processes. Annealing is most important for the modification of impactites, and finally can result in total recovery of primary shock effects (Grieve et al. 1996) and devitrification of impact glasses.

Annealing Effects in Shocked Minerals. Characteristic annealing effects, including recovery of primary shock features, develop if clasts of shocked minerals and rocks are incorporated in superheated impact melt. The effects are less pronounced in suevites or clastic matrix breccia due to their lower formation temperatures. Regional metamorphic and hydrothermal activity may enhance annealing.

Clasts of shocked plagioclase and microcline acquire in impact melts so-called checkerboard and ghost-like textures (Bischoff and Stöffler 1984). Checkerboard-feldspars consist of about 10 μm subgrains (Fig. 30a) which are equally oriented and surrounded by an interstitial mesostasis of different

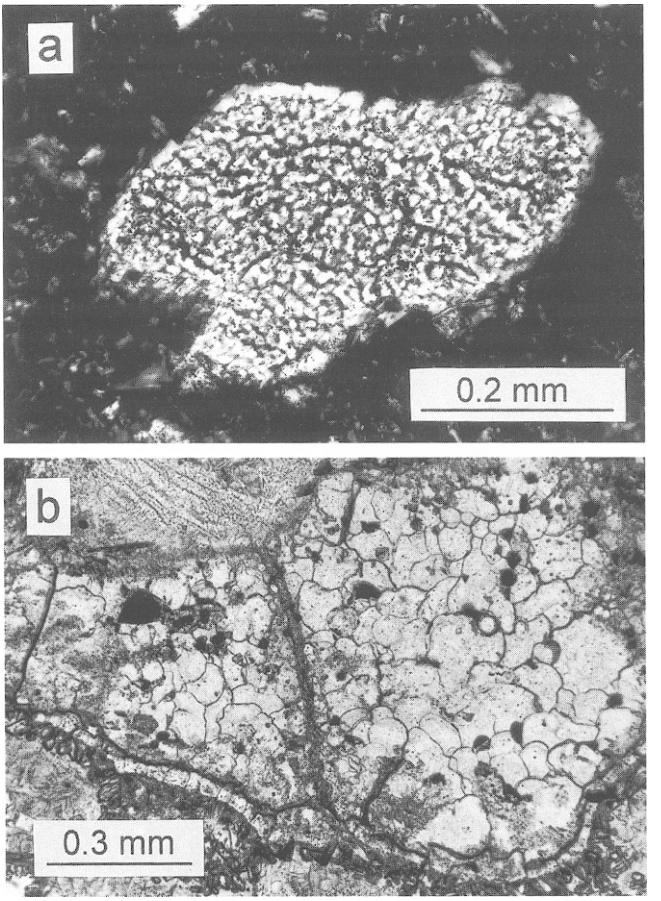

Fig. 30a, b. Annealing effects in mineral clasts found in Kärnäite (impact melt breccia) of the Lapajärvi impact structure, Finland. **a** Plagioclase fragment with checkerboard texture within a fine-grained crystalline matrix. **b** Quartz fragment with ballen texture and reaction zone embedded in the crystalline matrix.

composition. The uniform orientation is interpreted as memory effect to the crystal orientation of the precursor feldspar, which was either weakly shocked (<30 GPa) or a diaplectic glass (30–45 GPa). For example, in impact melt rocks at Lappajärvi, weakly shocked microcline clasts are converted into An-rich plagioclase subgrains rimmed by sanidine and a mesostasis consisting of tiny sanidine and quartz grains. These characteristics indicate heating of the shocked microcline above the liquidus temperature for a short period of time. Subsequent quenching caused fractional crystallization of the melt of microcline composition, which, according to the phase diagram, started with crystallization of plagioclase and completed with eutectic crystallization of sanidine and quartz. Ghost-like feldspar clasts have blurred contours and consist of randomly oriented feldspar laths with minor amounts of mesostasis. These ghosts are interpreted as having been fused at shock pressures in excess to 45 GPa prior to incorporation in impact melt. Compared to the weakly shocked feldspar clasts developing the checkerboard texture, the shock-fused feldspars were sustained for a longer period of time above liquidus temperature and the new feldspars crystallized with random orientation from the molten clast.

Shocked quartz incorporated in impact melt may develop a "ballen" texture (Carstens 1975; Grieve et al. 1996; Fig. 30b), which resembles a cauliflower-like fracture pattern. It is assumed that ballen quartz represents a paramorph of quartz after lechatelierite. Due to the high temperatures of impact melts, quartz has, however, not directly formed by devitrification of lechatelierite. In a transient state, high-cristobalite recrystallized and transformed to low-cristobalite, causing a volume contraction which subsequently results in the typical fracture pattern. Annealing of experimentally produced diaplectic quartz glass at temperatures above 1200 to 1300 °C yields a similar ballen texture. At these temperatures, diaplectic quartz glass recrystallizes to a mixture of crystalline α-quartz and cristobalite, whereas synthetic silica glass always transforms to pure cristobalite under identical conditions.

As illustrated in Fig. 31 for shocked quartz, a combination of aqueous alteration and annealing cause progressive modification of PDFs, leading finally to their decoration with tiny bubbles (Grieve et al. 1996). The aqueous fluids dissolve predominantly in PDFs because of the high solubility of water in amorphous silica, which is up to 6 wt.% H_2O, whereas, only <100 ppm are soluble in quartz (Cordier and Doukhan 1989). Annealing of the shocked quartz starts with recrystallization of the amorphous material, which itself is assisted by the presence of water. This leads in the first stage to a mixture of amorphous silica and minute quartz crystallites (<10 nm; Fig. 31b), as observed by Goltrant et al. (1991, 1992). Progressive recrystallization causes coarsening of the quartz crystallites and exsolution of water within the former PDFs in the form of bubbles. This results simply from the fact that the newly formed quartz crystallites are extremely oversaturated in water. The internal pressure increases with increasing size of the bubbles. Relaxation of the overpressure is achieved by incorporating SiO_2 from the bubble surface as extra half planes into the surrounding quartz lattice. A high density of sessile dislocation loops is formed

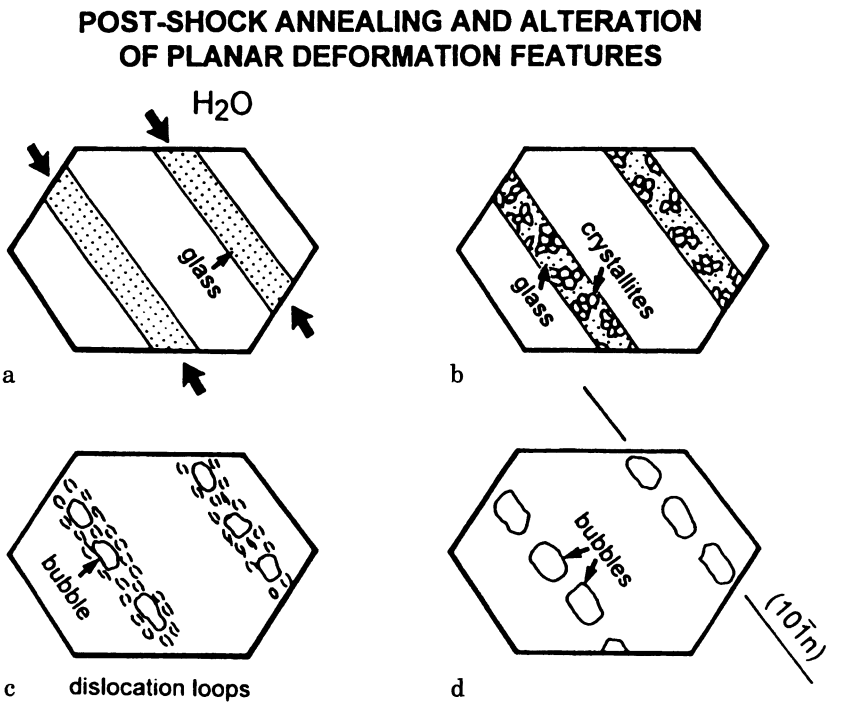

Fig. 31a–d. Schematic drawings of progressive post-shock modification of planar deformation features in quartz. **a** Initial state of glassy PDFs affected by hydrous fluids. **b** Incipient recrystallization of the glass to tiny quartz crystallites. **c** Progressive recrystallization leading to the disappearance of glass, exsolution of water, and incorporation of dislocation loops in the surrounding lattice. **d** Final state of a PDF consisting of tiny bubbles aligned along the planes of the original PDFs

decorating, together with the bubbles, the original PDF (Fig. 31 c). Such PDFs, consisting of a large density of dislocations and bubbles, are particularly observed in quartz grains from K/T sites and relatively young, Cenozoic impact craters (Goltrant et al. 1991, 1992). If annealing is sustained much longer, as in the case of the 2 Ga Vredefort structure, the only remnants of PDFs are aligned bubbles still showing the orientation of the former amorphous lamellae (Fig. 31 d). The dislocations have been transported out of the crystal or are reorganized in the form of subgrain boundaries.

Knowledge of post-shock annealing of shocked mafic minerals is relatively limited (Feldmann 1994). Recrystallization of shock-damaged biotite from the Janisjärvi and Popigai craters led to an assemblage of K-feldspar, orthopyroxene, and ilmenite. Strongly shocked garnets from the Popigai and Ries craters recrystallized to an assemblage consisting of fine-grained hercynite, hypersthene, and alkali feldspar. Annealing of strongly shocked amphiboles from the Puchezh-Katunky crater resulted in the formation of fine-grained aggregates

composed of plagioclase, amphibole, clinopyroxene, magnetite, and, rarely, K-feldspar.

Devitrification of Impact Glasses. Due to rapid quenching of impact melts, the resulting glasses are often oversaturated in water and exhibit high internal strain. Therefore, post-shock annealing easily initiates devitrification of impact glasses. Pyroxene, plagioclase, and subordinate magnetite have been identified as devitrification products in impact glass of the Ries suevite (von Engelhardt et al. 1995). Ortho- and clinopyroxene trichites occur in the form of hairs or have worm-like shapes ranging in thickness from 1 to 5 μm or as minute star-like and point-like crystallites. Clinopyroxenes show remarkably high Al_2O_3 contents of up to 10 wt.%, which has been detected so far only in lunar impact melt rocks of basaltic composition. Plagioclases form laths or fan-like to spherulitic aggregates.

Alteration Products. Mobilization of water and other volatiles results from shock-induced decomposition itself and, more importantly, post-shock waste heat in the deposited breccias, which expel volatiles from underlying colder lithologies. Vertical degassing pipes with a diameter of 2 to 40 cm in suevites at the Ries illustrate the importance and extent of volatile mobilization in impact deposits (von Engelhardt 1972). Alteration products in terrestrial impact formations are dominated by clay minerals (smectite, chlorite, montmorillionite, illite), zeolites (analcite, phillipsite, chabasite, etc.), K-feldspar, and quartz; to a minor extent, carbonates (calcite, siderite) and sulfates (barite) are present (Allen et al. 1982). Clay minerals such as Fe-chlorites and smectites reflect formation temperatures on the order of 100 to 300 °C. Suevites of the Ries contain up to 20 wt.% of Fe-rich montmorillionite occurring as coating of vesicles with constant thickness of about 10 μm. Their honeycomb texture, lack of illite interlayers, and presence of zeolites indicate temperatures around 100 °C for the hydrothermal alteration (Newsom et al. 1986), even though the deposition temperatures are estimated to be about 750 °C (von Engelhardt et al. 1995).

1.10.6 Examples for Terrestrial Impact Structures

A. Deutsch

The Nördlinger Ries – an Excellently Preserved Complex Impact Structure

Nördlinger Ries. The 15.0 Ma Ries (N 48°53′ E 10°37′) is a complex crater with a rim-to-rim diameter of about 26 km (Pohl et al. 1977). Due to the quite

Advanced Mineralogy, Volume 3
Mineral Matter in Space, Mantle, Ocean Floor, Biosphere, Environmental Management, and Jewelry (ed. by A. S. Marfunin)

complete preservation of the continuous ejecta blanket outside, and the breccia lens inside the crater, this complex impact structure is one of the most remarkable documents of impact cratering on Earth.

The Ries crater has a stratified target comprising crystalline basement of Hercynian age, covered by up to 700 m thick sediments which range from Permian to Miocene; among the sediments, limestones and marls dominate over shales, clays, and sandstone. The Ries consists of an almost circular, central basin with a diameter of about 12 km, whose flat surface is formed by 250 to 350 m of post-impact lake sediments. This central basin is bordered in the W, SW, and E by a horseshoe-shaped chain of isolated hills, the so-called inner ring, standing about 50 m above the central plain and consisting of large monomict brecciated, uplifted blocks of the crystalline basement with breccia dikes and shatter cones. Displaced megablocks, covered in part by lake sediments, make up the about 6 km wide zone between the inner ring and the tectonically modified crater rim, reaching up to 150 m above the plain. Differential erosion has removed part of this rim to the north. A unique feature of the Ries as compared to other terrestrial complex crater, is the excellent preservation of an appreciable part of the continuous ejecta blanket, extending mainly to the south and east up to about 45 km from the crater center, and forming a hummocky terrane.

This ejecta deposit is an up to 200 m thick clastic matrix breccia – the local term Bunte Breccia is now used to characterize similar rocks at other impact sites, composed of unshocked or only moderately shocked rock and mineral fragments of all stratigraphic units in the target. Up to 95 vol.% of the fragments are sedimentary, the remainder crystalline rocks; clast range in particle size from μm to nearly 1 km sized blocks. Beyond the continuous ejecta deposit, isolated fist-sized and brecciated fragments of Malmian limestone (Reuter blocks) occur within a layer of Miocene sediments in the Molasse basin south of the river Danube at distances up to 70 km. Distant ejecta are represented by the Moldavite tektite strewn field found at a range of more than 350 km in the Czech Republic, and at discrete localities in East Germany (Lausitz area) and Austria (villages of Stainz and Horn).

The Bunte Breccia is locally overlain by an up to 25 m thick layer of suevitic breccia (fallout suevite) occurring inside a radius of about 22 km as patches of several hundred m^2 to some km^2 extension. Impact melt particles in this suevite – their local name is Flädle – range in size between sub-mm and 50 cm and show signs of aerodynamical transport (glass bombs). A recent petrofabric examination indicate that transport of the fallout suevite occurred in part by horizontal movement, similar to a pyroclastic flow (Bringemeier 1994). Amongst the fragments, the up to some decimeters sized lithologies of the crystalline basement dominate over the much smaller sedimentary clasts. Crystalline rock fragments display all degrees of impact metamorphism. Impact diamonds occur in the suevite at the Otting quarry. From this locality, coesite and stishovite have been reported, providing in the 1960s the final proof for an impact origin of the Ries. Deposition temperature of the fallout

suevite was below 750 °C. Chilled zones are known from the base (~ 1 m) and the top (~ 10 m) of the suevite deposits. Emanating gases and hot vapor caused large-scale montmorillonitization of the matrix and formation of degassing pipes.

Coherent, clast-rich impact melt, the so-called red suevite, occurs at the eastern crater rim in several large masses extending to 50 m^2. The once glassy, vesicular matrix of this massive rock is completely recrystallized to a fine-grained aggregate of feldspar, pyroxen, hematite, and cristobalite. The fragment load of this melt consists nearly exclusively of crystalline lithologies displaying all stages of impact metamorphism.

The crater cavity is filled with a breccia lens, consisting from top to bottom of several m of sedimentary reworked suevitic breccia, about 15 m of graded suevite, and an up to 400 m thick suevite layer which, in its lower section, is gradually poorer in melt particles. At a depth of about 500 to 550 m from the present surface, drilling reached the brecciated crystalline basement, which is penetrated by dikes of suevitic breccia. Below about 650 m, the crystalline rocks still display a weak impact metamorphic overprint, decreasing with depth, as well as shatter cones, and numerous up to cm-thick dike breccias. The absence of a thick coherent layer of impact melt at the Ries is ascribed to the predominantly sedimentary target rocks, which, at high shock and post-shock temperatures, may decompose into gas and a solid residue but not melt.

Extensive geophysical measurements have revealed details of the subsurface structure of the Ries. Strong and irregular negative magnetic anomalies with an inverted field vector have been determined for the central cavity; they reflect the magnetization of the suevite layer. The area within the crater rim is characterized by a centrosymmetrical gravity low of up to 18 mgal. The hemispherical zone of brecciated basement with reduced density and seismic wave velocities extends to a depth of about 6 km and a radius of about 13 km.

Research on the Ries, in particular drilling, e.g., the Forschungsbohrung Nördlingen 1973 with 1206 m core recovery, and minute petrographic work, yielded some basic facts for a better understanding of the cratering process. For example, analyses of nine shallow drill cores, penetrating through the Bunte Breccia of the continuous ejecta blanket outside the crater rim into the uppermost ground zero surface, produced first evidence for regularities in the composition of such ejecta deposits (Hörz et al. 1977). Grain size of this breccia, as well as the size of megablocks, and the abundance of stratigraphically older target rocks (i.e., from a deeper level of the transient cavity) decrease radially from the crater center, while the mass ratio of locally derived material vs. primary ejecta increase. In the size fraction < 10 mm, up to 90 vol.% local materials – Tertiary sands, shales, pebbles, and coal – has been observed. This relationship plays an important role in interpreting and understanding the material sampled on the Moon during the Apollo missions.

Large Proterozoic Impact Structures (Sudbury, Vredefort), and the Bushveld Enigma

Compared to other solid bodies in the solar system, the Earth comprises surprisingly few (<10) "old" (pre-Cambrian) impact structures. This is explained by the inherent dynamic nature – with both exogenic and endogenic forces – of our planet. Two of the preserved craters, Sudbury and Vredefort, however, are the largest terrestrial impact structures, and both are associated with world-class ore deposits.

Sudbury. The 1850 Ma Sudbury Structure (N 46°36′ W81°11′) which has been recently reviewed by Deutsch et al. (1995), represents the best example of a terrestrial multi-ring impact structure. Sudbury is superimposed on the Proterozoic Huronian Supergroup of the Southern Province and Archean basement rocks of the Superior Province. As depicted in Fig. 32, the structure covers an area of >15000 km^2. Proceeding inwards and stratigraphically upwards, three main geological formations directly related to the impact event have been identified at Sudbury: the brecciated crater floor, extending up to a distance of 80 km from the outer margin of the Sudbury Igneous Complex (SIC), which is part of the coherent impact melt sheet in the central inner ring of the structure, and the allochthonous breccia lens.

The crater floor consists of the Footwall rocks, transected irregularly by dikes of the so-called Sudbury Breccia. Four types of breccia dikes can be distinguished, differing in matrix characteristics (melt vs. clastic matrix), thickness, clast content, and contact relationship to the country rock. They are most abundant in an approximately 13 km wide zone adjacent to the SIC and in concentric zones at 20 to 33, 42 to 48, and 78 to 80 km distance from the North Range of the SIC. The size of some pseudotachylite dikes indicates an amount of displacement in the order of 1 km between individual blocks (Spray and Thompson 1995). Erosional remnants of the Huronian Supergroup are preserved in a ring-like graben zone parallel to the outer margin of the SIC at a distance of 20 to 25 km. At the basal contact of the SIC with the footwall, the polymict parautochthonous Footwall Breccia, which includes clasts of the Sudbury Breccia and contains sulfide ores, forms a narrow, irregular zone. Annealing of the breccia by the overlying impact melt layer resulted in partial melting of the fine-grained clastic material, which, according to orthopyroxene-clinopyroxene geothermometry, crystallized below 1040 °C.

The coherent impact melt sheet ranges from a clast-rich, discontinuous impact melt breccia, the Contact Sublayer, through the dominantly inclusion-free magmatic-textured Main Mass of the SIC, to a capping, extremely inclusion-rich impact melt breccia, the Basal Member of the Onaping Formation. Apophyses of the melt complex, the Offset Dikes, either emanate radially from the outer margin of the SIC up to a distance of at least 30 km, or form dikes concentric

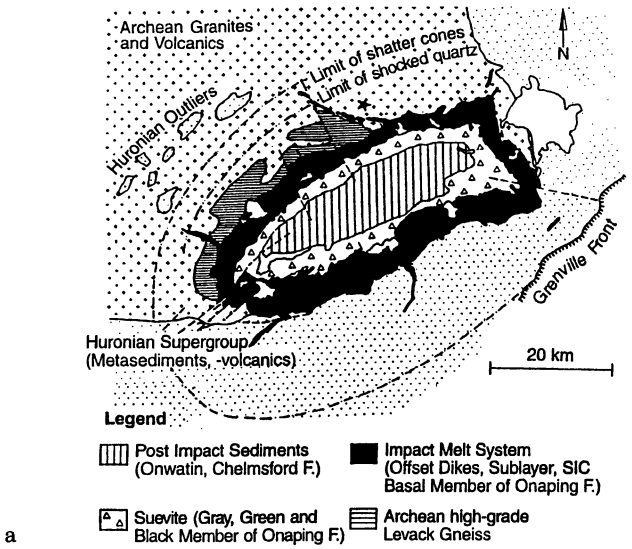

a

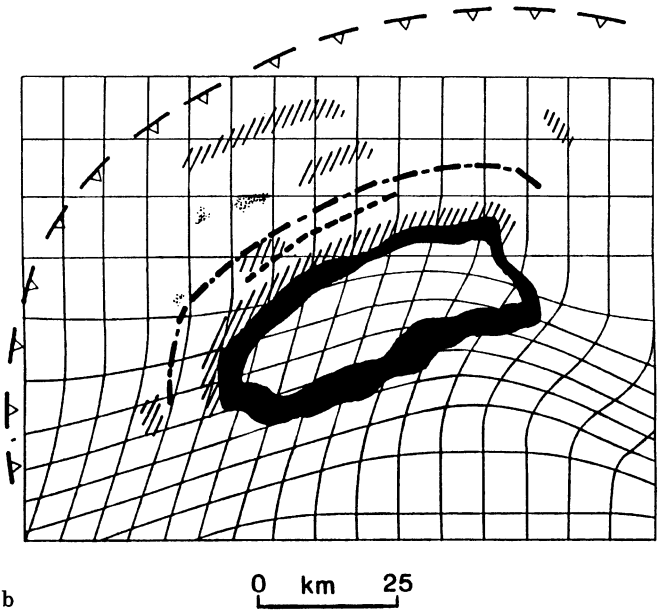

b

Fig. 32. **a** Geological sketch map showing the main lithological and stratigraphic units of the Sudbury Structure; ★ Foy Offset Dike; *stippled area* Southern Province; *crosses* Superior Province. The outer limits of occurrence shatter cones and decorated planar features in quartz ("shocked quartz") correspond to a shock pressure of about 2, and 6 to 7 GPa, respectively. Huronian outliers are downfaulted remnants of pre-impact cover rocks. **b** Sketch map of the Sudbury area showing radial limits north of the outer margin of the Sudbury Igneous Complex (SIC; *dark gray*) for decorated PDFs in quartz (*dashed lines*), shatter cones (*point-dash line*), the relic occurrence of downfaulted Huronian cover rocks (*light gray*) and zones with abundant Sudbury Breccia (*hatched*), and an estimate of the original outer rim of the final modified crater (*broken line with triangles*). The strain pattern, as estimated by Roest and Pilkington (1994), is given in *solid lines* which indicate the paleo-latitude and longitude lines.

to the SIC in the crater floor. The crystalline impact melt breccias of both the Contact Sublayer and the Offset Dikes contain abundant fragments of local material, as well as mafic to ultramafic inclusions, which are otherwise unknown at Sudbury. The up to 3.5 km thick Main Mass of the SIC consist of norites, a quartz-gabbro, and granophyres; it represents the central, differentiated part of the impact melt complex with an estimated volume of 1.0 to 2.5×10^4 km^3. The Basal Member contains up to 80 vol.% clasts of mainly Huronian metasediments in a crystalline matrix, which is the result of annealing by the underlying SIC.

The allochthonous breccia lens comprises fallback material, the Gray and the Green Member of the Onaping Formation (OF), whereas breccias of the topping, up to 1200-m-thick Black Member (OF) mark the onset of post-impact redepositional processes. These breccias are covered by the Onwatin and Chelmsford Formations, representing the sedimentary infill of the crater. The Gray Member is a suevite-like clastic matrix breccia with variably shocked clasts and irregularly shaped melt fragments, which displays flow structures, vesiculation, and a fine-grained crystalline texture. Huronian materials dominate amongst the fragments. The 5 to 70 m thick Green Member consists of fine-grained, often chloritized, clastic material and some larger lithic clasts embedded in a microcrystalline matrix. The unique texture of this impact melt breccia may have resulted from an agglomeration of melt particles and clastic debris deposited as fallback material.

The impact origin of the Sudbury Structure is substantiated by the occurrence of diagnostic shock indicators. These are Brazil twins and decorated PDFs in quartz, planar fractures in zircon of the Onaping breccias and footwall rocks, and shatter cones. Second-order features are huge pseudotachylite dikes and thick breccia sequences as well as fullerenes (C_{60} and C_{170}) occurring with an abundance of up to 10 ppm in Onaping breccias; these fullerenes were probably synthesized within the vapor plume (Becker et al. 1994). The present spatial distribution of impact-related formations and shock metamorphic effects, sketched in Fig. 32, has been used to constrain the original size of the Sudbury impact structure to approximately 250 km. This multi-ring impact basin was tectonized immediately after the impact and is now heavily eroded. Only the central depression inside the first ring is preserved, but remnants of additional rings are probably delineated by the four roughly semi-circular zones containing large bodies of Sudbury Breccia and pseudotachylites.

Solid arguments in support of the above outlined impact model are provided by structural, geophysical, geochemical, and geochronological investigations. High-precision U-Pb dating yields, within the given precision of +3.5/–2.6 Ma (2σ), an identical 1.85 Ga age for zircon and baddeleyite extracted from the Offset Dikes, the included ultramafic lithologies, and the SIC (e.g., Ostermann et al. 1996). These formations carry only newly crystallized grains, totally lacking shock features and inherited cores. The 1.85 Ga age is also recorded in heavily shocked zircons of the Onaping formation, titanite in the footwall south, and newly grown zircons in the basement north of the SIC, showing that

all formations, from the footwall up to the breccia layers, were either the product of or affected by the impact event.

All impact melt lithologies (coherent melt sheet, melt particles in the suevitic breccias) as well as mafic to ultramafic clasts in the Sublayer and the Offset Dikes display a strong geochemical affinity to crustal material. Slopes to the REE distribution patterns, which are bracketed by REE patterns for basement and cover rocks now exposed in the footwall, are steeply negative. Isotopic characteristics of the impact melt lithologies, with highly radiogenic initial Sr ratios, and $\varepsilon_{Nd}^{T=1.85\,Ga}$ ranging from −5 to about −9, correspond to those of local country, and, hence, target rocks. Nd model ages, relative to a depleted mantle source, of 2.7 Ga are identical with the true formation age of the crust in the Sudbury target area. In addition, osmium and lead isotope compositions of Cu-Ni ores in the Sublayer and Offset Dikes resemble values determined for local country rocks (e.g., Dickin et al. 1996). The geochemical features can be interpreted without particular requirement for an additional, 1.85 Ga mantle-derived component, and, therefore, strongly support an origin of the SIC by impact melting of crustal target lithologies. Further evolution of the SIC into a differentiated impact melt complex has not yet been modeled in detail. The present distribution with about 27 vol.% norites (mean SiO_2 content 56 wt.%), quartz-diorite (54 wt.% SiO_2), 63 vol.% of granophyric material (68 wt.% SiO_2), and the apparently abrupt geochemical transitions between the units, is currently best explained by the double diffusive convection system in the impact melt. The ores may have originated as immiscible sulfide droplets resulting from a decrease in sulfur solubility in the cooling siliceous impact melt sheet. Additional support for this simple model is provided by mass balance calculations, indicating that for the South Range a remixing of known ore bodies into the norite would raise its nickel content by only 10 ppm to about 90 ppm, which is well within the known range of nickel contents for Huronian metavolcanics in that area.

According to surface structural observations and a detailed geophysical survey within the frame of the LITHOPROBE transect, the present elliptical pattern of the SIC is the result of northwest-directed tectonic compression, which started immediately after the impact event and outlasted cooling of some impact formations. Deformation and tectonic displacement resulted in horizontal bulk shortening of the Sudbury Structure and exhumation of a lower level of the SIC in the south. After removing the effects of a simple NW-SE stress field, which is illustrated in Fig. 32b, the SIC could well have been originally circular with an estimated NW-SE diameter of about 60 to 65 km for the outer margin of the SIC at the present erosional level (Roest and Pilkington 1994). Seismic reflection data have revealed that the Levack Gneiss Complex and SIC layers of the North Range dip gently southward at 20 to 30° and appear continuous under the Sudbury Basin, with gradually increasing thickness towards the center. Indications for a magmatic plumbing system or feeder dikes are totally lacking. The now highly asymmetric SIC is rootless at depth, providing a very strong argument for the origin of the SIC by impact melting.

Vredefort. The circular 2023 Ma (Kamo et al. 1996) Vredefort structure (S 27°0′ E 27°30′) is the largest known terrestrial impact structure; for reviews see Grieve and Masaitis (1994) and Reimold and Koeberl (1994). As shown in Fig. 33, Vredefort consists of a central core of updomed Archean basement rocks with a diameter of about 36 km, rimmed by an approximately 18 km wide collar of steeply dipping to overturned Archean to Proterozoic sequences of the Witwatersrand and Ventersdorp Supergroups, and a roughly 28 km concentric synclinorium of the Proterozoic Transversal sequence. The southeastern half of the structure is covered by the Karoo sequence. The so-called Vredefort Dome is considered as the deeply eroded remnant of a large, complex impact structure with only the crater floor preserved. Taking an erosion of about 8 km into account, and using well-established relationships of the diameter of the uplifted area to the original crater diameter, the original rim-to-rim diameter of the Vredefort impact structure is estimated to be between 300 and 335 km (Therriault et al. 1996).

A variety of first- and second-order impact-related effects have been observed at Vredefort, e.g., extraordinary occurrences of pseudotachylites (Vredefort is the type locality of "pseudotachylytes"), shatter cones, planar microstructures in quartz, and coesite and stishovite (Martini 1991). Planar microstructures, which have been the key issue on the controversy of endogenic vs. exogenic origin for Vredefort, represent closely spaced sets of mechanical Brazil twins (Leroux et al. 1994b). Compared to other complex impact structures, where residual shock effects in quartz document increasing shock levels towards the center, shocked quartz at Vredefort seemingly shows an irregular distribution, and lowest pressures have been calculated for the center. This particular observation is ascribed to post-impact thermal metamorphism in the uplifted core, which was caused by intrinsic heat plus residual thermal energy, deposited by the shock event; in addition, a significant heat transfer from the hot overlying melt sheet could be expected. The planar deformation features, i.e., amorphous lamellae, in quartz responded to this annealing with formation of decorated planar elements and, finally, total recrystallization obliterated the shock effects. Therefore, PDFs reflecting high shock pressures disappeared, whereas the more robust mechanical Brazil twins survived.

Pseudotachylites are concentrated in the collar rocks surrounding the central uplifted area, but also occur in this core, in the Witwatersrand Basin at a distance of about 80 km from the presumed crater center, as well as around Johannesburg. ^{39}Ar-^{40}Ar dating resulted in uniform 2 Ga ages for all pseudotachylite occurrences, although some gas loss due to later low-temperature annealing is recorded. The age identity serves as an independent argument for the large size of the Vredefort impact structure.

Impact melt lithologies at Vredefort are preserved only in the form of dike-like bodies of the so-called 2023 ± 4 Ma ($2\,\sigma$) bronzite granophyre, representing apophyses of the originally overlying massive impact melt layer into the crater basement. These dikes resemble the Offset Dikes at Sudbury. The geochemical composition of the granophyre has been successfully modeled by mixing of

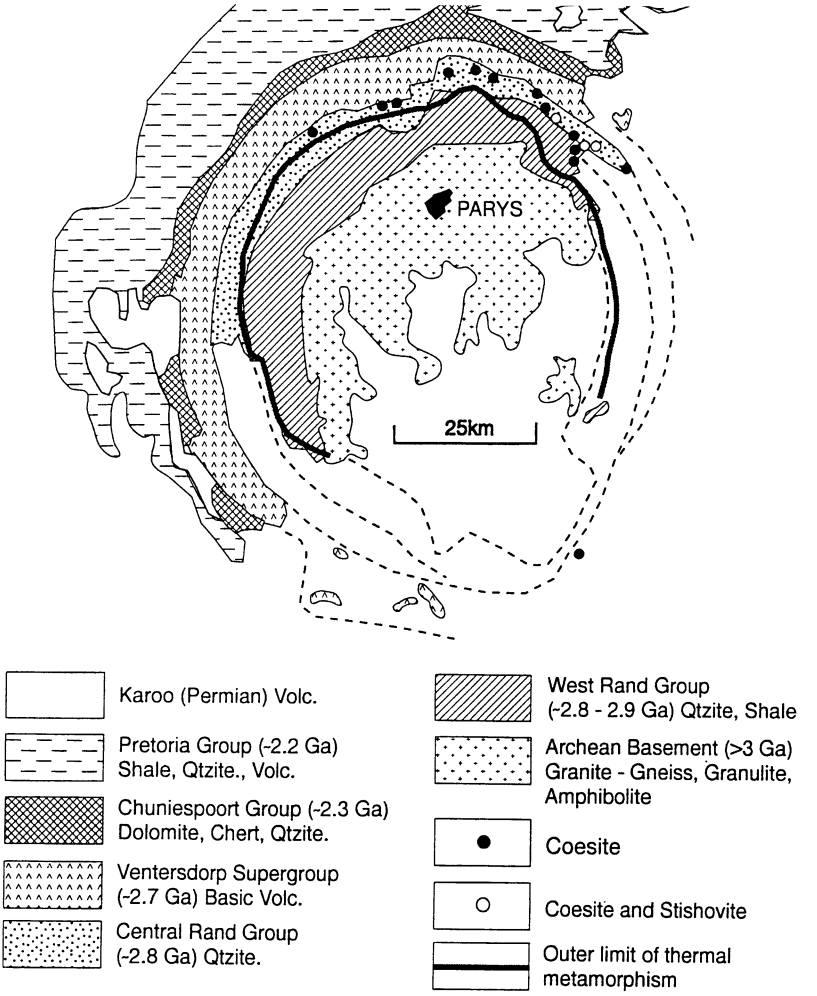

Fig. 33. Geological sketch map of the central part of the Vredefort impact structure. Qtzite = quorzite, Volc = volcanics. (After Martini 1991 and Grieve et al. 1996)

lithologies which constitute the lower part of the Vredefort target stratigraphy. In addition, Re-Os systematics indicate the presence of a meteoritic component.

The incredibly rich gold fields of the Witwatersrand Basin, accompanied by extremely valuable deposits of detrital uranite, occur in an 180° arc within the estimated original diameter of the Vredefort structure. Preservation of these progenetic sedimentary deposits is due to downdropping of higher stratigraphic levels of the target within an annulus surrounding the central uplift (Grieve and Masaitis 1994).

Bushveld Complex. Geological setting, geochemical and petrographic characteristics of the 2055±4 Ma (2 σ) (Kamo et al. 1996) Bushveld Complex, South Africa, have been reviewed recently by von Gruenewaldt and Harmer (1992). The extended and ore-rich Bushveld Complex covers an area of 65 000 km^2. It consists of the mafic to ultramafic, up to 7.5 km thick Rustenberg layered sequence, which is overlain by large volumes of granites and granophyres forming the up to 5 km thick Lebowa sheeted granite suite. Divided into a western and eastern compartment, the mafic series, with an estimated volume of 500 000 km^3, crop out in up to 40 km wide and at least 400 km striking arcuate belts. On both lobes, the layered sequence is slipping at low angels towards the center of the whole complex. The Bushveld Complex is topped by the Rooiberg Group, ranking amongst the largest known accumulations of felsites, with a volume of about 300 000 km^3. This siliceous, massive, and quite uniform sequence shows features suggestive of high emplacement temperatures (>850 °C). Stratigraphically, the Rooiberg Group is considered equivalent to the Stavoren granophyre of the Dullstrooom Formation, forming locally the floor of the layered suite, and, hence, considered as pre-dating the Bushveld Complex, though perhaps separated by only a very short time span. Both the granophyres, the Rustenberg and the Lebowa Suites, are not dated with the required precision to resolve the chronostratigraphic framework in detail. Published ages overlap within given errors, being typically on the order of 10 to 30 M (2 σ).

Since 1956, it has been repeatedly suggested that the Bushveld Complex could have originated due to simultaneous multiple impact events, although a self-consisting impact model taking into account and explaining all observational features has not yet been outlined. Main arguments in support of this presumption rest so far on quite speculative morphological interpretations, as well as on textural and geochemical properties of the Rooiberg felsites, which have been interpreted as impact melt (Elston 1992). Quartz grains throughout the Rooiberg Group display slightly curved microstructures with a typical spacing of >15 μm, which microscopically resemble deformation structures in quartz of tectonic shear zones. Despite intense field work and elaborate petrographic investigations, conclusive shock indicators such as residual shock features in quartz have not been reported from the Bushveld area (Joreau et al. 1997).

The impact hypothesis is at odds with the widely accepted interpretation that the Bushveld Complex represents the world's largest layered intrusion with an intracratonic setting, possibly emplaced in a rifted environment. Several geochemical data, however, are not well understood at the moment. Amongst these, highly radiogenic Sr, Pb, Os isotope ratios, and heavy oxygen isotope compositions have to be mentioned. For example, $^{86}Sr/^{86}Sr$ ratios recalculated to 2.05 Ga, range for most Bushveld lithologies from 0.7056 to about 0.709, compared to 0.7022 for a "normal mantle" having bulk Earth character. The initial ε_{Nd} value for the layered sequence is highly negative with −6, and the Nd model age relative to CHUR is about 3.5 Ga, corresponding to the true age of the oldest basement rocks of the northeastern Kapvaal craton. For one

Rooiberg high-magnesian felsite, a Nd model age of 3.4 Ga relative to a depleted mantle has been published. The data exclude a direct origin of the named elements from the contemporaneous bulk mantle, and are currently interpreted as evidence for (1) mixing of magmas derived from at least two mantle domanes with a highly complicated multistage pre-Bushveld history, and (2) contamination of the Bushveld material by crustal lithologies. Calculated amounts of assimilation vary between 10% for oxygen and up to 60% for Os (Hart and Kinloch 1989).

To conclude, an impact origin of the Bushveld Complex cannot be totally ruled out, but solid evidence for this assumption is lacking (e.g., French 1990). Taking the lessons from the development of the impact concept at the Sudbury Structure into account, a thorough reassessment of the vaguely defined impact hypothesis for the Bushveld Complex requires more elaborate geochemical work, e.g., systematic Nd isotope analyses, and high-precision dating. A detailed geochronological frame is one important step to foster or discard any impact model for the Bushveld area or part of it. Field and labor work should concentrate on the discovery of diagnostic residual shock effects, truly related to the Bushveld Complex. It must be taken into account, however, that the volume of impact melt increases relative to the volume of the transient cavity, causing obliteration shock effects which are documented at smaller terrestrial impact structures (Grieve and Cintala 1992).

Impact diamonds at the Popigai Impact Structure

V. L. Masaitis

The Popigai impact structure is located in northwest Siberia on the northern edge of the Archean Anabar shield, which is, in part, covered by Upper Proterozoic to Cretaceous sedimentary rocks. The Popigai impact event occurred about 35.7 ± 0.2 Ma (2σ) ago (Bottomley et al. 1997). Popigai may be regarded as a multi-ring impact structure with a diameter of about 100 km (Masaitis et al. 1975; Masaitis 1994). It consists of an about 45 km wide central depression, encircled by an uplifted ring of shocked gneisses, which, in turn, is surrounded by the ring through. This through and the central depression are filled by allogenic (allochthonous) impact breccias and impact melt rocks, reaching a maximum thickness of about 2.5 km.

The allogenic breccia consists of large blocks and fragments of crystalline and sedimentary rocks, and occupies the lower part of the crater filling. Many fragments display shatter cones and petrographical features of shock metamorphism, including the presence of coesite and stishovite. Coherent, up to some 100 m thick sheets of massive tagamites overlap the breccia. Tagamites also occur as irregular bodies in suevitic breccias (suevites), which are widely distributed in the upper part of the crater fill. Small patches of breccias and taga-

mites are preserved as relics of the ejecta blanket outside the crater depression. Tagemites and suevitic breccias originated by impact melting and partial dissipation of melt have a chemical composition identical to that of basement gneisses. Tagamites containing numerous clasts of shocked rocks and minerals show either a glassy or a crystalline matrix with plagioclase and pyroxene as main constituents. Suevites are made up of fragments and bombs of chilled impact glass with an admixture of rock debris. The impact melt rocks are enriched by Ni, Co, and Ir due to contamination of projectile material presumed to be composed of ordinary chondrite.

The Popigai crater is the place where, at the beginning of the 1970s, impact diamonds have been found for the first time directly in shocked and impact-melted rocks (Masaitis et al. 1972). Impact diamonds originated from martensitic transformation of graphite, which is a rock-forming mineral in garnet-biotite gneisses of the Popigai target lithologies. Impact diamonds differ from the well-known diamonds in kimberlites, and occur as irregular grains and tabular paracrystals; they are very rarely colorless, and mostly yellow, gray, or black. The largest grains may reach 10 mm, but the average dimension of the diamonds is 0.5–2 mm. Tabular paracrystals inherit the crystallographic shape of the precursor graphite, especially the pinacoid faces $\{0001\}$. However, the angles between the prismatic $\{10\bar{1}0\}$ faces of the paracrystals are distorted due to the anisotropy of compressibility of graphite. The inherited twinning striation is common for pinacoid faces, but some planar fissures observed on them may be caused by shock deformation. Grains and paracrystals of impact diamonds display dissolution patterns, the honeycomb microrelief on their surfaces being caused by phase inhomogeneities.

X-ray studies showed that paracrystals mainly consist of two microcrystalline phases: the spinel law cubic phase (diamond) and the hexagonal high-pressure phase (lonsdaleite), whose content in paracrystals may reach 50%, some remnant or secondary graphite may be present as well. The size of the single microcrystals of these high-pressure phases is about 5×10^{-4} cm or less. The polycrystalline aggregate is structured: the pinacoid of paracrystals, i.e., the (0001) plane of the precursor graphite, corresponds to the (111) plane of the cubic phase and is perpendicular to the (0001) plane of lonsdaleite. According to the optical properties, paramorphs imitate monocrystals of non-cubic symmetry. In some cases, the paracrystals display transparency, strong birefringence (up to 0.02) and usually total straight extinction. Sometimes, the twinning of paracrystals is inherited from Veselovsky twins of the precursor graphite.

The density of impact diamonds varies due to the admixture of graphite and minerals and glasses from the host rocks, but some paracrystals are characterized by anomalous density (up to 3.61 g cm^{-3}) which is higher than the X-ray density of cubic diamond. Inclusions in impact diamonds are graphite, alumosilicat glasses, silica-glass, and Fe-oxide; diamond paramorphs exhibit a minor admixture of Si, Ti, Al, Na, Ca, similar to that observed in the precursor graphite.

Spectra of combinative dispersion display intensive widening of the Raman line at 1332 cm^{-1} (up to 30 times that of endogenic diamonds), which reflects

the degree of defectivity of polycrystals. Photoluminescence spectra are characterized by systems of non-phonon lines in the interval 650–780 nm and the absence of the defect represented by the 640-nm line. These data and the study of IR spectra may indicate the presence of N-centers of absorption as well as centers caused by the presence of CO_2 and H_2O. In UV light, impact diamonds usually have orange-red luminescence. The carbon isotope composition of the precursor graphite and the impact diamonds is identical, ranging from –12 to –17 ‰ $\delta^{13}C$.

Impact diamonds occur as accessories in tagamites and suevites, as well as in fragments of strongly shocked gneisses (protoimpactites). In these graphite-bearing rocks, all minerals are diaplectic or transformed into shock-fused monomineralic glasses; diamonds included is such lithologies may be regarded as authigenic. The study of shock features in all silicate minerals of these protoimpactites indicates a pressure of about 34–36 GPa for the onset of the transformation from graphite to diamond; the transformation is complete at a pressure of about 60 GPa. The degree of transfer is presumed to be controlled not only by the maximum shock pressure but also by the duration of the compression as well as the crystal orientation relative to the front of the shock wave.

There are some regularities in the distribution of diamonds in the impactites within the Popigai crater. Some radial zones are enriched with diamonds due to azimuthal inhomogeneities in the distribution of graphite in target rocks, superimposed by the concentric zoning of shock metamorphism. The primary distribution of shock-induced high-pressure carbon phases was disturbed by the radial ejection of melted material with a different diamond content. The preservation of diamonds from oxidation and graphitization depended on the post-shock temperature of the ejected material and its cooling rate after deposition. The overheated fractions of melt appear to be virtually barren of diamonds after chilling.

Modern placers of impact diamonds adjacent to Popigai originated as a result of impactite disintegration and redeposition. Single grains of impact diamonds were found at a distance of about 100–150 km from the crater rim, which suggested that they are relics of totally rewashed distal ejecta.

In terms of energy source and ore formation mechanism, the primary deposits of impact diamonds belong to an absolutely new category of economic minerals and are basically different from sedimentogenic, magmatogenic, metamorphogenic, and other concentrations of mineral raw materials generated in the Earth's crust and on its surface. At present, similar impact diamonds have been found in other impact structures originating in graphite-bearing target rocks (Ries, Kara, Puchezh-Katunki, Terny, Zapadnaya astroblemes). Thus, impact diamonds may be widely distributed, and finds of this material in placer deposits indicate the rewashing of impactites of some buried or strongly eroded craters. Although the lonsdaleite phase has not yet been established in carbonados occurring in placer deposits in Central Africa and Brazil, there is a supposition that this type is polycrystalline diamond originated in the Precambrian by large impacts on a carbon-bearing target. However, preliminary TEM

observations seem to disprove this hypothesis (see above: High-Pressure Polymorphs).

Impact diamonds may be regarded as a criterion for the impact origin of lava-like or tuff-like rocks, where they can be found similarly to the high-pressure phases, coesite and stishovite. Their presence in any thin layer in the sedimentary sequence may be caused by dust-cloud transport, indicating a synchronous impact event to have occurred in some distant region.

Special investigations and commercial tests showed that polycrystalline impact diamonds from the Popigai crater are occasionally superior to the kimberlite ones in a number of properties, in particular in resistance to destructing load. Light-colored impact diamonds are the strongest, which allows them to be used for drills and other abrasive tools. Apographitic impact diamonds represent a new type of industrial diamond raw material, which offers a number of advantages over the well-known types of natural and synthetic diamonds. The economic value of this industrial impact diamond deposit may be significant, taking into account the high content of this mineral in impactites, and the very large resources of ores ensured by the widespread occurrences of diamond-bearing rocks at Popigai.

References

Agrinier P, Boyd SR, Martinez I, Schärer U, Javoy M, Deutsch A (1995) On the kinetics of $CaO + CO_2 \Rightarrow CaCO_3$ and CO_2 released during impact processes. Ann Geophys 13 Suppl III C:738

Ahrens TJ, Gaffney ES (1971) Dynamic compression of enstatite. J Geophys Res 76:5504–5514

Allen CC, Gooding JL, Keil K (1982) Hydrothermally altered impact melt rock and breccia: contributions to the soil of Mars. J Geophys Res 87:10,083–10,101

Ashworth JR, Schneider H (1985) Deformation and transformation in experimentally shock-loaded quartz. Phys Chem Min 11:241–249

Barber DJ, Wenk HR (1979) Deformation twinning in calcite, dolomite, and other rhombohedral carbonates. Phys Chem Min 5:141–165

Becker L, Bada JL, Winans RE, Hunt JE, Bunch TE, French BM (1994) Fullerenes in the 1.85 billion-year-old Sudbury Impact Structure. Science 265:642–645

Beran A, Koeberl C (1996) Water in tektites and impact glasses by FTIR Spectrometry. Meteoritics Planet Sci 32:211–216

Bischoff A, Stöffler D (1984) Chemical and structural changes induced by thermal annealing of shocked feldspar inclusions in impact melt rocks from Lappajärvi crater, Finland. J Geophys Res 89:B645–B656

Blum JD, Papanastassiou DA, Koeberl C, Wasserburg GJ (1992) Neodymium and strontium isotopic study of Asutralasian tektites: new constraints on the provenance and age of target materials. Geochim Cosmochim Acta 56:483–492

Bohor BF, Foord EE, Modreski PJ, Triplehorn DM (1984) Mineralogical evidence for an impact event at the Cretaceous-Tertiary boundary. Sience 224:867–869

Bohor BF, Betterton WJ, Krogh TE (1993) Impact shocked zircons: discovery of shock-induced textures reflecting increasing degrees of shock metamorphism. Earth Planet Sci Lett 119:419–424

Boslough MB (1991) Shock metamorphism and chemistry and planetary geologic processes. Ann Rev Earth Planet Sci 19:101–130

Bottomley RJ, Grieve RAF, York D, Masaitis VL (1997) The age of the Popigai impact event and its relation to events at the Eocene/Oligocene boundary. Nature 388:365–368
Brett R (1992) The Cretaceous-Tertiary extinction: a lethal mechanism involving anhydrite target rocks. Geochim Cosmochim Acta 56:3603–3606
Bringemeier D (1994) Petrofabric examination of the main suevite of the Otting quarry, Nördlinger Ries, Germany. Meteoritics 29:417–422
Buchanan PC, Reimold WU (1996) Analysis of deformation lamellae in quartz grains from the Rooiberg felsite, Bushveld Complex, South Africa, and associated rocks. Lunar Planet Sci Conf XXVII: 175–176
Carlisle DB, Braman DR (1991) Nonometre-size diamonds in the Cretaceous/Tertiary boundary clay of Alberta. Nature 352:708–709
Carstens H (1975) Thermal history of impact melt rocks in the Fennoscandian shield. Contrib Mineral Petrol 50:145–155
Carter NL (1965) Basal quartz deformation lamellae, a criterion for recognition of impactites. Am J Sci 263:786–806
Carter NL, Avé Lallemant HG (1970) High temperature flow of dunite and peridotite. Geol Soc Am Bull 81:2181–2202
Chen G, Tyburczy JA, Ahrens TJ (1994) Shock-induced devolatilization of calcium sulfate and implications for K-T extinctions. Earth Planet Sci Lett 128:615–628
Chen M, Sharp TG, El Goresy A, Wopenka B, Xie X (1996) The majorite-pyrope + magnesio-wüstite assemblage: constraints on the history of shock veins in chondrites. Science 1271:1570–1573
Cintala MJ, Grieve RAF (1994) The effects of differential scaling of impact melt and crater dimensions on lunar and terrestrial craters: some brief examples. In: Dressler BO, Grieve RAF, Sharpton VL (eds) Large meteorite impacts and planetary evolution. Geol Soc Am Spec Pap 293:51–59
Clarke RS, Appleman DE, Ross DR (1981) An antarctic iron meteorite contains preterrestrial impact-produced diamond and Ionsdaleite. Nature 291:396–398
Cordier P, Doukhan JC (1989) Water solubility in quartz and its influence on ductility. Eur J Mineral 1:221–237
Cummings D (1964) Kink-bands: shock deformation of biotite resulting from a nuclear explosion. Science 148:950–952
Dachille F, Gigl P, Simons PY (1968) Experimental and analytical studies of crystalline damage useful for the recognition if impact structures. In: French BM, Short NM (eds) shock metamorphism of natural materials. Mono Book Corp, Baltimore, Maryland, pp 555–570
DeCarli PS, Jamieson JC (1961) Formation of diamond by explosive shock. Science 133:1821–1822
Deribas AA, Dobretsov NL, Kudinov VM, Zyuzin NI (1966) Shock compression of SiO_2 powders. Dokl Akad Nauk USSR 168:127–130
Deutsch A, Schärer U (1994) Dating terrestrial impact events (invited review). Meteoritics 29: 301–322
Deutsch A, Buhl D, Langenhorst F (1992) On the significance of crater ages – new ages for Dellen (Sweden) and Araguainha (Brazil). Tectonophysics 216:205–218
Deutsch A, Grieve RAF, Avermann M, Bishoff L, Brockmeyer P, Buhl D, Lakomy R, Müller-Mohr V, Ostermann M, Stöffler D (1995) The Sudbury structure (Ontario, Canada): a tectonically deformed multi-ring impact basin. Geol Rundsch 84:697–709
Deutsch A, Ostermann M, Masaitis VL (1997) Geochemistry and Nd-Sr isotope signature of tektite-like objects (Urengoites, South-Ural glass). Meteoritics Planet Sci 32:679–686
Dickin AP, Artan MA, Crocket JH (1996) Isotopic evidence for distinct crustal sources of North and South Range ores, Sudbury Igneous Complex. Geochim Cosmochim Acta 60:1605–1613
El Goresy A, Fechtig H, Ottermann J (1968) The opaque minerals in impactite glasses. In: French BM, Short NM (eds) Shock metamorphism of natural materials. Mono Book Corp, Baltimore, Maryland, pp 531–553

Elston WE (1992) Does the Bushveld-Vredefort system (South Africa) record the largest known terrestrial impact catastrophe? Int Conf on Large meteorite impacts and planetary evolution. Sudbury LPI Contrib No 790:23–24
Evans NJ, Gregoire DC, Grieve RAF, Goodfellow WD, Veizer J (1993) Use of platinum-group elements for impactor identification: terrestrial impact craters and Cretaceous-Tertiary boundary. Geochim Cosmochim Acta 57:3737–3748
Feldman VI (1994) The conditions of shock metamorphism. In: Dressler BO, Grieve RAF, Sharpton VL (eds) Large meteorite impacts and planetary evolution. Geol Soc Am Spec Pap 293:121–132
Floran RJ, Grieve RAF, Phinney WC, Warner JL, Simonds CH, Blanchard DP, Dence MR (1978) Manicouagan impact melt Quebec 1 stratigraphy petrology and chemistry. J Geophys Res 83:2737–2759
Fregerslev S, Carstens H (1976) FeNi metal in impact melt rocks of Lake Lappajärvi, Finland, Contrib Mineral Petrol 55:255–263
French BM, Short NM (1968) Shock metamorphism of natural materials. Mono Book Corp, Baltimore, Maryland, 644 pp
French BM (1990) Absence of shock-metamorphic effects in the Bushveld Complex, South Africa: results of an intensive search. Tectonophysics 171:287–301
Frondel C, Marvin UB (1967) Lonsdaleite, a hexagonal polymorph of diamond. Nature 214:587
Gersonde R, Kyte FT, Bleil U, Diekmann B, Flores JA, Gohl K, Grahl G, Hagen R, Kuhn G, Sierro FJ, Voelker D, Abelmann A, Bostwick JA (1997) Geological record and reconstruction of the late Pliocere impact of the Eltanin asteroid in the Southern Ocean. Nature 390:357–363
Gilmour I, Russell SS, Arden JW, Lee MR, Franchi IA, Pillinger CT (1992) Terrestrial carbon and nitrogen isotopic ratios from Cretaceous-Tertiary boundary nanodiamonds. Science 258:1624–1626
Goltrant O, Cordier P, Doukhan JC (1991) Planar deformation features in shocked quartz: a transmission electron microscopy investigation. Earth Planet Sci Lett 106:103–115
Goltrant O, Leroux H, Doukhan JC, Cordier P (1992) Formation mechanism of planar deformation features in naturally shocked quartz. Phys Earth Planet Int 74:219–240
Gostin VA, Keays RR, Wallace MW (1989) Iridium anomaly from the Acraman impact ejecta horizon: impacts can produce sedimentary iridium peaks. Nature 340:542–544
Gratz AJ, Nellis WJ, Christie JM, Brocious W, Swegle J, Cordier P (1992) Shock metamorphism of quartz with initial temperatures −170 to +1000 °C. Phys Chem Min 19:267–288
Graup G (1978) Das Kristallin im Nördlinger Ries. Petrographische Zusammensetzung und Auswurfsmechanismus der kristallinen Trümmermassen, Struktur des kristallinen Untergrundes und Beziehungen zum Moldanubikum. Enke, Stuttgart, 190 pp
Grieve RAF (1978) The melt rocks at Brent crater, Ontario, Canada. Proc Lunar Planet Sci Conf 9th: 2579–2608
Grieve RAF (1987) Terrestrial impact structures. Annu Rev Earth Planet Sci 15:245–270
Grieve RAF (1991) Terrestrial impact: the record in the rocks. Meteoritics 26:175–194
Grieve RAF (1997) Extraterrestrial impact events: the record in the rocks and the stratigraphic column. Palaeogeo. Paleoclimat. Palaeoecol. 132, 5–23
Grieve RAF, Cintala MJ (1992) An analysis of differential impact melt-crater scaling and implications for the terrestrial impact record. Meteoritics 27:526–538
Grieve RAF, Masaitis VL (1994) The economic potential of terrestrial impact craters. Int Geol Rev 36:105–151
Grieve RAF, Shoemaker EM (1994) The record of past impacts on Earth. In: Gehrels T (ed) Hazards due to comets and asteroids. University of Arizona Press, Tucson, pp 417–462
Grieve RAF, Langenhorst F, Stöffler D (1996) Shock metamorphism of quartz in nature and experiment: II. Significance in geoscience. Meteoritics Planet Sci 31:6–35
Gudlaugsson ST (1993) Large impact crater in the Barents Sea. Geology 21:291–294
Gurov EP, Gurova EP (1991) Geological structure and composition of rocks in impact craters. Nauka Press, Kiev (in Russian)

Gurov EP, Melnychuk EV, Metalidi SV, Ryabenko VA, Gurova EP (1985) The characteristics of the geological structure of the eroded astrobleme in the western part of the Ukrainian Shield. Dopovidi Akad Nauk Ukrainskoi Radyanskoi Sotsialisychnoi Republiky, Seriya B:8–11 (in Russian)

Hannemann RE, Strong HM, Bundy FP (1967) Hexagonal diamonds in meteorites: implications. Science 155:995–997

Hanss RE, Montaque BR, Davis MK, Galindo C, Hörz F (1978) X-ray diffractometer studies of shocked materials, Proc Lunar Planet Sci Conf IX:2773–2787

Hart SR, Kinloch ED (1989) Osmium isotope systematics in Witwatersrand and Bushveld ore deposits. Econ Geol 84:1651–1655

Hörz F (1968) Statistical measurements of deformation structures and refractive indices in experimentally shock-loaded quartz. In: French BM, Short NM (eds) Shock metamorphism of natural materials. Mono Book Corp, Baltimore, Maryland, pp 243–254

Hörz F, Quaide WL (1972) Debye-Scherrer investigations of experimentally shocked silicates. Moon 6:45–82

Hörz F, Gall H, Hüttner R, Oberbeck VR (1977) Shallow drilling in the Bunte Breccia impact deposits, Ries Crater, Germany. In: Roddy DJ, Pepin RO, Merrill RB (eds) Impact and explosion cratering. Pergamon Press, New York, pp 425–448

Hörz F, See TH, Murali AV, Blauchard DP (1989) Heterogeneous dissemination of projectile materials in the impact melts from Wabar Crater, Saudi Arabia. Proc Lunar Sci Conf IXX:697–709

Ivanov BA (1995) Geomechanical models of impact cratering: Puchezh-Katunki structure. In: Dressler BO, Grieve RAF, Sharpton VL (eds) Large meteorite impacts and planetary evolution. Geol Soc Am Sec Pap 293:81–91

Jahn BM, Floran RJ, Simonds CH (1978) Rb-Sr isochron age of the Manicouagan melt sheet Quebec, Canada. J Geophys Res 83:2799–2803

Jakubith M, Hornemann U (1981) Majorite formation from enstatite by experimental shock-loading. Phys Earth Planet Int 27:95–99

Joreau P, Reimold WU, Robb LJ, Doukhan JC (1997) A TEM study of deformed quartz grains from volcaniclastic sediments associated with the Bushveld Complex, South Africa. Eur J Mineral 9:393–401

Kamo SL, Reimold WU, Krogh TE, Colliston WP (1996) A 2.023-Ga age for the Vredefort impact event and a first report of shock-metamorphosed zircons in pseudotachylitic breccias and granophyre. Earth Planet Sci Lett 144:369–387

Kargel JS, Coffin P, Kraft M, Lewis JS, Moore C, Roddy D, Shoemaker EM, Wittke JH (1996) Systematic collection and analysis of meteoritic materials from Meteor Crater, Arizona. Lunar Planet Sci Conf XXVII:645–646

Kieffer SW, Phakey PP, Christie JM (1976) Shock processes in porous quarzite: transmission electron microscope observations and theory. Contrib Mineral Petrol 59:41–93

Kirby SH, Christie JM (1977) Mechanical twinning in diopside $Ca(Mg,Fe)Si_2O_6$: structural mechanism and associated crystal defects. Phys Chem Min 1:137–163

Kitamura M, Goto T, Syono Y (1977) Intergrowth textures of diaplectic glass and crystal in shock-loaded P-anorthite. Contr Mineral Petrol 61:299–304

Kleinmann B (1969) The breakdown of zircon observed in the Libyan desert glass as evidence of its impact origin. Earth Planet Sci Lett 5:497–501

Koeberl C (1990) The geochemistry of tektites: an overview. Tectonophysics 171:405–422

Koeberl C, Reimold WU (1995) Early Archaean spherule beds in the Barberton Mountain Land, South Africa: no evidence for impact origin. Precambrian Res 74:1–33

Koeberl C, Shirey SB (1996) Re-Os systematics as a diagnostic tool for the study of impact craters and distal ejecta. Palaeogeo. Paleoclimat. Palaeoecol. 132, 25–46

Kyte FT, Bohor BF (1995) Nickel-rich magnesiowüstite in Cretaceous/Tertiary boundary spherules crystallized from ultramafic, refractory silicate liquids. Geochim Cosmochim Acta 59:4967–4974

Kyte FT, Bostwick JA (1995) Magnesioferrite spinel in Cretaceous/Tertiary boundary sediments of the Pacific basin: remnants of hot, early ejecta from the Chicxulub impact? Earth Planet Sci Lett 132:113–127

Lambert P, Mackinnon IDR (1984) Micas in experimentally shocked gneiss. J Geophys Res 89:B685–B699

Lange MA, Lambert P, Ahrens TJ 81985) Shock effects on hydrous minerals and implications for carbonaceous meteorites. Geochim Cosmochim Acta 49:1715–1726

Langenhorst F (1989) Experimentally shocked plagioclase: changes of refractive indices and optic axial angle in the 10–30 GPa range. Meteoritics 24:291

Langenhorst F (1994) Shock experiments on α- and β-quartz: II. X-ray investigations. Earth Planet Sci Lett 128:683–698

Langenhorst F (1996) Characteristics of shocked quartz in late Eocene impact ejecta from Massignano (Ancona, Italy): Clues to shock conditions and source crater. Geology 24: 487–490

Langenhorst F (1997) Impaktdiamanten als Zeugen des Bombardements aus dem All. Humboldt-Spektrum, Humboldt-Universität zu Berlin, Heft 2/97, 32–37

Langenhorst F, Deutsch A (1994) Shock experiments on preheated α- and β-quartz: I. Optical and density data. Earth Planet Sci Lett 125:407–420

Langenhorst F, Joreau P, Doukhan JC (1995) Thermal and shock metamorphism of the Tenham meteorite: a TEM examination. Geochim Cosmochim Acta 59:1835–1845

Leroux H, Doukhan JC, Langenhorst F (1994a) Microstructural defects in experimentally shocked diopside: a TEM characterization. Phys Chem Min 20:521–530

Leroux H, Reimold WU, Doukhan JC (1994b) A TEM investigation of shock metamorphism in quartz from the Vredefort dome, South Africa. Tectonophysics 230:223–239

Lipschutz ME (1964) Origin of diamonds in the ureilites. Science 143:1431–1434

Madon M, Poirer JP (1983) Transmission electron microscope observation of α, β and $(Mg,Fe)_2SiO_4$ in shocked meteorites: planar defects and polymorphic transitions. Phys Earth Planet Int 33:31–44

Manghnani MH, Syono Y (1987) High-pressure research in mineral physics. Geophysical Monograph 39, American Geophysical Union

Margolis S, Claeys Ph, Kyte FT (1991) Microtektites, microcrystites and spinels from a late Pliocene asteroid impact in the Southern Ocean. Science 251:1594–1597

Martinez I, Schärer U, Guyot F (1993) Impact-induced phase transformations at 50–60 GPa in continental crust: an EPMA and ATEM study. Earth Planet Sci Lett 119:207–223

Martinez I, Agrinier P, Schärer U, Javoy M (1994) CO_2 production by impact into carbonates? A SEM-ATEM and stable isotope (^{18}O, ^{13}C) study of carbonates from the Haughton impact crater. Earth Planet Sci Lett 121:559–574

Martinez I, Deutsch A, Schärer U, Ildefonse Ph, Guyot F, Agrinier P (1995) Shock recovery experiments on dolomite and thermodynamical modeling of impact-induced decarbonation. J Geophys Res 100, B8:15,465–15,476

Martini JEJ (1991) The nature, distribution and genesis of the coesite and stishovite associated with the pseudotachylite of the Vredefort Dome, South Africa. Earth Planet Sci Lett 103:285–300

Masaitis VL (1993) Origin of the Sudbury Structure from the points of new petrographic mineralogical and geochemical data. Trans All-Russian Mineral Soc 122:1–17 (in Russian)

Masaitis VL (1994) Impactites from the Popigai crater. In: Dressler BO, Grieve RAF, Sharpton VL (eds) Large meteorite impacts and planetary evolution. Geol Soc Am Spec Pap 293:153–162

Masaitis VL, Mashchak MS (1996) Recrystallization and blastesis of shock-metamorphozed rocks in impact structures. Proc Russ Mineral Soc CXXV:1–18

Masaitis VL, Futergendler DI, Gnevushev MA (1972) Diamonds in impactites of the Popigay meteorite crater. Zap Vsesoyuznogo Mineralogicheskogo Obshchestva 101:108–112

Masaitis VL, Mikhailov MV, Selivanovskaya TV (1975) Popigai meteorite crater. Nauka, Moscow, 124 pp

Masaitis VL, Danilin AI, Mashchak MS, Raikhlin AI, Selivanovskaya TV, Shadenkov EM (1980) The geology of astroblemes. Nedra Press, St Petersburg, USSR, Russia, 231 pp (in Russian)

Masaitis VL, Mashchak MS, Naumol MV, Orlovo JV, Selivanovskaya TV (1995) Puchezh-Katunki impact crater: main features of geological structure. Doklady Ac Si 342:358–360

McLaren AC, Phakey PP (1966) Electron microscope study of Brazil twin boundaries in amethyst quartz. Phys Stat Sol 13:413–422

Melosh HJ (1989) Impact cratering. A geological process. Oxford University Press, New York, 245 pp

Melosh HJ, Vickery AM (1991) Melt droplet formation in energetic impact events. Nature 350:494–497

Milton DJ, De Carli P (1963) Maskelynite: formation by explosive shock. Science 140:670–671

Morgan J, Warner M and the Chicxulub working group (1997) Size and morphology of the Chicxulub impact crater. Nature 390, 472–476

Mori H (1994) Shock-induced phase transformations of the Earth and planetary materials. J Mineral Soc Jpn 23:171–178

Müller WF (1993) Thermal and deformation history of the Shergotty meteorite deduced from clinopyroxene microstructure. Geochim Cosmochim Acta 57:4311–4322

Müller-Mohr V (1992) Breccias in the basement of a deeply erode impact structure Sudbury Canada. Tectonophysics 216:219–226

Newsom HE, Graup G, Sewards T, Keil K (1986) Fluidization and hydrothermal alteration of the suevite deposit at the Ries crater, West Germany, and implications for Mars. J Geophys Res 91:E239–E251

Nishiizumi K, Kohl CP, Shoemaker EM, Arnold JR, Klein J, Fink D, Middleton R (1991) In situ ^{10}Be-^{26}Al exposure ages at meteor Crater, Arizona. Geochim Cosmochim Acta 55:2699–2703

Ostermann M, Deutsch A, Schärer U (1996) Impact melt dikes in the Sudbury multi-ring basin (Canada): Implications from U-Pb geochronology on the Foy Offset. Meteor Planet Sci 31, 494–501

Ostertag R (1983) Shock experiments on feldspar crystals. J Geophys Res 88:B364–B376

Palme H, Goebel E, Grieve RAF (1979) The distribution of volatile and siderophile elements in the impact melt of East Clearwater (Quebec) Proc Lunar Planet Sci Conf 10th:2465–2495

Pevzner LA, Masaitis VL (1996) (in Russian)

Phillips F, Zreda MG, Smith SS, Elmore D, Kubik PW, Dorn RI, Roddy DJ (1991) Age and geomorphic history of Meteor Crater Arizona from cosmogenic Cl and C in rock varnish. Geochim Cosmochim Acta 55:2695–2698

Pilkington M, Grieve RAF (1992) The geophysical signature of terrestrial impact craters. Rev Geophys 30:161–181

Plado J, Pesonen LJ, Elo S, Puura V, Suuroja K (1996) Geophysical research on the Kärdla impact structure, Hiiumaa Island, Estonia. Meteor Planet Sci 31:289–298

Poag CW (1996) Structural outer rim of Chesapeake Bay impact crater: seismic and bore hole evidence. Meteor Planet Sci 31:218–226

Pohl J, Stöffler D, Gall H, Ernstson K (1977) The Ries impact crater. In: Roddy DJ, Pepin RO, Merill RB (eds) Impact and explosion cratering. Pergamon Press, New York, pp 343–404

Pope KO, Baines KH, Ocampo AC, Ivanov BA (1994) Impact winter and the Cretaceous/Tertiary extinctions: results of a Chicxulub asteroid impact model. Earth Planet Sci Lett 128:719–725

Pope KO, Ocampo AC, Fisher AG, Morrison J, Sharp Z (1996) Carbonate condensates in the Chicxulub ejecta depositis from Belize. Lunar Planet Sci Conf XXVII:1045–1046

Putnis A, Price GD (1979) High pressure $(Mg,Fe)_2SiO_4$ phases in the Tenham chondritic meteorite. Nature 280:217–218

Rasmussen KL, Clausen HB, Kallemeyn GW (1995) No iridium anomaly after the 1908 Tunguska impact evidence from a Greenland ice core. Meteoritics 30:634–638

Reimold WU, Koeberl C (1994) About the impact origin of the Vredefort structure. Geobull Geol Soc South Africa 37:3–7

Robertson PB, Grieve RAF (1977) Shock attenuation at terrestrial impact structures. In: Roddy DJ, Pepin RO, Merill RB (eds) Impact and explosion cratering. Pergamon Press, New York, pp 687–702

Robertson PB, Mason GD (1975) Shatter cones from Haughton dome, Devon Island, Canada. Nature 255:393–394

Robin E, Bonté Ph, Froget L, Jéhanno C, Rocchia R (1992) Formation of spinels in cosmic objects during atmospheric entry: a clue to the Cretaceous-Tertiary boundary event. Earth Planet Sci Lett 108:181–190

Roddy DJ, Boyce JM, Colton GW, Dial AL Jr (1975) Meteor crater, Arizona, rim drilling with thickness, structural uplift, diameter, depth, volume, and mass-balance calculations. Proc Lunar Sci Conf 6th:2621–2644

Roest WR, Pilkington M (1994) Restoring post-impact deformation at Sudbury: a circular argument. Geophys Res Lett 21:959–962

Rost R, Dolgov YA, Vishnevskiy SA (1978) Gases in inclusions of impact glass in the Ries crater, West Germany, and finds of high-pressure carbon polymorphs. Dokl Acad Nauk USSR 241:165–168 (in Russian)

Schmitz B, Jeppsson L, Ekvall J (1994) A search for shocked quartz grains and impact ejecta in early Silurian sediments on Gotland. Sweden. Geol Mag 131:361–367

Schneider H (1972) Shock-induced mechanical deformations in biotites from crystalline rocks of the Ries crater (Southern Germany). Contrib Mineral Petrol 37:75–85

Schneider H, Vasudevan R, Hornemann U (1984) Deformation of experimentally shock-loaded quartz powders: X-ray line broadening studies. Phys Chem Min 10:142–147

Schrand Ch, Deutsch A (1996) Phase transformations in pre-heated granitic rock samples in shock recovery experiments at 85 GPa: formation of shock-generated crystals. Meteor Planet Sci 31, A124–A125

Sharp TG, Lingemann CM, Dupas C, Stöffler D (1997) Natural occurrence of $MgSiO_3$-ilmenite and evidence for $MgSiO_3$-perovskite in a shocked L chondrite. Science 277: 352–355

Simonson BE, Davies D, Wallace M, Reeves S (1996) PGEs and quartz grains in a resedimented Late Archean impact horizon in the Hamersley Group of Western Australia. Lunar Planet Sci Conf XXVII:1203–1204

Skrotzki W (1994) Defect structure and deformation mechanisms in naturally deformed augite and enstatite. Tectonophysics 229:43–68

Smit J (1994) Extinctions at the Cretaceous-Tertiary boundary. The link to the Chicxulub impact. In: Gehrels T (ed) Hazards due to comets and asteroids. University of Arizona Press, Tucson, pp 859–878

Smit J, Kyte FT (1984) Siderophile-rich magnetic spheroids from the Cretaceous-Tertiary boundary in Umbria, Italy. Nature 310:403–405

Smith JV, Dawson JB (1985) Carbonado: diamond aggregates from early impacts of crustal rocks? Geology 13:342–343

Spray JG, Thompson LM (1995) Friction melt distribution in a multi-ring impact basin. Nature 373:130–132

Stöffler D (1971) Coesite and stishovite: Identification and formation conditions in shock-metamorphosed rocks. J Geophys Res 76:5474–5488

Stöffler D (1972) Deformation and transformation of rock-forming minerals by natural and experimental shock processes: I. Behavior of minerals under shock compression. Fortschr Mineral 49:50–113

Stöffler D, Grieve RAF (1994) Classification and nomenclature of impact metamorphic rocks: a proposal to the IUGS subcommission on the systematics of metamorphic rocks. Lunar Planet Sci Conf XXV:1347–1348

Stöffler D, Langenhorst F (1994) Shock metamorphism of quartz in nature and experiment: I. Basic observation and theory. Meteoritics 29:155–181

Stöffler D, Keil K, Scott ERD (1991) Shock metamorphism of ordinary chondrites. Geochim Cosmochim Acta 55:3845–3867
Therriault AM, Reid AM, Reimold WU (1993) Original size of the Vredefort Structure, South Africa. Lunar Planet Sci Conf XXIV: 1419–1420
Thompson LM, Spray JG (1994) Pseudotachylytic rock distribution and genesis within the Sudbury impact structure. In: Dressler BO, Grieve RAF, Sharpton VL (eds) Large meteorite impacts and planetary evolution. Geol Soc Am Sec Pap 293:275–287
Tomioka N, Fujino K (1997) Natural (Mg, Fe)SiO_3-ilmenite and -perovskite in the Tenham meteorite. Science 277, 1084–1086
Trueb LF (1971) Microstructural study of diamonds synthesized under conditions of high temperature and moderate explosive shock pressure. J Appl Phys 42:503–510
Tschermak G (1872) Die Meteoriten von Shergotty and Goalpur. Sitzungsber Akad Wiss Wien Math-Naturwiss Kl 65 Teil 1:122–145
Turner FJ (1964) Analysis of kinks in micas of an Innsbruck mica schist. N Jb Miner Mh 9:51–83
Valter AA, Yeremenko GK, Kwasnitsa VN, Polkanov YA (1992) Shock-metamorphosed carbon minerals. Nauka Press, Kiev (in Russian)
von Gruenewaldt G, Harmer RE (1992) Tectonic setting of proterozoic layered intrusions with special reference to the Bushveld Complex. Proterozoic crustal evolution (ed KC Condie). Developments in Precambrian geology 10: Chapter 5. Elsevier, Amsterdam, pp 181–213
von Engelhardt W (1972) Shock-produced rock glasses from the Ries Crater. Contrib Mineral Petrol 36:265–292
von Engelhardt W, Bertsch W (1969) Shock-induced planar deformation structures in quartz from the Ries crater, Germany. Contrib Mineral Petrol 20:203–234
von Engelhardt W, Arndt J, Stöffler D, Müller WF, Jeziorkowski H, Gubser RA (1967) Diaplektische Gläser in den Breccien des Ries von Nördlingen als Anzeichen für Stoßwellenmetamorphose. Contrib Mineral Petrol 15:91–100
von Engelhardt W, Arndt J, Fecker B, Pankau HG (1995) Suevite breccia from the Ries crater, Germany: origin, cooling history and devitrification of impact glass. Meteoritics 30:279–293
White JC (1993) Shock-induced melting and silica polymorph formation, Vredefort structure, South Africa. In: Boland JA, FitzGerald JD (eds) Defects and processes in solid state: geoscience applications. Elsevier, New York, pp 69–84

1.10.7 The Cretaceous-Tertiary Boundary Impact Event

M. A. Nazarov

The Cretaceous period was terminated by a massive extinction of major groups of animals and plants including dinosaurs, the great marine reptiles, the flying reptiles, the ammonites and belemnites, many bivalve groups, and major groups of marine phyto- and zooplankton. This is one of the most dramatic mass extinction events ever recorded. It has been estimated that as many as 75% of Cretaceous species may have been eliminated. Numerous theories have been proposed to explain the nature of the biotic crisis. However, the problem with almost all these theories was that they rested on very little physical data. Physical evidence for extinction mechanisms has largely come from the 1-30-cm-thick clay layer marking the Cretaceous-Tertiary (K-T) boundary. This

layer, deposited during the K-T transition approximately 65 Ma ago, contains strong evidence for an impact of an extraterrestrial body that had struck the Earth at the end of the Cretaceous, causing the massive extinction.

The K-T boundary clay layer is enriched relative to the crustal abundance in Ir and other siderophile elements (Ni, Co, Ru Rh, Pd, Os, Pt, Au) by factors of 5–4000. The enrichment is global in extent and has been documented at more than 75 K-T boundary sites throughout the world. It means that the siderophile anomaly should have been produced by a global-scale event for a short time. The catastrophic event could not be related to an abrupt shift in ocean chemistry because the anomaly is found in both marine and nonmarine sediments. The very low $^{187}Os/^{188}Os$ ratio of the K-T clay (up to 0.135) points to either the mantle or an extraterrestrial source for the K-T siderophiles, whereas the trace element abundance pattern of the clay is compatible only with an extraterrestrial chondritic source. Thus, geochemical data indicate firmly a catastrophic accretionary event at the end of the Cretaceous. However, no extraterrestrial particles have been detected at the K-T boundary by mineralogical methods. Only siderophile-rich, magnetite spherules and Ni-rich magnesioferrite crystals found in the K-T layer are suggested to be derived from extraterrestrial matter.

Possible accretionary mechanisms include: (1) accretion of extraterrestrial dust or a crushed material of an accreting object undergone by tidal and atmospheric disruption; (2) the impact of compact extraterrestrial objects. If the K-T accretionary event is an impact, then an impact ejecta should be present in the K-T boundary layer. In fact, this material has been recognized. It has been demonstrated that the K-T clay contains quartz grains exhibiting features characteristic of shock metamorphism. The grains show multiple sets of planar features precisely oriented with respect to the crystal structure. The only known way to produce such features is by a high-velocity impact, and quartz grains exhibiting such lamellae are commonly present in terrestrial impact craters and are produced by laboratory shock experiments. At the K-T boundary shocked quartz grains have been detected worldwide. Besides individual shocked quartz grains, composite shock-deformed grains of quartz-quartz and quartz-feldspar occur globally in the K-T layer. Shocked grains are most abundant and largest in size in K-T sections of the USA and Mexico. Here, stishovite, a high-pressure phase, was also identified. Tektitelike glasses discovered in the K-T sites of Haiti and Mexico provide further strong evidence for the presence of an ejecta component in the K-T layer. The glasses have mainly dacitic to andesitic compositions. However, some of the glasses are Ca-rich and can have resulted from mixing of impact-melted basement rocks with limestones and/or anhydrites.

The diameter of the K-T object estimated from the observed noble metal concentrations in about 10–20 km. The projectile could form an impact crater of more than 200 km in diameter. However, the K-T object could be disrupted by tidal forces and, therefore, a few craters of a smaller size could be formed. The presence of the shocked quartz grains and the andesitic composition of the

tektitelike glasses shows that the K-T object, or at least its fragment, impacted the continental crust. It has been demonstrated that the 180-km-diameter buried circular structure centered at Chicxulub, on the north coast of Yucatan, Mexico, could be a continental K-T boundary impact crater. Now the structure is under detailed investigation. another possible K-T crater is the Kara impact structure located on the Kara Sea shore, near to the Ural Mountains in Russia. The structure has a diameter of 120 km, but it may be a little older than the K-T boundary. If the Chicxulub and Kara are indeed of different ages, then the cratering rate in the Cretaceous should be much higher than the normal rate.

The kinetic energy associated with the K-T object is $>10^{30}$ erg. The transfer of the energy to the environment should lead to significant physical and chemical changes inducing massive extinction of species. Possible environmental stresses caused by the impact include: short-term heating of the atmosphere, storm winds and tsunamis, global fires, shielding of the Sun by lofted fine impact ejecta and a subsequent sharp cooling of the oceans and atmospheres, a decline in photosynthesis rates, a CO_2 and/or H_2O-greenhouse, shock production of NO giving acid rains, and/or enhanced transmission of UV light due to destruction of the ozone layer. Geochemcial studies of the K-T clay do show evidence for some environmental changes. This clay is globally enriched in soot, indicating major wildfires, whereas C, O, and N isotopic compositions of the clay record significant temperature changes, decline of bioproduction, and precipitation of acid rains.

The impact scenario of the K-T transition suggests that other mass extinctions in geological history could also have been caused by impact events. In fact, the extinctions appear to have been periodic, with a 26-Ma cycle, and terrestrial impact-crater age distributions show a similar periodicity. Therefore, it has been suggested that impacts from cyclic swarms of comets in the inner Solar System were responsible for the periodic extinctions. However, geochemical studies across main bioevent horizons in the fossil record have not provided clear evidence for the hypothesis.

References

Alvarez LW, Alvarez W, Asaro F, Michel H (1980) Extraterrestrial cause for the Cretaceous-Tertiary extinction. Science 208:1095–1108

Glen W (ed) (1994) the mass extinction debates: how science works in a crisis. Stanford University Press, Stanford, 370 pp

Sharpton VL, Ward PD (eds) (1990) Global catastrophes in Earth history. Geol Soc Am Spec Pap 247:631

Silver LT, Shultz PH (eds) (1982) Geological implications of impacts of large asteroids and comets on the Earth. Geol Soc Am Spec Pap 190:528